NOVA SCHOOL OF
SCIENCE & TECHNOLOGY

DEPARTMENT OF
PHYSICS

MARIA INÊS FRANCISCO GÂNDARA

BSc in Biomedical Engineering

EFFECTS OF SPATIAL RESOLUTION ON ARRHYTHMIA DRIVERS' DETECTION AND LOCALIZATION

INTER-ELECTRODE RECOMMENDATIONS FOR CARDIAC ELECTROPHYSIOLOGICAL MAPPING DEVICES

MASTER IN BIOMEDICAL ENGINEERING

NOVA University Lisbon
March, 2022

NOVA SCHOOL OF
SCIENCE & TECHNOLOGY

DEPARTMENT OF
PHYSICS

EFFECTS OF SPATIAL RESOLUTION ON ARRHYTHMIA DRIVERS' DETECTION AND LOCALIZATION

INTER-ELECTRODE RECOMMENDATIONS FOR CARDIAC ELECTROPHYSIOLOGICAL MAPPING DEVICES

MARIA INÊS FRANCISCO GÂNDARA

BSc in Biomedical Engineering

Adviser: Kedar Aras
Postdoctoral Scientist, The George Washington University

Co-adviser: Carla Quintão
Assistant Professor, NOVA University Lisbon

Examination Committee

Chair: Ricardo Nuno Pereira Verga e Afonso Vigário
Associate Professor, NOVA University Lisbon

Rapporteur: Luís Miguel Domingues Ferreira Silva
Postdoctoral Researcher, NOVA University Lisbon

Adviser: Kedar Aras
Postdoctoral Scientist, The George Washington University

MASTER IN BIOMEDICAL ENGINEERING

NOVA University Lisbon
March, 2022

Effects of spatial resolution on arrhythmia drivers' detection and localization

---

This document was created with the (pdf/Xe/Lua)LaTeX processor and the NOVAthesis template (v6.8.2) [1].

To my family.

ACKNOWLEDGEMENTS

Throughout the work on this thesis, I had great support and I had the opportunity to meet incredible people to whom I am grateful.

First of all, I would like to express my sincere gratitude to my advisor, Dr. Kedar Aras, for supporting me and teaching me so much throughout these months. Kedar has become a role model for me in every aspect, from his dedication and sagaciousness to his contagious good humour. I would like to thank Dr. Igor Efimov, for giving the chance to work at the Efimov Lab, exposing me to fantastic projects and allowing me to meet so many impressive people. I would also like to acknowledge Eric, Zach, Sharon, Paloma, Rose, Micah, and everyone at the lab for receiving me with open arms. A special thanks to Jaclyn, for letting me assist and actively participate in her human heart experiments. Additionally, I would like to thank Dr. Carla Quintão, for reassuring me and providing feedback on my work.

Furthermore, I would like to greatly thank Dr. Caroline Roney for taking the time to explain to me her research and thought process, as well as providing advice on my work. My gratitude goes to Dr. Fu Siong Ng as well, for his responsiveness and for establishing the contact with Dr. Caroline.

I would also like to thank Mariana, Telmini, Vera and William for their beautiful friendship, that always makes me feel so close when I am far. To all my friends and colleagues that I have met throughout these years in FCT, thank you for accompanying me and making this an incredible journey.

To Afonso, thank you so much for always being there for me and for encouraging me to take chances. Your help and love were indispensable in every step of the way.

Lastly, a whole-hearted thank you to my family, for giving me all the love and support a person can wish for. To my Titi, Ilias and my cousins, Sofia and Catarina, for taking care of me and allowing me the joy of spending these months with them. And to my parents, Isabel and José, and my brother, Diogo, for always loving me, motivating me, and for providing me so many opportunities. You are my happiness.

“Whether you think you can, or you think you can’t –
you’re right.”

Henry Ford

ABSTRACT

Arrhythmia is a cardiac rhythm disorder that can be fatal. Its treatment includes ablation of the cardiac tissue and/or defibrillation. Advances are being made for both treatment options to localize the culprit region and apply therapy directly where it is needed. However, success rates have been inconsistent, with frequent arrhythmia recurrence. A likely reason is the limited current resolution of mapping devices, that averages 4 mm. Higher resolution may improve localization of arrhythmia drivers, termed rotors, and consequently improve efficacy of treatment.

This study evaluates the effects of spatial resolution on arrhythmia dynamics, rotor tracking, and rotor localization. Optical data from ex vivo human hearts was used, being clinically relevant and with ultra-high spatial resolution. To simulate different resolutions, original data was downsampled by multiple factors and upsampled back to full resolution. Rotors were tracked for each sub-resolution and compared to the rotors in the original data. Further comparisons were made according to arrhythmia type, sex, anatomical region, and mapped surface. Accuracy profiles were created for both rotor detection and localization, describing how accuracy changed with spatial resolution and spatial accuracy.

Rotor detection accuracy for currently used mapping devices was found to be 57±4%. Localization accuracy is 61±7%. Detection accuracy was above 80% only for a resolution of 1.4 mm. Moreover, the detection and localization accuracies were affected by arrhythmia type, and rotor incidence was found to be higher in the endocardium. Therefore, current clinical rotor detection and localization accuracies can be expected to fall within a confidence interval of 47-67% and 46-75%, respectively. This means that a higher spatial resolution is needed in cardiac mapping devices than what is currently available. For high accuracy, a resolution of at least 1.4 mm is required. The accuracy profiles provided in this thesis may serve as a guideline for future mapping device development.

Keywords: Optical mapping, Cardiac electrophysiology, Spatial resolution, Arrhythmia dynamics, Rotor, Phase singularity.

RESUMO

Arritmia é um distúrbio do ritmo cardíaco que pode ser fatal. O seu tratamento passa por ablação do tecido cardíaco e/ou desfibrilhação. Tem havido progressos em ambas as opções para localizar a região afetada e aplicar a terapia diretamente onde é requerida. Contudo, a taxa de sucesso tem sido inconsistente, com frequente recorrência das arritmias. Uma razão provável é a limitada resolução atual dos dispositivos de mapeamento, sendo, em média, de 4 mm. Uma maior resolução poderá melhorar a localização de catalisadores de arritmias, designados por rotores, e, consequentemente, melhorar a eficácia do tratamento.

Este estudo avalia os efeitos da resolução espacial na dinâmica de arritmias e na localização e deteção de rotores. Dados óticos de corações humanos ex vivo foram usados, tendo alta resolução espacial e sendo clinicamente relevantes. De modo a simular diferentes resoluções, os dados recolhidos foram *downsampled* por vários fatores e *upsampled* de volta para a resolução original. Os rotores foram monitorizados para cada sub-resolução e comparados com os rotores dos dados originais. Outras comparações foram feitas em consideração com tipo de arritmia, sexo, região anatómica e superfície mapeada. Perfis de exatidão foram criados para a deteção e localização de rotores, de forma a descrever as alterações na exatidão face à resolução especial e exatidão espacial.

A exatidão da deteção de rotores para os atuais dispositivos de mapeamento é de 57±4%. A exatidão da localização é de 61±7%. A precisão da deteção foi acima de 80% apenas para uma resolução de 1,4 mm. Adicionalmente, as exatidões de deteção e localização foram afetadas pelo tipo de arritmia e a incidência de rotores é maior no endocárdio. Portanto, as atuais exatidões clínicas de deteção e localização de rotores encontram-se num intervalo de confiança de 47-67% e 46-75%, respetivamente. Ou seja, é necessária uma maior resolução espacial nos dispositivos cardíacos de mapeamento do que existe atualmente. Para uma alta precisão, é necessária uma resolução de pelo menos 1.4 mm. Os perfis de exatidão disponibilizados nesta tese poderão servir como diretriz para o futuro desenvolvimento de dispositivos médicos de mapeamento cardíaco.

Palavras-chave: Mapeamento ótico, Eletrofisiologia cardíaca, Resolução espacial, Dinâmicas de arritmia, Rotor, Singularidade de fase.

CONTENTS

Appendices

List of Figures

LIST OF TABLES

GLOSSARY

ablation	Burning cardiac tissue to block pathological impulse propagation, as a mean of treatment.
arrhythmia	Cardiac rhythm disorder.
chirality	Direction of rotation of a phase singularity.
cycle length	Duration of a full cardiac cycle, that is, time between two consecutive depolarizations.
defibrillation	Application of an electrical shock to the whole heart in order to reset electrical activity. Used when the heart is in fibrillation. See fibrillation.
detection accuracy	Measurement of the proportion of true rotors detected in detriment of false and/or missed rotors. Given by the F1-score.
downsampling	Decimation of data by eliminating the data corresponding to certain pixels.
electrode	Metal plaque or needle that transfers electrical energy between the body and a device. It can be used for diagnostic, by translating physiological currents into signals, or for treatment, by applying electric current to the tissue.
endocardium	Inner layer of the heart wall.
epicardium	Outer layer of the heart wall.
F1-score	Harmonic mean of precision and recall. Provides a sense of the overall accuracy. See precision and recall.
fibrillation	Completely uncoordinated contraction of the heart muscles.
inter-electrode distance	Length between electrodes in a device. Directly related to spatial resolution, as the value of spatial resolution corresponds to the inter-electrode distance. See spatial resolution.

interpolation	Estimation and construction of intermediate data points based on known data points.
localization accuracy	Measurement of the proportion of true density peaks in rotor density maps, in detriment of false and/or missed peaks. Given by the F1-score. See F1-score.
mapping catheter	Thin tube with electrode(s) at the tip that is inserted through an artery and guided to a heart chamber. Used to map electrical activity in the heart chambers. See electrode.
myocardium	Muscular layer of the heart, between the epicardium and the endocadium.
optical mapping	Technique to map the electrical activity of the heart. The tissue is perfused with a voltage-sensitive dye and illuminated with a specific wavelength light that excites the dye. A specialized camera records the fluorescent output in its field of view. The output depends on the electrical state of the cardiac cells.
phase singularity	Center of rotation of a spiral wave. In a phase map, it is a point with no defined phase value, surrounded by tissue with phases ranging from π to π [2]. Interchangeable with rotor.
precision	Fraction of true positives by the sum of true positives and false positives. For rotor detection, it corresponds to the fraction of true rotors detected among all rotors detected in a sub-resolution. For rotor localization, it corresponds to the fraction of true density peaks detected among all density peaks detected in a sub-resolution.
recall	Fraction of true positives by the sum of true positives and false negatives. For rotor detection, it corresponds to the fraction of true rotors detected in a sub-resolution among all true rotors. For rotor localization, it corresponds to the fraction of true density peaks detected in a sub-resolution among all true density peaks.
rotor	Spiral wave in cardiac phase maps that identifies a reentrant circuit. Interchangeable with phase singularity.
rotor duration	Average lifespan of the rotors detected.
rotor incidence	Number of rotors detected per unit area in eight seconds.

spatial accuracy	Maximum permissible displacement from the original location. A higher spatial accuracy corresponds to a smaller displacement radius.
spatial resolution	For optical maps, refers to the size the pixels. For an electrode array, it refers to the distance between electrodes. In this study, the pixel resolution of the optical maps was kept the same, but the resolution of the data itself was diminished because the data was decimated, resulting in bigger spacing between pixels with true data. A higher spatial resolution corresponds to smaller pixels or a smaller inter-electrode-distance. Directly related to inter-electrode distance.
stable rotor	Rotor that lasts the minimum cycle length or longer. See rotor.
tachycardia	Abnormally fast heart rhythm.
upsampling	Increment of data points by interpolating the values between known data points and extrapolating outside known data. See interpolation.

ABBREVIATIONS

AF	atrial fibrillation
AP	action potential
API	apical
APS	all phase singularities
AT	atrial tachycardia
AV	atrioventricular
CL	cycle length
DF	dominant frequency
ECG	electrocardiogram
FIRM	focal impulse and rotor modulation
ICD	implantable cardioverter defibrillator
IED	inter-electrode distance
LA	left atrium
LV	left ventricle
MID	mid-ventricular
MVT	monomorphic ventricular tachycardia
PS	phase singularity
RA	right atrium
RV	right ventricle
RVOT	right ventricular outflow tract
SA	sinoatrial

SEM	standard error of the mean
SR	stable rotor
VF	ventricular fibrillation
VT	ventricular tachycardia

Chapter 1

Introduction

Cardiovascular disease is the leading natural cause of death in developed countries [3]. Sudden cardiac death accounts for 50% of the mortality due to cardiac issues, being responsible for an estimated 4-5 million deaths per year globally [4], [5]. The majority of sudden cardiac death cases are caused by rhythm disorders, also known as arrhythmias. The arrhythmias that lead to death usually originate in the ventricles, such as ventricular tachycardia (VT) and ventricular fibrillation (VF). When in the atria, this disorder is not much more benevolent, being a major risk factor for ischemic stroke [6].

Current treatment options vary depending on the etiology and location of the arrhythmia. For atrial tachycardia and fibrillation, the preferred therapy is radiofrequency ablation, which involves damaging the heart tissue to block pathological impulse conduction. The alternative to ablation is anti-arrhythmic drugs, which have been shown to have limited efficacy and can be associated with adverse side effects [7], [8]. Focal ablation targets electrical conduction irregularities called rotors, that are present when the propagation wavefront circulates around itself in a spiral instead of following a linear path. These rotors are thought to maintain and drive arrhythmic episodes. Rotor ablation has presented divergent success rates, and a possible reason agreed upon is unequal spatial resolution used by different studies. Indeed, the resolution and electrode density of current cardiac mapping devices may be insufficient, and precise and accurate detection of ablation targets is necessary for the successful termination of the arrhythmic episode. Consense on the appropriate resolution to adequately map rotors is still to be reached.

In the case of VT or VF, the treatment of choice is defibrillation. Defibrillation consists in discharging an electrical shock to the chest that effectively resets the electrical activity of the heart, successfully terminating the majority of VFs [9]. The need for such violent measures is due to the quick progression of these episodes, so much so that a 10-minute delay in delivery of defibrillation results in a nearly zero survival rate [10]. To avoid such circumstances, the use of an implantable cardioverter defibrillator (ICD) is indicated for patients who have survived a cardiac arrest caused by VF or VT without revertible cause and patients who are likely to suffer from severe VT/VF in the future [11]. The ICD can detect VT and VF and applies a defibrillation shock when detected. However, electric therapy has its own hindrances. Due to the technological limitations of the current ICD devices, such as high defibrillation threshold and low VT/VF sensing resolution, the shocks delivered are extremely painful [12]. There are two ways to decrease the amount of energy of the shocks and, consequently, the pain induced: (1) narrow the scope of the shock to the area that needs it, and (2) apply a sequence of lower energy shocks instead of a single high energy one. While there has been progress with the second option [13], it remains very hard to lower the shock's energy without jeopardizing the defibrillation success if the arrhythmia's site is unknown. Locating a ventricular arrhythmia and determining the ideal site for therapy is very challenging and currently there is no method available for it. This leads to an unmet need for high-definition VT/VF sensing to minimize inappropriate shocks and improve therapy. In order to achieve that, it is important to know the spatial resolution required to correctly identify and localize arrhythmia drivers.

For the treatment of both atrial and ventricular tachycardia, a need is present for the establishment of the maximum inter-electrode spacing for arrhythmic mapping devices. Studies have been done to try and assess the minimum spatial resolution necessary to successfully map rotors, but the majority of them has supported themselves in simulated data or animal models, none of which is ideal to properly determine the true resolution needs of human cardiac electrophysiology.

This thesis proposes the use of high spatiotemporal resolution data obtained by optically mapping the electrical activity of ex vivo donor human hearts to deduce the spatial resolution requirements for accurate detection and localization of rotors. The usage of optically mapped human data sets this work apart from previous studies.

1.1 Thesis goals

This thesis aims to analyze and quantify the loss of information due to spatial resolution when mapping cardiac arrhythmias. The hypothesis is that the minimum spatial resolution for electrode mapping devices could be inferred through the downsampling of optical data, which has a spatiotemporal resolution much higher than what can currently be obtained with electrodes. In order to achieve the overarching aim, the following goals were identified and pursued:

- Analyze the impact of spatial resolution on perceived arrhythmia dynamics;
- Analyze the impact of spatial resolution on rotor detection;
- Analyze the impact of spatial resolution on rotor localization;

- Define the minimum inter-electrode distance for robust rotor detection and localization.

1.2 Thesis overview

The thesis is structured as follows. Chapter 2 goes over the theoretical concepts relevant for the understanding of the thesis and the studies that have been done on the spatial resolution requirements for mapping the heart. In Chapter 3, the study methodology is presented, encompassing all the steps necessary to obtain and condition the optical data, the process to assess correlation between sub-resolution results and the original data, the metrics that were retrieved, and how they were analyzed. In Chapter 4, the results obtained are presented and interpreted. Lastly, in Chapter 5 the main conclusions from the results are drawn, the study's limitations are identified, and solutions to the limitations and possible future directions are presented.

CHAPTER 2

LITERATURE REVIEW

This chapter summarizes important concepts for the understanding of the thesis and reviews the research done on the subject. First, the anatomy and the normal electrophysiology of the heart are explained in Section 2.1. With that knowledge, it is possible to go deeper and explore a common cardiac pathology, the arrhythmia, along with its causes and possible treatments, in Section 2.2. To study this pathology, and for some therapies, it is necessary to map the electrical activity of the heart in order to understand its mechanisms. The current mapping methods and emerging technologies are explored in Section 2.3. Finally, an adequate spatial resolution of the mapping devices is crucial to ensure accurate cardiac mapping. Since the objective of this thesis is to assess the necessary resolution for mapping arrhythmias, the studies done in that respect are reviewed in Section 2.4.

2.1 Cardiac anatomy and electrophysiology

The heart is a muscular organ responsible for pumping blood through the body. As shown in Figure 2.1, it is composed of four chambers: right atrium (RA), left atrium (LA), right ventricle (RV) and left ventricle (LV). The right and left sides of the heart function as two separate pumps. On the right side, the blood enters through the superior vena cava into the RA, flows to the RV and is ejected through the right ventricular outflow tract (RVOT) into the pulmonary artery, towards the lungs. On the left side, the blood enters the LA through the pulmonary veins, and the LV propels it through the whole body. The heart itself is irrigated by the coronary arteries, that branch from the ascending aorta [14]. The heart walls are mainly composed of muscular tissue, called myocardium, that stands in between the inner and outer layers of the wall, the endocardium and epicardium, respectively.

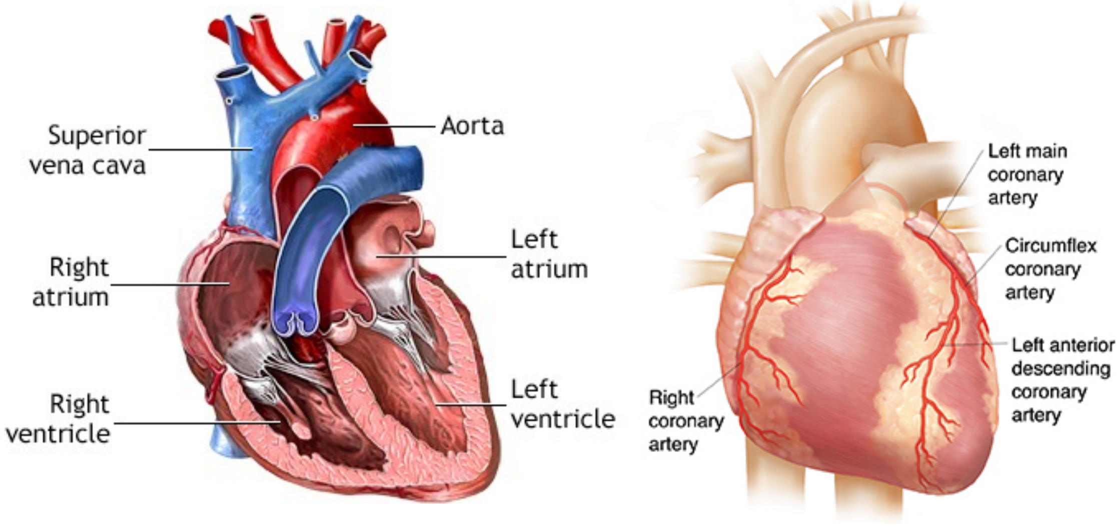

Figure 2.1: Heart anatomy. **Left.** Frontal cut of the heart, showing the heart chambers, veins, and arteries responsible for the blood circulation through the heart. Adapted from [15]. **Right.** Frontal view of the heart, showing the coronary arteries. Adapted from [16].

The ability of the heart to work as a pump is due to the contractibility of its muscles. Cardiac muscle fibers are interconnected so that when one cell is excited it quickly propagates through the rest of the cardiac cells. The atria and the ventricles are separated by fibrous tissue, enabling them to contract at different times [17].

The coordinated contraction of the cardiac muscle cells, termed myocytes, is regulated by an impulse-conducting system, illustrated in Figure 2.2, which is composed of specialized cells that can generate and transmit action potentials without input from the nervous system. The electrical impulse is normally initiated by the sinoatrial (SA) node and propagated through the atria. The impulse arrives at the atrioventricular (AV) node and follows through a passage to the ventricles, denominated by bundle of His. The pathway bifurcates, originating the right bundle branch and the left bundle branch. These branches divide further into the Purkinje fibers, which spread the impulse through the ventricular walls [18]. This results in synchronized contraction of the ventricular myocytes [17].

The cardiac cycle is maintained through the conduction of electric impulses, termed cardiac action potentials, through the myocardium. The action potential (AP) is created by a sequence of ions fluxes through the myocytes' cell membrane. The membrane is a phospholipid bilayer highly impermeable to ions, so the ionic movements are controlled by specialized proteins (ion channels, passive cotransporters, and active transporters). The voltage of the membrane defines the type and the number of channels open, so the gating of the channels is said to be voltage-sensitive [18], [20].

The AP of a typical myocyte is represented in Figure 2.3. In phase 4 the cell is at rest. In this state, the potassium (K^+) concentration is much higher inside the myocyte and the sodium (Na^+) and calcium (Ca^{++}) concentrations are much higher outside. At rest,

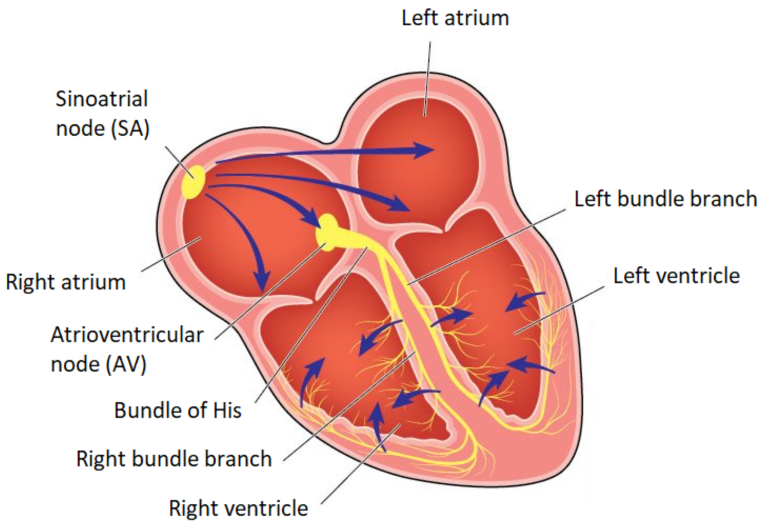

Figure 2.2: Impulse-conducting system and its components. Adapted from [19].

the cell's membrane is impermeable to ions other than potassium and its transmembrane potential is approximately -90 millivolts (mV) (negative voltage means the inside of the cell is more negative than the outside). In the case of pacemaker cells, such as the SA node, the maximum negative voltage is approximately -60 mV [20]. The AP occurs when the cell's membrane voltage is altered.

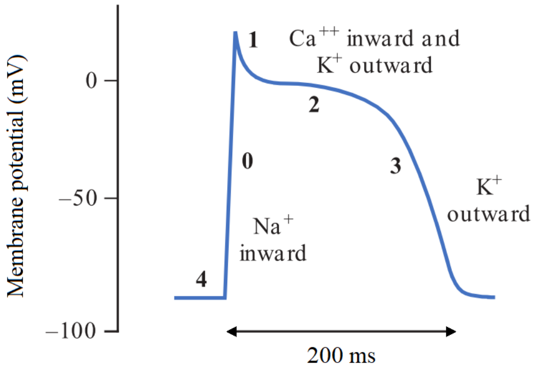

Figure 2.3: Representation of the action potential of a typical myocyte. The resting state of the membrane's potential is at -90 mV (phase 4). Any stimulus that raises the membrane potential above a threshold of -70 mV induces the opening of sodium channels, leading to a quick sodium influx and consequent depolarization (phase 0). A transient outward potassium current returns the membrane potential to approximately 0 mV, causing partial repolarization (phase 1). A prolonged balance between outward K^+ current and inward Ca^{++} current results in a nearly zero net current, thus creating a plateau (phase 2). Repolarization begins when the calcium channels start to close (phase 3). The continued exit of K^+ ions returns the transmembrane voltage to -90 mV. Then, through active transport, the resting concentrations are reestablished. Adapted from [20].

Pacemaker cells have automaticity, thus do not need external stimuli to depolarize. Figure 2.4 illustrates the AP of a pacemaker cell, in which case phase 4 is a slope as a result of an ionic influx, called the pacemaker current (I_f), that leads to an autonomous depolarization of the cell [20].

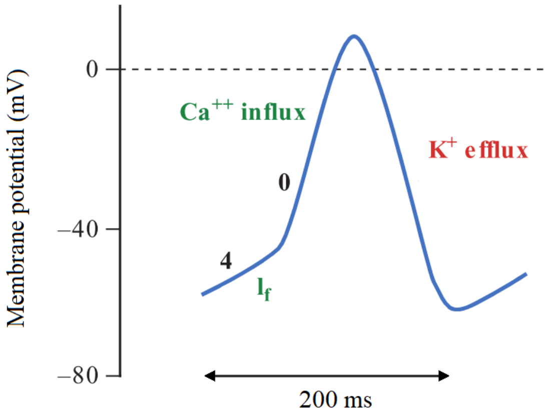

Figure 2.4: Representation of the action potential of a pacemaker cell. During phase 4, a steady influx of positively charged ions, called pacemaker current (I_f), decreases the membrane potential until it reaches the threshold voltage, which triggers a quicker and complete depolarization (phase 0). Adapted from [20].

Specialized cells from the impulse conducting system also have automaticity and, therefore, have I_f. However, since their firing rate is slower than the SA node's intrinsic rhythm, the SA node triggers depolarization through the rest of the automatic cells before they have time to spontaneously depolarize. Nevertheless, most elements of the system have the potential to act as pacemakers if the SA node is not working properly.

An important concept to retain is the refractory period. Due to the necessity of the ventricles to have enough time to relax and refill between contractions, there is a prolonged period after an electrical stimulation during which the cardiac cell is unresponsive to restimulation.

2.2 Cardiac arrhythmias

An arrhythmia is defined as an irregular heartbeat. There are two types of arrhythmia: bradycardias when the heart rhythm is abnormally slow, and tachycardias when it is abnormally fast. A tachyarrhythmia, the type that this thesis is focused on, is considered to be present if the heart rate is greater than 100 beats per minute for three beats or more [21].

2.2.1 Causes and mechanisms

While there are more arrhythmic mechanisms, the most prevalent in tachycardia are reentry, abnormal automaticity, and triggered activity.

Reentry

The most common and most studied cause of tachycardia is reentry. As illustrated in Figure 2.5, it occurs when an electric impulse circulates around a reentry path, repeatedly depolarizing a certain area of cardiac tissue. For reentry to happen two conditions are necessary: the presence of a unidirectional conduction block, that is, an area of cardiac tissue that is refractory from a previous stimulation when a new electrical impulse encounters it; and slow retrograde conduction, that is, abnormally slow impulse conduction through the tissue that previously had a unidirectional block [22].

Reentry can be anatomical or functional. In an anatomical reentry, the reentrant circuit occurs in well-defined anatomical structures and the propagating wave follows a fixed path around an obstacle, with an excitable gap separating the front of the wave and the refractory tail, as shown in Figure 2.6A [23]. However, reentry does not require an anatomic obstacle, as it can be a functional obstacle instead. Functional reentry can be described by two methods, the leading circle or rotors. Figure 2.6B is a schematic representation of the leading circle hypothesis, in which there is no fully excitable gap between the wavefront and its tail, and the tissue at the center of the leading circle is refractory due to centripetal excitation waveforms [24]. Another form of functional reentry is rotors, represented in Figure 2.6C, where the tissue at the center is not refractory and the wavefront and tail meet at the core of the rotation, termed phase singularity (PS). A rotor can be stationary, with a stable PS, or it can be meandering, in which case its trajectory may take complex shapes [24], [25]. The generation of a spiral wave is represented in Figure 2.6E, with the PS marked by an asterisk.

Abnormal Automaticity

The injury of cardiac tissue may cause normal cardiac muscle cells to gain automaticity, leading to ectopic heart beats. If the impulse formation rate of these cells surpasses that of the SA node, they will transiently function as a pacemaker and originate a tachycardia [22].

Triggered Activity

Triggered activity refers to afterdepolarization, that is, the depolarization of the cell membrane triggered by a preceding action potential. If the afterdepolarization reaches a threshold voltage, an abnormal action potential is induced. This AP may be self-perpetuating, causing a series of depolarization and, consequently, a tachycardia [22].

2.2.2 Arrhythmia classification

Arrhythmias appear in different regions of the heart and have different levels of complexity, and are categorized accordingly. Tachycardias can be designated as supraventricular, if its origin is in the atria or the AV node, or as ventricular, if the arrhythmia is related

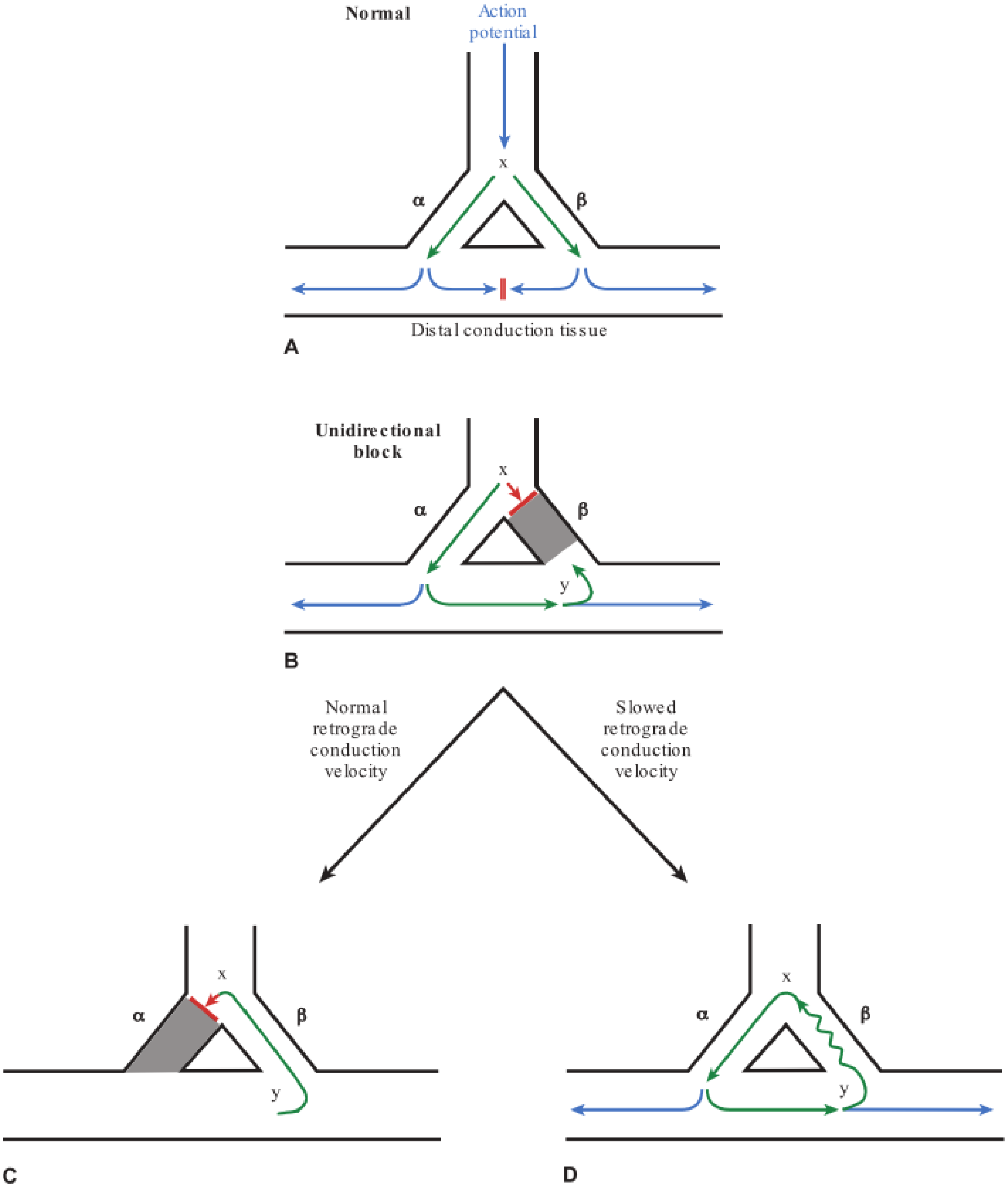

Figure 2.5: Mechanism of impulse reentry. **A.** Normal forward propagation of an electrical impulse, bifurcating in point x. **B.** Unidirectional block. The impulse encounters tissue that is still refractory from a previous stimulation. In this case, the impulse can only propagate through the α branch and, since it is not stopped by the presence of another impulse, it continues to propagate through the available paths. If the branch is no longer refractory when the impulse reaches its distal end, the AP will enter β and conduct retrogradely. **C.** If the impulse circulates with a normal velocity, it reaches the superior portion of α when it is in its refractory period and the reentry is stopped. **D.** If the retrograde conduction is abnormally slow and reaches α when it is ready to depolarize, it creates a conduction loop. Adapted from [22].

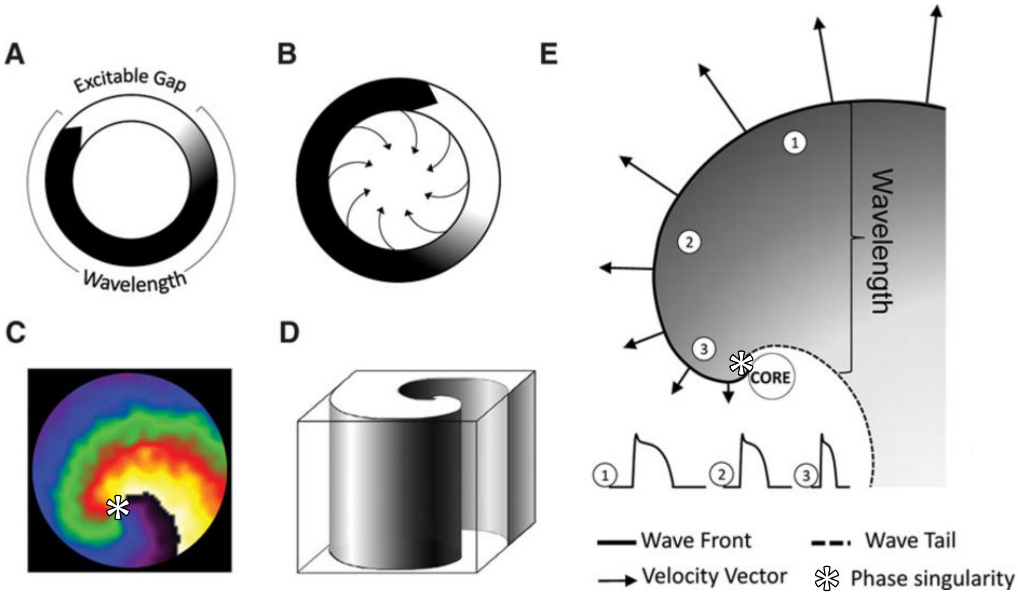

Figure 2.6: Rotors and spiral waves' dynamics. **A.** Representation of an anatomical reentry circuit. The impulse propagates around the unexcitable region and the front of the impulse wave meets the excitable gap at its tail. **B.** Leading circle, an impulse propagation wave without an excitable gap and a refractory center due to centripetal excitation waveforms. **C.** Rotor, an impulse propagating spiral wave without any separation between the wavefront and its tail. The colors in the figure represent the state of excitation of the myocytes, ranging from rest to depolarization. At the phase singularity, marked by an asterisk, the excitation's state is not defined. **D.** 3D representation of a spiral wave, designated "scroll wave". **E.** Propagation of a spiral wave around a phase singularity, marked by an asterisk. Adapted from [24].

to the His-Purkinje system or the ventricles. They can be further divided by their mechanism and electrocardiogram (ECG) presentation, an ECG being a measurement of the electric activity of the heart through the body's surface. Figure 2.7 provides a reference for what a normal ECG should look like, and illustrates the components of a heartbeat measured by an ECG: P wave, QRS complex, and T wave. The P wave is caused by the depolarization of the atria; the QRS complex, formed by three distinct waves, results from the depolarization of the ventricles; and, finally, the T wave is induced by the ventricles while they recover from depolarization, being associated with the repolarization of the cell. The RR interval corresponds to a full cardiac cycle [26].

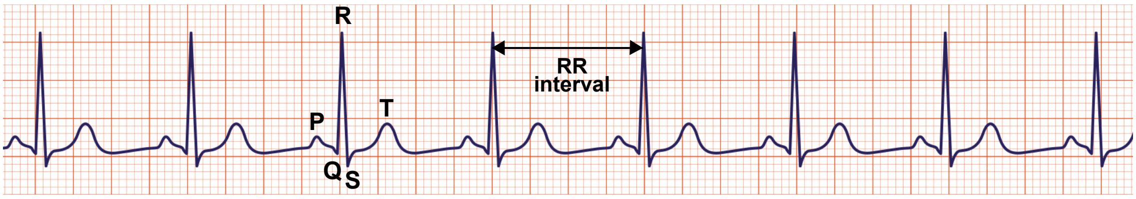

Figure 2.7: Representation of a normal electrocardiogram (sinus rhythm). Adapted from [27].

Supraventricular tachycardias

Supraventricular tachycardias are divided into atrial tachycardias (AT), sinus tachycardia, and paroxysmal supraventricular tachycardia.

Common ATs are atrial premature beats, atrial flutter, and atrial fibrillation (AF). An atrial premature beat is caused by an ectopic focus in the atria. Atrial flutter is characterized by rapid, regular atrial activity, as shown in Figure 2.8, while AF is a chaotic rhythm that makes the P wave in an ECG indiscernible, illustrated in Figure 2.9. Sinus tachycardia refers to increased automaticity of the SA node. Its ECG morphology is normal, but the heart rate is high, as in Figure 2.10. Paroxysmal supraventricular tachycardia, shown in Figure 2.11, is usually generated by a reentrant circuit, connecting the atria with the ventricles. The reentry pathway can be either in the AV node region or through an accessory pathway. If the AV node is the cause, it is denominated an atrioventricular nodal reentrant tachycardia. If the impulse reenters the atria through a pathway that does not belong to the normal conducting system, it is called an atrioventricular reciprocating tachycardia [21], [28]–[31].

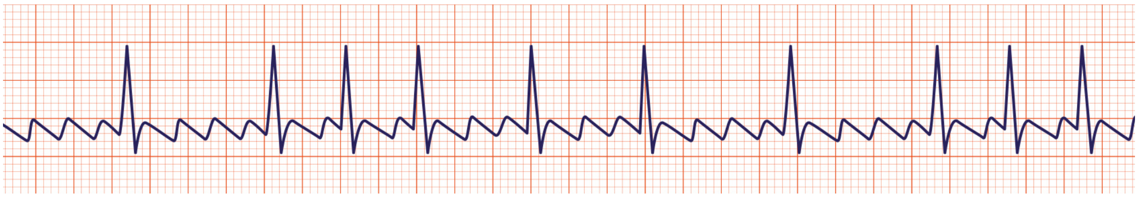

Figure 2.8: Representative electrocardiogram signal of atrial flutter, characterized by a "sawtooth"pattern [30]. Adapted from [27].

Figure 2.9: Representative electrocardiogram signal of atrial fibrillation. Characterized by irregular R-R intervals and irregular atrial waves [30]. Adapted from [27].

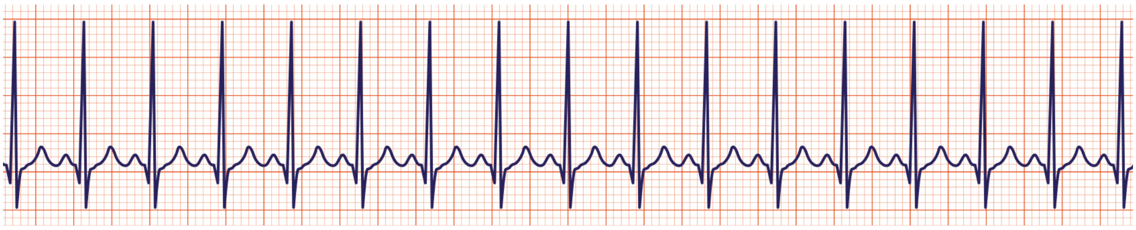

Figure 2.10: Representative electrocardiogram signal of sinus tachycardia. Characterized by regular increase in heart rate [31]. Adapted from [27].

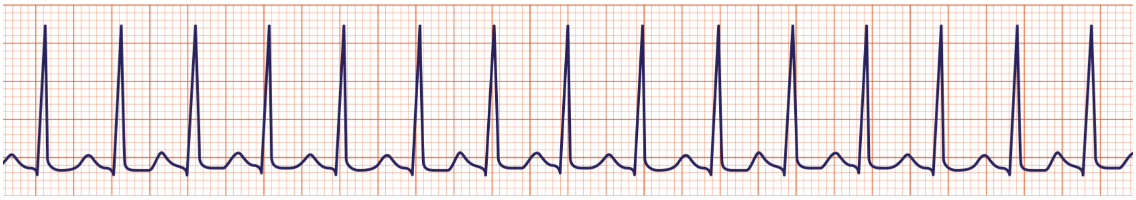

Figure 2.11: Representative electrocardiogram signal of supraventricular tachycardia. Characterized by increased heart rate and hidden P wave [30]. Adapted from [27].

Ventricular tachycardia

Ventricular tachycardias can present as ventricular premature beats, ventricular tachycardia (VT) or ventricular fibrillation (VF).

A ventricular premature beat, just like its atrial counterpart, appears when an ectopic focus triggers an action potential. A ventricular premature beat in itself is not dangerous, however, it may indicate an underlying disorder and be worrisome [21].

VT is considered to be present if there is a series of three or more consecutive ventricular premature beats. There are two types of VT: sustained VT, if it persists for more than 30 seconds, which causes extreme symptoms or requires immediate therapy, or non-sustained VT, if it is self-terminating. Another dichotomy is monomorphic VT and polymorphic VT. Monomorphic VT (MVT), as seen in Figure 2.12, is a sustained VT with widened QRS complexes that are seemingly constant in shape and rate. It usually derives from an anatomic reentrant circuit. On the other hand, a polymorphic VT's signal has no stable shape or rhythm. Typically, the mechanisms behind it are multiple ectopic foci or a complex rotor-based reentry. Sustained polymorphic VT normally results in VF.

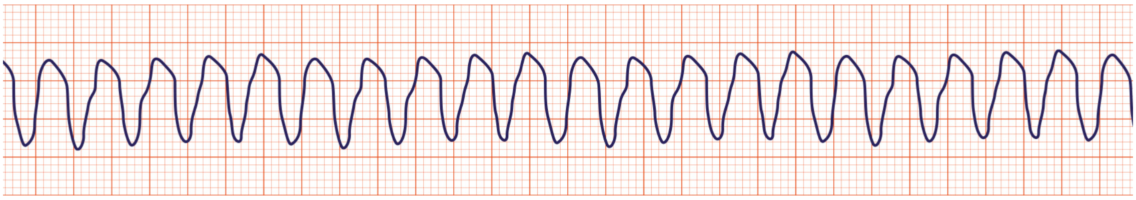

Figure 2.12: Representative electrocardiogram signal of a monomorphic ventricular tachycardia. Characterized by an identifiable and morphologically stable QRS complex [30]. Adapted from [27].

VF is the result of rapid and erratic electrical impulses that disables coordinated contractions, terminating cardiac output and leading to death if not quickly treated. Its ECG signal, in Figure 2.13, is easily identifiable by being a chaotic line without any discrete QRS complex [21].

2.2.3 Treatment

There are three different approaches to treat arrhythmia: pharmacologic therapy, catheter ablation, and electrical therapy.

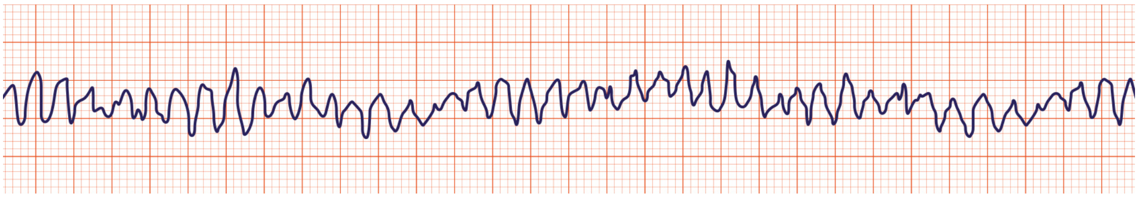

Figure 2.13: Representative electrocardiogram signal of ventricular fibrillation. Characterized by a chaotic line without discernible QRS complexes [21]. Adapted from [27].

Antiarrhythmic Drugs

Antiarrhythmic drugs work by changing ion channels' activity. While being a common treatment for tachycardia, these drugs can be very dangerous as they easily become proarrhythmic instead. By altering the AP morphology, new arrhythmias can be triggered [8]. Therefore, pharmacologic therapy is not ideal and antiarrhythmic drug development has begun to focus more on reducing arrhythmia symptoms rather than treating it [32].

Catheter Ablation

In the case of spatially stable arrhythmia drivers or known anatomical sources, ablative therapy is usually the recommended treatment. Cardiac ablation is performed using a transvenous catheter that applies radiofrequency current directly on the myocardium, heating and damaging the tissue and consequently removing its conductive properties [22], [33]. Therefore, ablation is useful to isolate arrhythmogenic regions and block reentrant pathways. The pathological source is identified and located with electrophysiologic mapping techniques, explored in Section 2.3, that vary according to the arrhythmia's complexity.

The main employment of this method is in the treatment of atrial tachycardia and fibrillation, specifically for pulmonary vein isolation. The pulmonary vein muscular sleeves (extensions of myocardium over the pulmonary veins) are known to be where most focal triggers appear [34] and, therefore, that region is electrically separated from the rest of the myocardium through a point-by-point linear ablation encircling the vein [33], [35]. If the ectopic foci or micro-reentry circuits are located in other regions, focal ablation is preferred [33]. This localized treatment is also applied in cases of recurrent VF or VT caused by focal triggers, playing a long-term protective role [36]–[39].

A new and still experimental technique for focal ablation of rotational arrhythmia drivers is called focal impulse and rotor modulation (FIRM) mapping [40], [41]. It utilizes the phase information of intracardiac electrograms to track the progression of the mapped region through the action potential and consequently localize phase singularities [42]. Even though the success rates for ablation guided by FIRM mapping are contradictory at this time, the technique shows great promise for tailored therapy [43]–[46].

Despite its advantages, if tissue ablation is not performed in the correct area the treatment will not be successful, and high volumes of ablated tissue may generate further arrhythmic substrate by creating slow conduction regions [47]. Therefore, the pursuit of high resolution and high precision mapping techniques is necessary.

Electric Cadioversion and Defibrillation
When an arrhythmia is life-threatening and fast response is needed, such as in the case of VF, electric treatment is the only option. When a high-energy electrical current is applied to the heart, it depolarizes the majority of the myocardium, resetting its electrical configuration. This interrupts reentrant circuits and enables the SA node to regain the pacemaker function. However, if the cause of arrhythmia is abnormal automaticity, the condition may persist. While both electrical cardioversion and defibrillation require shocking the heart, they differ on the targeted type of tachycardia. Cardioversion is performed to terminate supraventricular tachycardias or monomorphic VT. In this case, the device synchronizes with the ECG signal in order to discharge when a QRS complex (corresponding to ventricular depolarization) occurs, preventing discharge during a T wave which may induce reentry. During VF, however, there are no distinct QRS complexes, so the shock is not synchronized. An unsynchronized electrical discharge is termed defibrillation [22].

Cardioversion and defibrillation can the applied externally, using two-electrode paddles or adhesive electrodes, or internally, through an implantable cardioverter defibrillator (ICD). Although the energy required for internal electrical therapy is significantly less than for external therapy, the procedure is still painful for the patient [22]. Therefore, research is being conducted to try to minimize the energy necessary to terminate arrhythmia, by either applying multiple lower-energy pulses or restricting the shock delivered to the area of interest [13], [48].

2.3 Electrophysiological mapping of the heart

Cardiac mapping aims at characterizing and visualizing the propagation of the electric impulses across the myocardium. In the case of arrhythmia, electrophysiological mapping becomes particularly useful to detect potential arrhythmia drivers and to study the mechanisms that generate and maintain these unstable rhythms.

2.3.1 Catheter-based

The clinically employed method for cardiac mapping without surgery is through catheters. A mapping catheter is a thin, flexible tube that is inserted through the femoral or radial artery and steered to the heart chambers [49]. Catheters have electrodes that enable the discrete measurement of the electrical activity at each contact point. Thus, multiple electrodes can acquire physiological signals from different sites in the endocardium and paint a picture of the overall electrical activity and propagation dynamics. In a clinical setting, mapping is mostly used to guide ablation therapy.

There are multiple mapping techniques using catheters, with varying levels of complexity. The conventional method is the simplest and is adequate for the ablation and isolation of known arrhythmogenic landmarks [50]. It employs the roving probe technique, in which a probe with one or more electrodes is moved across the heart chamber to record the electrical activity at different sites [51], [52]. Multiple probes can be used, either stationary or moving, recording one probe at a time [53], [54]. Due to the time required to move the probe in order to create a single map, it cannot map impulse propagation for each heartbeat and will only detect long-lasting and stable arrhythmias [55].

Advancements on the multiplexer technology, which allows a mapping device to quickly send multiple input signals through a single output, opened the door to new catheter configurations [55]. Figure 2.14 provides visual examples of some of the current catheter designs, that go from simple linear catheters to basket and star-shaped configurations. Of all of these, the most ambitious design in terms of coverage is the basket. These catheters have 5-8 flexible splines with multiple electrodes that are collapsible to navigate through the vessels and that expand inside the heart chamber to achieve the highest amount of contact points with the endocardium. By simultaneously recording from the entire chamber, this design allows mapping of impulse propagation beat to beat, making it possible to track more unstable arrhythmias, such as atrial and ventricular fibrillation [56], [57].

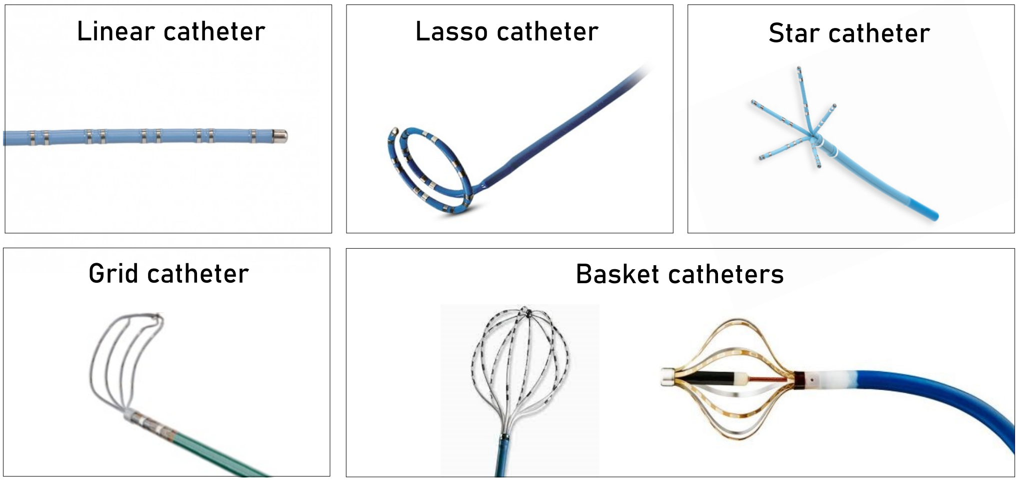

Figure 2.14: Examples of current catheter styles: linear, lasso, star, grid and basket catheters. Adapted from [58]–[61].

Basket catheters are considered to have high resolution, due to their small inter-electrode distances (IEDs) and their high electrode density compared to other catheter designs. Along the splines, IED can be as narrow as 2 mm in the most recent models, as displayed in Table 2.1, which presents some catheters manufactured by different medical device companies and their spatial resolution. However, between splines, the IED reaches much higher values. In Table 2.1, the basket's diameter corresponds to its equator's diameter when fully deployed. Knowing the diameter, it is possible to infer the maximum IED between splines by calculating the circumference of the equator and dividing it by the number of splines. For the Constellation catheter (Boston Scientific, Marlborough,

Table 2.1: Comparative table of currently used clinical mapping catheters. The mean of the inter-electrode distances is approximately 4 mm.

Catheter	**Style**	**NE**	**D (mm)**	**IED (mm)**
Constellation™[1]	Basket	64	31 to 75	2 to 7
IntellaMap Orion™[1]	Basket	64	22	2.5
Advisor™ HD Grid[2]	Grid	16	N/A	3
Inquiry™ Afocus II™[2]	Double Loop	20	N/A	4
Lasso® Nav[3]	Single Loop	10 or 20	N/A	8 or 2-6-2
Pentaray® Nav[3]	Star	20	N/A	4-4-4 or 2-6-2
Decanav®[3]	Linear	10	N/A	2-8-2

NE, number of electrodes; D, diameter; IED, inter-electrode distance.

[1] Boston Scientific, Marlborough, Massachusetts, USA [62] [63].

[2] Abbott, Plymouth, Minnesota, USA [59].

[3] Biosense-Webster, Irvine, California, USA [64].

Massachusetts, USA), with a diameter of 31 mm, the approximate IED at the equator is 12.2 mm. For bigger models, this value will go up to 29.5 mm. The IntellaMap Orion (Boston Scientific, Marlborough, Massachusetts, USA) is a smaller-sized basket, and the maximum IED at its equator is approximately 8.6 mm.

Besides the structural spacing between electrodes, mapping catheters' empirical spatial resolution drops even lower due to poor tissue contact [41]. The heart chambers are a dynamic environment, and the catheters' relative rigidity may fail to adapt and conform to the beating heart wall. This leads to spacing between some electrodes and the endocardium, which has been shown to negatively impact signal quality [41], [65]. Furthermore, significant spline bunching has been observed when deploying basket catheters [41], [66], heavily diminishing coverage of the atria. The emergence of flexible and stretchable electronics has led to the development of soft, implantable devices that have shown promise in addressing these issues.

2.3.2 Conformal bioelectronics

A new class of stretchable electronics is changing the paradigm of wearable and implantable devices, including for cardiac monitoring and therapy [67]. Soft bioelectronics have the potential to conform to the tissue of interest, reducing motion artifacts and maximizing coverage without affecting the natural motion of the tissue. In addition, they require no manual operation after being implanted [68]. The devices being developed have consistently achieved higher electrode densities and higher spatial resolutions than those possible for mapping catheters, with IEDs that range from 3.5 mm [69] to sub-100 µm [70], and usually map the epicardium instead of the endocardium.

The designs for cardiac electrophysiological mapping vary from two-dimensional sheets to meshes. In 2010, Viventi et al. designed a conformal electrode array with 800 µm IED that was successful in adhering to the epicardium even when it was beating rapidly [68]. It showed the promise of this technology for this finality but many improvements had to be made. One of them was the small area covered (14.4 mm by 12.8 mm), which was tackled by meshes. Cardiac meshes typically take advantage of fractal designs to enhance their elasticity [71], [72] and cover the majority of the heart [69], [72]. Stretchable bioelectronics are also being integrated with catheters, mapping the endocardium [48], [73].

Besides electrophysiological mapping, soft bioelectronics are making strides in therapy, such as pacing [74], defibrillation [71] and ablation [48], [73], [75]. Conformal bioelectronics are still far from clinical implementation, but promise a future with higher-resolution cardiac mapping and localized therapy. Subsequently, it becomes ever more relevant to define the spatial resolution needed for accurate rotor identification and localization.

2.3.3 Optical mapping

Cardiac optical mapping is used to study electrical activation, repolarization, and calcium handling in myocardial preparations with a spatial resolution and sample density much greater than possible for electrode techniques. In optical mapping experiments, the cardiac tissue is prepared and perfused with a potentiometric dye, which has a fluorescent output responsive to the transmembrane voltage of the cell. A light source with a specific wavelength excites the dye in the tissue, which in turn emits fluorescence with an intensity that is dependent on the transmembrane potential. Motion artifacts render optical signals useless, so electromechanical uncouplers are used, which inhibit the mechanical action of the heart but maintain its electrical excitation [76].

Figure 2.15 illustrates a typical optical mapping setup, in which the detector is a high-speed camera that captures the fluorescent intensity in the form of a matrix at each time point [77], [78]. This mapping method can only be used in experimental settings since the tissue needs to be dyed and electromechanical uncouplers are used.

2.4 Spatial resolution requirements for mapping arrhythmias

Spatial resolution requirements have been thoroughly studied for AF, especially with the objective of tissue ablation in mind. Since a single ablation lesion usually covers a region with 5 to 8 mm in diameter, the goal of these studies was for the rotors to be detected within that area [79], [80].

The majority of the studies used simulations of cardiac electrical activity to test the effect of spatial resolution on arrhythmia drivers' detection. Martinez-Mateu et al. used a virtual model of the atria to determine the accuracy of a basket catheter to detect rotors for guiding cardiac ablation [65]. They simulated three baskets with different IEDs. One had a realistic configuration of 64 electrodes distributed through 8 splines, with a diameter of 31 mm and an IED of 4.8 mm along its splines. The other two baskets had different

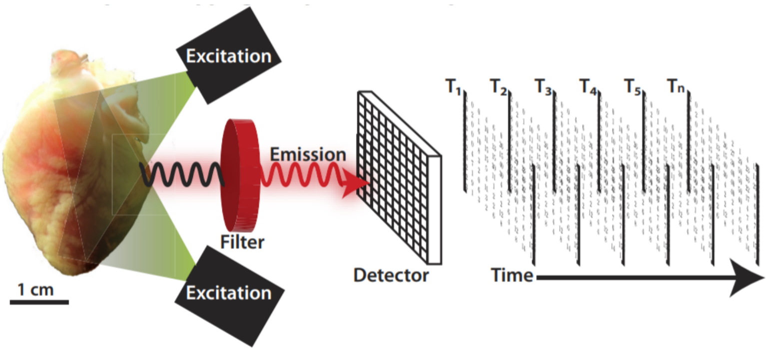

Figure 2.15: Cardiac optical mapping setup and data acquisition. The heart preparation is homogeneously illuminated by photons with an appropriate excitation wavelength. The photons excite the dye, which sequentially returns to its ground state, emitting fluorescent photons. The filter separates the illumination and emission photons, so the system only measures the relevant signal. The filtered fluorescent photos are captured by a high-speed camera, working as a detector that acquires data in the form of a series of matrices of fluorescent intensity [77], [78]. Adapted from [77].

electrode densities, one having four splines with six electrodes in each, and the other 16 splines with 16 electrodes per spline. Electrograms were computed at the coordinates of the baskets' electrodes, linearly interpolated on 57,600 points, and converted to phase in order to map rotors. They concluded that decreasing the electrode density reduced correct rotor detection, while increasing electrode density significantly reduced false rotor detection due to interpolation. In addition, for an 8x8 basket, the probability of ablating a true rotor was lower than the probability of ablating a false rotor. Ablation accuracy was expected to improve substantially for 16x16 baskets, with an IED of 2.4 mm along the splines and a maximum IED of 5.85 mm between splines.

Alessandrini et al. also used simulation in their study [81]. They created two virtual grid catheters, with 9x9 and 5x5 electrodes that translated to IEDs of 3 mm and 6 mm, respectively. High-resolution simulated electrical data of the atria served as the ground truth and the grids' electrodes' coordinates were used as sampling points. Rotors were tracked for the ground truth data and for both grid conformations, and the positions of the rotors' tip at each time point were used to create trajectory density maps. These maps provide important insight on where the rotors linger, and the position of the trajectory density maps' peak was used as the target for simulated ablation therapy. Therefore, it made sense for the distance between density maps' peak sites to be the term of comparison between the ground truth data and the decimated maps obtained with the grids. They observed that for the catheter with an IED of 3 mm it was possible to locate the rotors with an error within an ablation lesion dimension, as long as the distance of the electrodes to the heart wall was below 10 mm. For the catheter with 6 mm of inter-electrode spacing, the localization error was deemed unacceptable. In the end, Alessandrini et al. warn that, considering their results, currently available basket catheters should not have sufficient resolution, if fully deployed, to correctly locate arrhythmia drivers.

Yet another simulation study was undertaken by Aronis et al. [82]. They tested not only if rotor localization accuracy was impacted by IED, but also if the number of rotors present was a factor. They used a cardiac tissue model with a spatial resolution of 1 mm and simulated from one to seven simultaneous rotors. Six sub-resolution data sets were generated, with IEDs of 2, 4, 8, 10, 15, and 30 mm. For each sub-resolution, the error of rotor localization was calculated as the distance between the centers of mass of the estimated PSs and the reference PSs. When more than one rotor was present, the error was defined as the distance between the center of mass of each estimated PS and the nearest reference PS. The IED on clinical setting was considered to be 10 mm. For that value, they concluded that the accuracy of ablation targeting would be affected if more than one rotor was present, which is the usual for AF cases. They found that an IED of 4 mm would be sufficient for the localization error (3.2 ± 0.6 mm) to fall within the ablation lesion area, even with multiple rotors present.

Roney et al. looked at resolution requirements for accurate identification of rotors and focal sources as a function of wavelength of the arrhythmia, that is, the distance between wavefronts [83]. The necessary resolution (R) should obey the expression $R = \lambda/N$, where λ is the arrhythmia's wavelength and N is the number of data points between consecutive wavefronts. To test the resolution requirements, the simulated data, with original IED of 0.1 mm, was uniformly downsampled to have IEDs ranging from 1 to 25 mm and interpolated back to the original resolution for comparison. When downsampling the data, it was guaranteed that the chosen data points' positions would be as close to the rotor in the full resolution as possible. The result reached was that N had to be at least 3.1 for correctly identifying rotors and avoiding false detections. This led to their conclusion that basket catheters have adequate resolution to detect rotors, but not enough to rule out false ones. With a value defined for N, it was possible to infer the value of R for the lowest atrial wavelength, in order to obtain the most restrictive resolution requirement. Following this logic, they arrived at the final value of $R = 14.2$ mm and considered most clinically available catheters to have IEDs inside that limit. Therefore, they should be able to correctly detect rotors if positioned over them.

In a more realistic environment, King et al. performed optical mapping on rabbit hearts and compared rotor detection results as spatial resolution decreases [84]. Their study promotes a 2 mm IED as ideal for rotor detection.

When it comes to ventricular tachycardia and fibrillation, there is not much information regarding the effect of spatial resolution on rotor detection and localization, since ablation is not the preferred treatment. However, it is important to understand its impact on VT and VF dynamics and underlying mechanisms. Furthermore, the tendency is for ventricular arrhythmia therapies to become more and more localized, and accurate application of therapy will be essential for their success [39], [85].

To summarize, the overall consensus is that current basket catheters do not provide sufficient rotor detection accuracy, and poor spatial resolution is presented as a possible reason for the equivocal reports of FIRM mapping efficacy [83]. Low spatial resolution leads to various errors in arrhythmia detection, such as missing rotors, the appearance of false rotors, and mislocating rotors. These errors, in turn, cause the erroneous ablation of healthy tissue and failure to apply therapy where it is needed [84]. In terms of what the ideal IED should be for appropriate rotor localization, the reported values varied considerably, likely due to the variations in the resolutions tested.

The majority of the studies on spatial resolution requirements for rotors' detection used cardiac simulation data, which, while useful, does not produce results as reliable as real data. Furthermore, none had access to human data besides clinical data for which it is impossible to effectively test different resolutions. The alternative was animal studies, and while some animal species come close to humans in terms of cardiac physiology, results from animal studies do not always translate to human settings. For the present work, both of those limitations are overcome, as the data analyzed was obtained from optically mapped donor human hearts.

Chapter 3

Methodology

This chapter goes into detail on the protocols and methods used to obtain, process, and analyze the data. The fluorescence data, obtained by optically mapping donor human hearts (Section 3.1), was first filtered (Section 3.3.1) and then translated to the phase domain (Section 3.3.3). From the phase data, it was possible to identify (Section 3.3.7) and track (Section 3.3.8) arrhythmia drivers. After having done so for multiple resolutions, the phase singularities found for the original resolution data were compared with those found for each sub-resolution studied (Section 3.4). The metrics used to evaluate the loss of information as resolution decreases are described and justified (Section 3.6). Additionally, electrical data was processed (Section 3.5.2), so that the results obtained from the optical data could be validated against it (Section 3.5.3).

3.1 Experimental preparation

The experiments were undertaken by Dr. Kedar Aras for a different study, yet to be published. For the purpose of acquiring relevant data, the experiments were conducted on de-identified donor human hearts rejected for transplantation. The hearts were recovered at the time of explantation and treated with similar measures to hearts taken for transplantation: they were cardioplegically arrested and maintained in ice-cold cardioplegia during transport to the laboratory. Cardioplegia is a solution that protects the myocardium by decreasing its electromechanical activity, and therefore its oxygen demand [86].

The goal of the study was to optically map the right ventricular outflow tract (RVOT), which is a common site for the genesis of ventricular tachycardia [87]. To expose the RVOT surface, most of the atria, the LV and the posterior RV were removed. The aorta and the pulmonary artery were dissected open to expose and isolate the right and left coronary arteries for cannulation. The remaining vessel branches were tied off or cauterized. To place the RVOT preparation in a vertical position, it was stretched across a frame and secured to it. The frame was held in an upright position inside a bath to allow optical access to both the endocardial and epicardial surfaces. The bath was temperature-controlled at 37 °C and the heart preparation was perfused under constant pressure (60 mmHg) with oxygenated Tyrode's solution. The tissue was immobilized by blebbistatin (10-15 µM), an electromechanical uncoupler that inhibits muscle contraction, to suppress motion artifacts in optical recordings without adverse electrophysiological effects [88], [89], and stained with the voltage-sensitive dye Di-4-ANBDQBS [90]. Figure 3.1 shows a representative donor human whole heart and a RVOT wedge preparation.

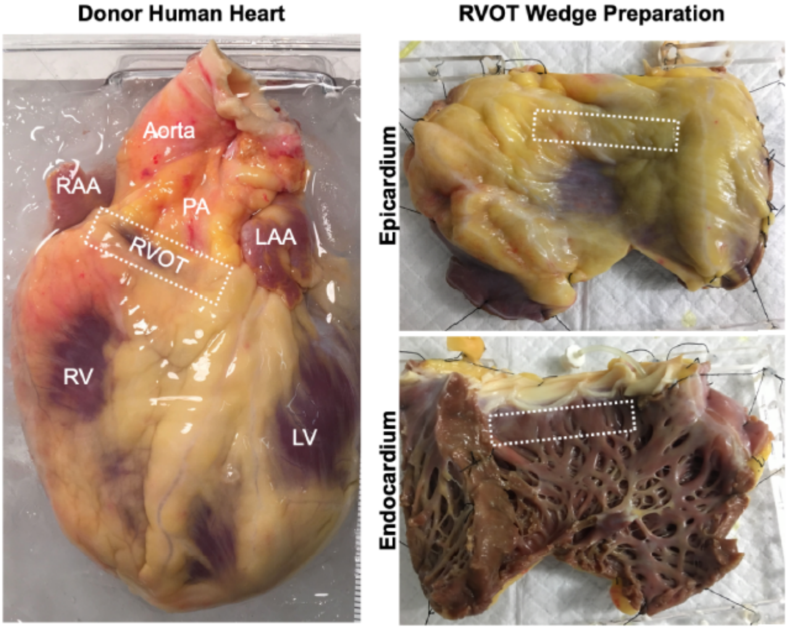

Figure 3.1: Representative donor human heart and right ventricular outflow tract (RVOT) tissue wedge preparation. The RVOT region is identified on the epicardial and the endocardial surface (marked with a white dotted rectangle). RAA, right atrial appendage; PA, pulmonary artery; LAA, left atrial appendage; RV, right ventricle; LV, left ventricle. Courtesy of Dr. Kedar Aras.

Arrhythmia was induced using a dynamic restitution protocol (S1S1), in which the tissue is paced at a steadily increasing rate [91]. When the S1S1 protocol wasn't successful, burst pacing at 50 Hz was used for arrhythmia induction. All induced arrhythmias were sustained and lasted for at least 15 minutes.

The heart wedge was optically mapped from the epicardium and the endocardium using two MiCAM05 (SciMedia, California, USA) CMOS cameras, in a setup similar to the one shown in Figure 3.2. The cameras' resolution was 100 by 100 pixels and the tissue area mapped was approximately 7.0 by 7.0 cm, resulting in a spatial resolution of 700 µm for the optical data. The electrical action potentials were also captured, using a stretchable electrode array, displayed in Figure 3.3.

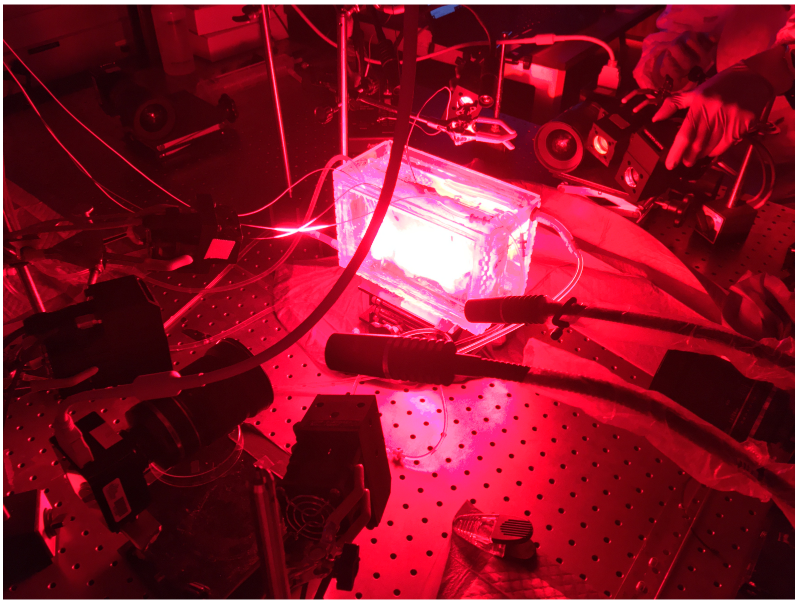

Figure 3.2: Dual-side optical mapping setup. Two MiCAM05 (SciMedia, CA) CMOS cameras stand equidistant on opposite sides of the heart preparation and two red light lamps are pointed to each side of the preparation.

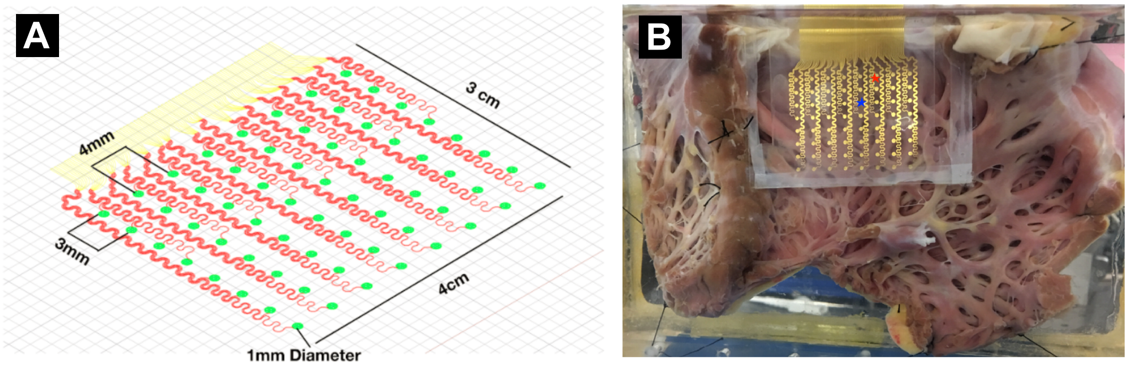

Figure 3.3: Stretchable and translucent array with 64 electrodes to record electrical signals simultaneously with optical signals. **(A)** Device schematic. **(B)** Placement of the array on the endocardium. Courtesy of Dr. Kedar Aras.

3.2 Data description

The data used for this thesis was obtained from 12 de-identified donor human hearts from Washington Regional Transplant Community (WRTC) in Washington, DC. A complete list of hearts with available clinical information is provided in Appendix A. Both sinus rhythm (baseline) and arrhythmic episodes (VF and MVT) were recorded. Table 3.1 presents the number of recordings used per heart and specifies the type of arrhythmia mapped in each heart.

Optical data: Signals obtained from optical mapping represent fluorescence intensity, in arbitrary units. They are recorded in the form of a 100 by 100 matrix per millisecond, each recording lasting 8 seconds. This results in 10,000 signals, each with

8000 data points. Spatial resolution is 700 µm in both directions.

Electrical data: The electrical recordings are voltage signals, obtained from 64 electrodes, and with a sampling frequency of 1000 Hz. The electrode array had inter-electrode distances of 4 mm horizontally and 3 mm vertically, and covered a total area of 12 cm^2, as shown previously in Figure 3.3.

Table 3.1: Summary of experiments. For each experiment, both sides of the heart were recorded simultaneously, so the number of recordings per heart is 2n.

Donor ID	D1	D2	D3	D4	D5	D6	D7	D8	D9	D10	D11	D12
n	3	2	2	2	2	2	2	2	2	2	2	2
Sex	M	F	F	F	M	M	F	M	F	F	M	M
ArrType	MVT	VF	VF	MVT	MVT	VF	VF	VF	VF	MVT	MVT	VF

n, number of experiments for each heart; M, male; F, female; ArrType, arrhythmia type; MVT, monomorphic ventricular tachycardia; VF, ventricular fibrillation.

3.3 Optical data processing

The processing of optical data to extract arrhythmia dynamics was done using the Cadence software, developed by Dr. Kedar Aras [92]. First, the data was filtered (Section 3.3.1). Then, the filtered data was translated to the phase domain (Section 3.3.3), where it is possible to identify (Section 3.3.7) and track (Section 3.3.8) arrhythmia drivers. Extra to the Cadence processing, the data was upsampled (Section 3.3.5) and downsampled (Section 3.3.4) in order to create sub-resolution maps. After tracking PSs for multiple resolutions, the phase singularities found for the original resolution data were compared with those found for each sub-resolution studied (Section 3.4). The PSs taken into consideration had to last longer than the minimum cycle length (CL), and the method to compute the CL for each recording is presented in Section 3.3.2. All data processing was performed in MATLAB version 2021a [93].

3.3.1 Data filtering

The fluorescence data was converted from a CMOS file to a Matlab matrix and preprocessed through the following steps [94].

1. *Spatial binning:* The data was spatially smoothed to decrease noise by replacing each pixel with the average of itself and its neighbors. To that end, the data matrix was convoluted with a matrix of ones (Matlab function `conv2`), whose size depended on the number of neighbors to be included in the averaging. For this work, a matrix of 5 by 5 (24 neighbors) was chosen. Other matrix sizes were experimented with, and 5 by 5 removed sufficient noise without over-smoothing.

2. *Powerline noise removal:* The powerline noise at 60Hz was removed from the recordings using an infinite impulse response band-stop filter.

3. *Temporal filtering:* The signal of each pixel was temporally filtered using the Parks-McClellan Remez Exchange algorithm, available as the Matlab function `firpm`, which applies a finite impulse response signal processing filter to the data. The low and high band-pass threshold frequencies chosen were 0 Hz and 100 Hz, respectively. These values were deemed appropriate since the experiments were made on isolated heart wedges, without the interference of other physiological functions [84]. The filter may cause a temporal shift, so a zero-phase filter was also used (Matlab function `filtfilt`).

4. *Drift correction:* A fourth-degree polynomial function is fitted to the signal of each pixel using `polyfit`. The polynomial is then subtracted from the signal to remove any existing drift.

3.3.2 Cycle length calculation

After filtering the data, the dominant frequency (DF) and the CL are extracted. The dominant frequency corresponds to the highest peak of the discrete Fourier Transform of the signal, that is, the frequency that carries the most energy [95]. It is obtained for each pixel and therefore provides information about the cardiac rhythm and its stability across the myocardium.

The cycle length is the time period between activations. Since the relationship between frequency (f) and the period (T) of a sinusoidal signal is given by

$$T = \frac{1}{f} \tag{3.1}$$

the inverse of DF already gives an idea of what the CL should be. However, a more accurate estimate of CL was attained by finding the activation peaks of the signal for each pixel and calculating the median of the difference between consecutive peaks. The Matlab function `findpeaks` was employed for this end and the median value of DF was used to determine target times to aid the peaks' detection.

The CL was computed for each pixel. The lowest value of CL for each recording was considered the minimum CL.

3.3.3 Phase mapping

The conversion of fluorescence data to phase angle involved preparing the data and applying the Hilbert transform. The phase mapping process is illustrated in Figure 3.4. The first step of this operation is to subtract the mean from the signal (Figure 3.4A), since the phase calculation is sensitive to constant components [96]. Let $f(t)$ be a filtered fluorescence signal. The zero-mean signal $\tilde{f}(t)$ is obtained through

$$\tilde{f}(t) = f(t) - \overline{f(t)}, \tag{3.2}$$

with $\overline{f(t)}$ as the mean value of $f(t)$. Then, the signal is inverted, so that the phase cut matches with the cardiac depolarization (Figure 3.4B). The Hilbert transform was performed using the Matlab function `hilbert` from the Signal Processing Toolbox, which returns an analytical signal, $z(t)$, with the signal and its Hilbert transform as complex conjugates (Figure 3.4C):

$$z(t) = \tilde{f}(t) + iH\left[\tilde{f}(t)\right]. \tag{3.3}$$

In the phase-space, the real and the imaginary parts of $z(t)$ are plotted against each other (Figure 3.4D) and the phase angle, θ, can be computed for each instant [97]. This relationship is described by

$$\theta(t) = \arctan\left[\frac{imag\{z(t)\}}{real\{z(t)\}}\right] = \arctan\left[\frac{H[\tilde{f}(t)]}{\tilde{f}(t)}\right]. \tag{3.4}$$

The resulting phase data varies from -π to +π, corresponding to a complete cycle of the cardiac action potential (Figure 3.4E).

Algorithm optimization

The conversion of fluorescence data to phase adds noise to the data. Noisy phase maps are prone to phantom PSs and make it harder to track the real ones. Therefore, spatial binning after phase mapping was added to the algorithm. The phase data was smoothed using the same method as the fluorescence data spatial binning (Section 3.3.1). However, to avoid noise in the transition line from -π to +π, the phase angle data (θ) had to be converted to its exponential form ($e^{i\theta}$) before spatial smoothing and reverted afterward. When applied directly, the smoothing operator does not respect the discrete transition between -π and π, as seen in Figure 3.5. This method, as done by Dr. Caroline Roney [98], successfully avoids the erroneous transition.

To verify if this step would be beneficial to track PSs and, consequently, a useful addition to the algorithm, the results of PS tracking with or without phase binning were compared for one recording. It was observed that smoothing the phase data facilitated tracking and prevented some PSs to be temporally broken into shorter duration ones. An example of this occurrence can be viewed in Figure 3.6. Furthermore, it reduced the number of false rotors detections.

3.3.4 Downsampling

To test the effect of lower resolutions, the data was uniformly decimated by $\mathbb{D}$ downsampling factor, where $\mathbb{D} \in \{2,3,4,5,6,7,8,9,10\}$. The pixels that were collected were considered pseudo-electrodes, as they mimic the information obtained from electrical mapping. This was achieved by creating an interpolant based on the original data matrix through the Matlab function `griddedInterpolant`. The interpolant was then used to extract the values corresponding to the uniform grid for each sub-resolution.

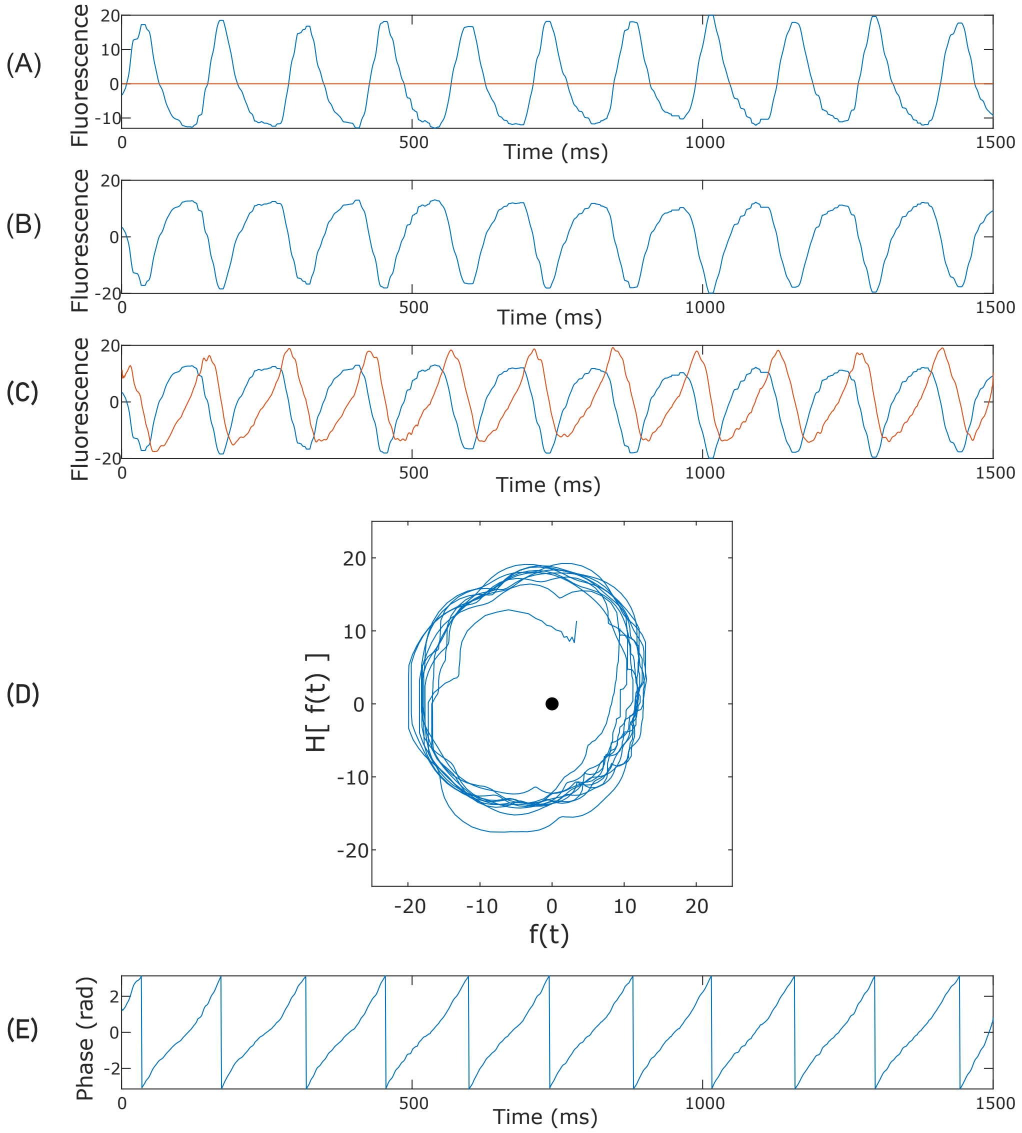

Figure 3.4: Phase mapping process. **(A)** The filtered signal (blue) and mean of the signal (orange), which in this case is zero. Therefore, the signal remains the same after subtracting the mean. **(B)** The signal is inverted so that the phase cut matches the signal's peaks. **(C)** Inverted signal (blue) and its Hilbert transform function (orange), with a phase-shift of 90°. **(D)** Inverted function is plotted against its Hilbert transform. **(E)** Phase angle from graph (D), plotted in time. The transition from π to -π corresponds to the filtered signal's peaks, and each segment from -π to π corresponds to one cardiac cycle.

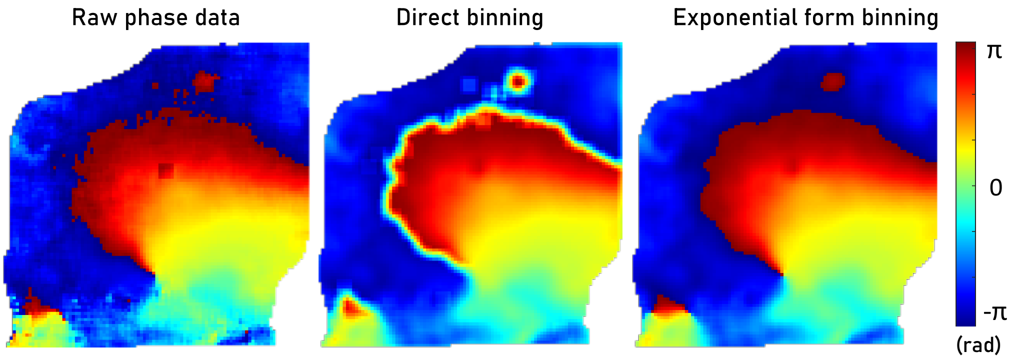

Figure 3.5: Spatial binning was applied after converting phase angle to exponential form. Phase data binning was performed to reduce noise. The data had to be converted to its exponential form before spatial averaging to avoid issues in the transition from π to -π. After smoothing, the data was returned to phase angle. In this case, the bin size of the smoothing operator was 5 by 5 pixels. Method by Dr. Caroline Roney [98].

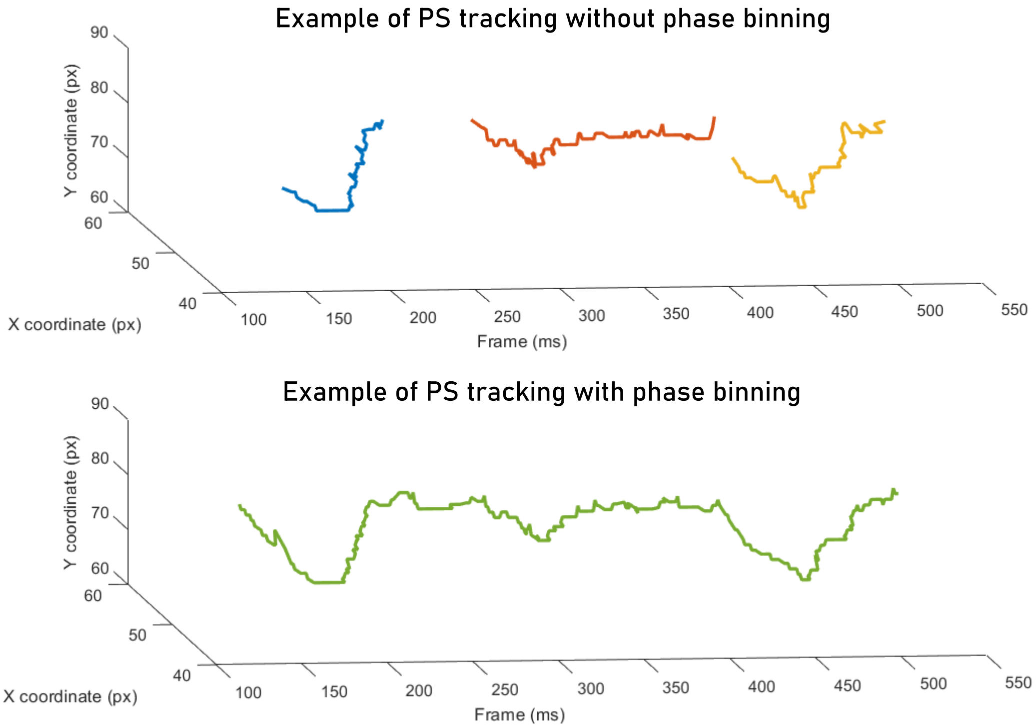

Figure 3.6: Comparison of phase singularity (PS) tracking precision with or without phase binning. Each line segment in the graphs corresponds to a PS, represented by their spatial coordinates through time. The three rotors detected without phase binning for this temporal segment (top) correlate with a single rotor detected when spatially averaging the phase data (bottom).

As default, the grid was positioned starting in the upper left corner of the original data matrix. However, to study the effect of the grid position on the results, three other placements were tested for $\mathbb{D} = \{2, 5, 10\}$. These sub-resolutions were chosen to provide a range of high, intermediary, and low spatial resolutions.

The downsampling was performed after filtering and phase mapping because optical data is very noisy and downsampling before its filtering would not provide realistic or reliable results. The impact of downsampling before or after phase mapping was none since the conversion is done on a pixel basis, therefore that choice was arbitrary.

3.3.5 Upsampling

The decimated data was upsampled back to the original resolution immediately after downsampling so that comparison with the original data would be possible. The Matlab function `griddedInterpolant` was again used, in this instance to create an interpolant based on the sub-resolution data matrix. By employing the interpolant, the values corresponding to the lost data points were computed through interpolation.

Three interpolation methods were tested to determine which would provide the highest fidelity: bilinear, bicubic, and cubic spline. Bilinear and bicubic are extensions of linear and cubic interpolation for two-dimensional data. Bilinear interpolation connects the known data points with a straight line, bicubic interpolation uses a cubic convolution kernel, and cubic spline uses spline interpolation. A representation of the behavior of the different methods for one-dimensional data is displayed in Figure 3.7.

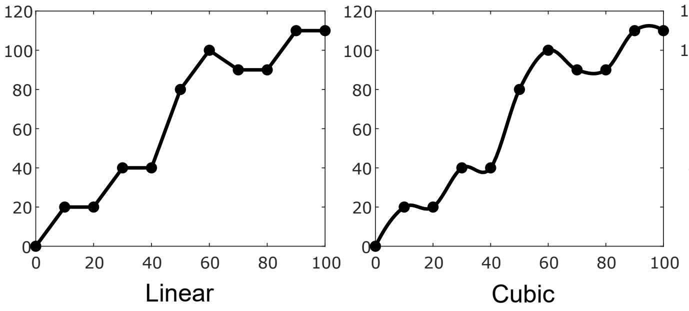

Figure 3.7: Visual representation of different interpolation methods for one-dimensional signals. Adapted from [99].

3.3.6 Data masking

Optical data is prone to noise and the data's quality may not be spatially uniform. Therefore, to only analyze the meaningful and relevant areas of the recording, a data mask is created based on a baseline recording and applied to the arrhythmic data. This step is performed after upsampling to avoid loss of information at the mask border.

3.3.7 Phase singularity detection

An arrhythmic episode may be caused by an anatomic or functional anomaly in the tissue conductivity, inducing a reentrant pathway. When reentry occurs, a conducting wavefront re-excites part of the cardiac tissue through which it had passed already, pivoting around a core of unexcited but excitable cardiac tissue. This phenomenon can be recognized in phase maps as a phase singularity, a point where the range of cardiac excitation values merges. Therefore, a PS is found by detecting sharp variation in the phase map, both horizontally and vertically.

To identify those points, the partial derivative is calculated in both directions, resulting in two separate matrices for each time frame. The resulting values are adjusted to remain between -π and +π, replacing those higher than +π and lower than -π in the following manner:

$$\pi + a \Rightarrow -\pi + a \wedge -\pi - b \Rightarrow \pi - b, \text{ for } a, b > 0 \tag{3.5}$$

The Sobel edge detection operator was convoluted with each matrix, its direction corresponding to the partial derivative direction. Both matrices were summed for each time frame, resulting in an overall variation description through time. Since both directions are taken into account, the variation of the isophase line when π transitions to -π is overlooked and only phase singularities, which represent a phase jump in every direction, are recognized.

The phase jumps were expected to be ±2π and a tolerance of 3 rad was deemed appropriate [98]. Consequently, values superior to 2π-3 rad were considered clockwise PS candidates, while those inferior to -2π+3 rad were considered anti-clockwise PS candidates. Figures 3.8A and 3.8B represent a clockwise PS and its detection by the Sobel operator, respectively. As shown in the figures, each PS is defined by four pixels in a square, that is, four neighboring PS candidates. To avoid mistakenly tracking more than once the same PS, the neighborhood rule was added to the algorithm.

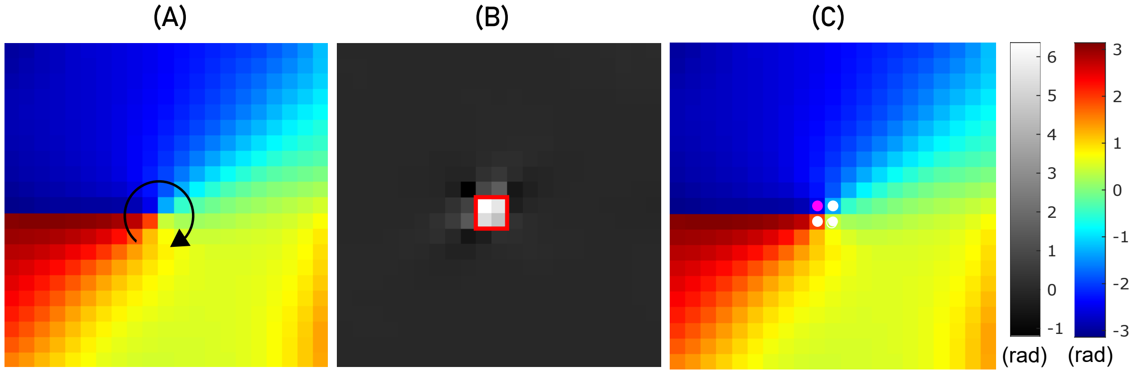

Figure 3.8: Phase singularities detection process. **(A)** Section of one instantaneous phase map where one clockwise phase singularity is present. **(B)** Output of the convolution of the partial derivatives of the phase map with the Sobel operator. The red square delimits a neighborhood of four pixels that have a high enough phase variation to be considered phase singularity (PS) candidates. Since the neighborhood has at least four members, it is not discarded as noise. The neighbor with the highest absolute value is selected to represent the PS. **(C)** Phase map with the PS candidates neighborhood marked by the dots. The pink dot signals the selected candidate and the remainder are in white.

Algorithm optimization

The neighborhood rule was developed by Dr. Caroline Roney [98]. When a PS candidate pixel is found, it verifies how many of its neighbors are PS candidates as well. If the pixel is inserted in a neighborhood of at least four pixels that are PS candidates and that have the same chirality, then the neighborhood is deemed a PS. If the neighborhood has less than four pixels, then it is considered noise.

After assessing that the neighborhood represents a true PS, the pixel with the highest variation in its neighborhood is appointed as the location of the PS. This step reduces computation time and makes the code more robust against PS candidates in the same neighborhood being accounted as different PSs, such as in the example in Figure 3.9A. Furthermore, ignoring isolated candidates avoids false detections on the border of the data mask, as shown in Figure 3.9.

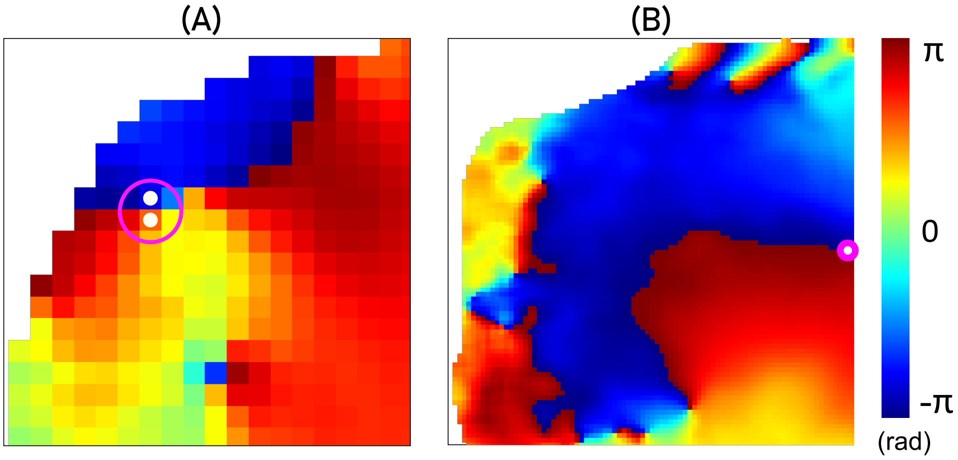

Figure 3.9: Examples of wrong phase singularity detections that can be avoided with the neighborhood rule. **A.** Double detection of the same phase singularity. The white dots identify the phase singularities detected and are emphasized by the magenta circle. **B.** False phase singularity due to the image border, marked with a magenta circle.

3.3.8 Phase singularity tracking

In order to assess the lifespan and movements of each PS, it is necessary to track them through time and establish each individual path across the myocardium. To do so, a Matlab object is created for every PS in every frame, with its location and chirality set as properties.

For every frame in the recording, the PSs present are analyzed. If a PS is not already assigned to a path, its frame and index number are added to the PS object properties as the starting point of a new path. Then, its position is compared against the PSs in the next five frames. If a PS is found within a 2-pixel (1.4 mm) radius from the previous one and with matching chirality, it is deemed to be the same PS and added to the path. The choice of 1.4 mm for the allowed spatial displacement of the PS between frames is based on the maximum velocity of action potential propagation, which is 100 cm/s [100], [101]. Therefore, for a temporal displacement of 1 ms between frames, a PS's maximum movement should be 1 mm due to physiological constraints. However, the spatial threshold should not be a fixed value but instead depend on the temporal displacement. For example, if due to noise the PS is only detected again after three frames, the movement allowed should be 3 mm. The fixed value was implemented and thus constitutes a limitation to the current work.

For every PS added to a path, the path's lifespan, distance covered, and displacement between its initial and final positions are updated. PSs lasting less than 50 ms were considered noise and not taken into account. The reasoning behind the temporal threshold of 50 ms was that some PSs were found in baseline recordings with lifespans up to 40 ms. Since these recordings represented sinus rhythm and, therefore, possessed no real PSs, it was confirmed that signal noise produced phantom rotors that could last that long. Consequently, as a precaution, all PSs detected in arrhythmic signals that lasted less than 50 ms were discarded as potential illusory rotors.

Algorithm optimization

For PS tracking, the Cadence software was optimized by adding a PS blacklist. It was observed that, in some occasions, one noisy PS point or PS segment could appear near another PS trajectory and, due to its proximity, account the other's future trajectory as its own. Consequently, some PSs would appear repeated, as in Figure 3.10. To eliminate these cases, every instantaneous PS assigned to a trajectory was added to the PS blacklist and would not be taken into account for future PSs being tracked.

3.3.9 PS density maps peak detection

PS density maps provide an additional method to evaluate PS detection and, more specifically, its localization accuracy, since these maps allow the spatial visualization of PSs' distribution [81]. The density maps were created by counting the phase singularities' occurrences in each pixel. For every phase singularity lasting longer than 50 ms, its path was registered by incrementing the PS count of the location where it appeared in each frame. To better compare the maps from different resolutions, and to better visualize PS distribution, the density maps were spatially averaged with a 3x3 pixels bin, as shown in Figure 3.11. This bin size has been used by Dr. Roney for this finality and was deemed sufficient to visualize PS conglomerates in density maps [98].

To detect the density peaks, the Matlab function `imregionalmax` was used. This function finds the regional maxima in a given image. This method, however, led to the detection of not only the true peaks but also of any slight peaks in low-density regions. To isolate the true peaks, some conditions had to be implemented. First, a minimum density was defined. To do this, the pixel with the highest PS density was detected and for any other possible peaks to be considered so, their PS density had to be at least 75% of the value of highest density. This step cut the false low-density peak detections. The second condition aimed at avoiding multiple detections of the same peak. For any potential PS density peak, the pixels within a certain radius were taken into account, to verify if there

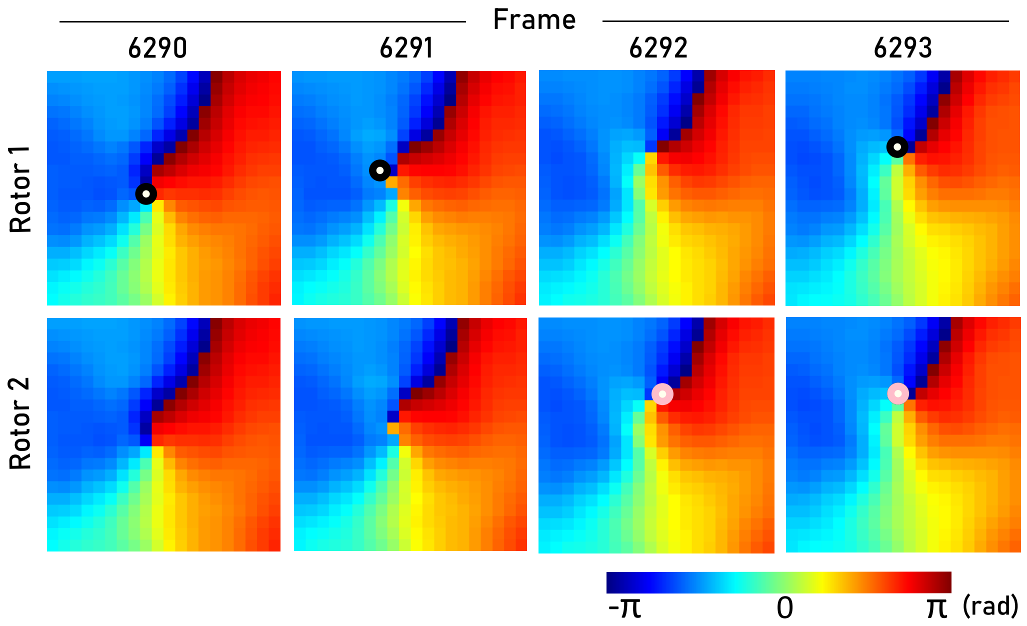

Figure 3.10: Rotor overlap without phase singularity blacklist. The figure shows a four seconds segment of two separate PS trajectories detected, Rotor 1 and Rotor 2. Rotor 1 starts in frame 6269, while Rotor 2 appears in frame 6292 displayed in the Figure. Rotor 1 is lost in frame 6292 due to the spatial distance between instantaneous PSs, but is reconnected in frame 6293. However, since the PS did not disappear in frame 6292, it was simply too distant, there is an instantaneous PS that is detected and used to start a new trajectory. From frame 6293 forward, the paths of Rotor 1 and Rotor 2 are exactly the same. Thus, Rotor 2 is a duplication of a portion of Rotor 1. To prevent duplicate PSs, the PS blacklist is applied and, for the presented case, Rotor 2 is not detected anymore.

were other possible peaks nearby. If so, the highest peak was kept and all other peaks in the neighborhood were discarded. This conditioning is illustrated in Figure 3.12.

3.4 Correlation between original and decimated data

With the main objective of analyzing the effects of decreasing spatial resolution on arrhythmia drivers' dynamics, it is necessary to assess if the PSs found for the original resolution are also present in the decimated maps and how they differ. Like so, when analysing density maps it is also necessary to appraise the corresponding peaks in the original maps and in the sub-resolution maps. Thus, this section describes how these correlations were established for both the individual PSs and the PS density map's peaks, and explains which information was retrieved from them.

3.4.1 Tracked phase singularities

For each sub-resolution it was substantiated which, if any, of the PSs correlated spatially and temporally with the ones from the original maps. When comparing the PSs present

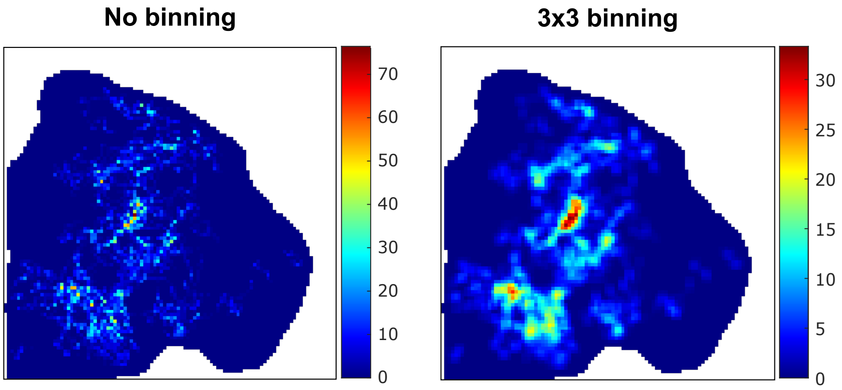

Figure 3.11: Phase singularity density maps with and without spatial averaging. Since phase singularities are not expected to be static, the averaged density map gives a more realistic notion of where phase singularities are present and where they are concentrated. A 3 by 3 pixels bin was used for the convolution [98].

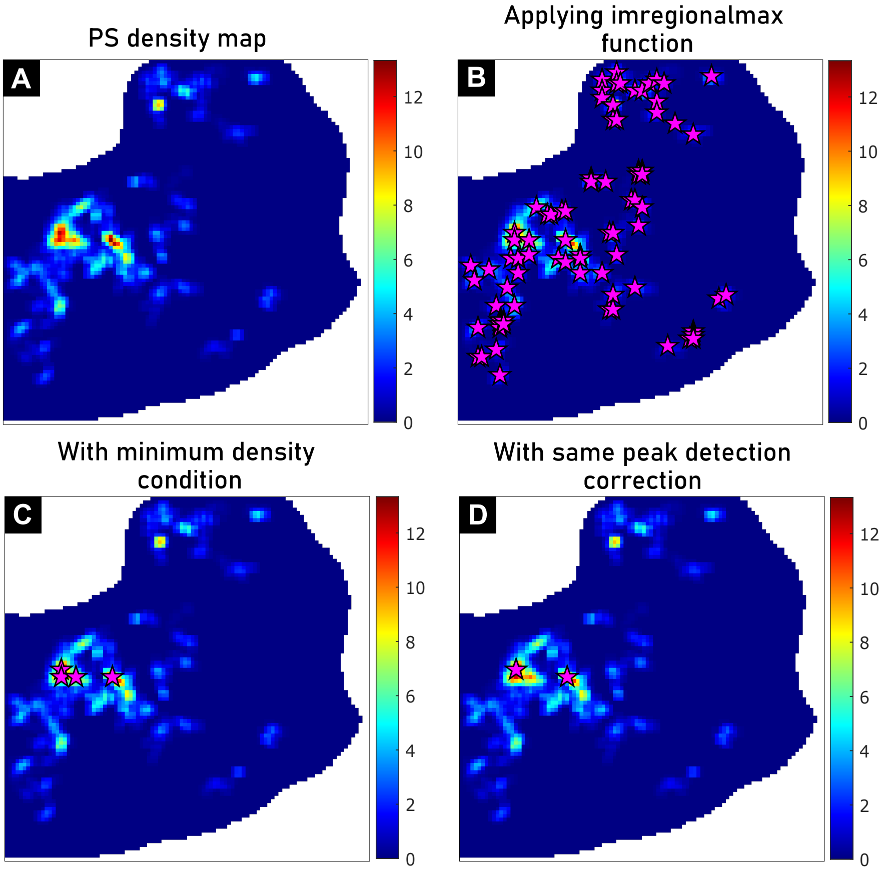

Figure 3.12: Detection and conditioning of phase singularity density peaks. Peak detections are represented by pink stars. **(A)** Representative PS density map. **(B)** Peak detection through Matlab function `imregionalmax`. Every deflection is considered a peak. **(C)** Peak detection after applying the minimum density conditioning. Only peaks with density equal or superior to 75% of the highest peak are taken into consideration. **(D)** Final density peaks after correcting multiple detections of the same peak. Only the highest peak within a certain radius is considered a true peak.

in the original map and a decimated map, all possible pairings were analyzed one by one. Four conditions had to be fulfilled for a correlation to be drawn:

Condition 1. Lifespan longer than the minimum CL.

Only stable rotors were considered for correlation. A stable rotor (SR) was defined as lasting longer than the minimum CL of the recording, based on the work by Bayer et al. [102] but adapted for each dataset. To be noted that one of the donor hearts studied (identified as D3 in Table 3.1) had no stable rotors.

Condition 2. Same chirality.

PSs have to rotate in the same direction to be considered equivalent [84].

Condition 3. Share at least a quarter of the lifespan.

By changing the resolution of the data, the signal will distort and, in some instances, the flow of a rotor's path might be broken. The path is still present but separated into shorter-lasting fragments. To allow these fragments, if lasting longer than the minimum CL, to be recognized as a match to the original path, the temporal restrictions have to be balanced. Therefore, while the rotors do not have to appear and disappear at the same time or have a similar lifespan, they must temporally correlate for at least a quarter of their duration.

Condition 4. Minimum spatial displacement of 5 pixels.

The distance between the PSs' locations was measured for each shared frame. To be considered the same rotor, the mean distance between PSs' locations had to be, at most, 5 pixels, which corresponds to 3.5 mm. This value coincides with the mean radius of a tissue ablation lesion and therefore was considered an acceptable margin of error. This distance was taken as default but in Section 4.2.3 other values were also used.

The correlation process was divided into three steps. First, the primary matches were established, where each rotor was only allowed to match once. Thus, if for any of the resolutions there were fragmented drivers, the matching rotor would only correlate with one of the fragments. This first take separates the rotors into three groups: the successfully matched, with the established pairings; the missed rotors, which were the uncorrelated PSs from the full resolution data; and the false rotors, which were the uncorrelated PSs from the sub-resolution data.

The second step was to check for correlations between the missing rotors and the sub-resolution PSs. The objective was to confirm if the rotors were in fact missing or if multiple PSs from the original data represented a single PS from the decimated data. If any such pairing was found, the PS would be removed from the missing rotors bin and entered in a new division, the mistakenly missed.

Lastly, the same logic was applied to the false rotors and the mistakenly false rotors were separated from the actually false ones.

In the end, the number of found rotors, which represents all the stable rotors from the original resolution that are identified in the sub-resolution maps, is given by the sum of the initially matched rotors with the falsely missed rotors.

3.4.2 Phase singularity density peaks

In the case of PS density maps peaks, the position of each peak in the original maps was compared against the position of every peak in each sub-resolution. Correlation was deemed successful if the peaks in the decimated maps were within a radius r from a true peak. To test the correlation success for different spatial accuracy requirements, multiple r values were explored (1.4 mm, 2.1 mm, and 3.5 mm).

The number of found peaks is the number of original peaks found in a sub-resolution PS density map, the number of missed peaks is the amount of original peaks not found, and the number of false peaks is the quantity of erroneous peaks found in the sub-resolution map that are not present in the original.

3.5 Validation with electrical data

The optical maps were compared with the data from the electrodes array, to confirm correlation of the signals. To do so, the electrical signals had to be processed and converted to phase. This data processing was different from the fluorescence data's. First, the data was cleansed of signals that were too noisy. Then, the data was filtered and its derivative was used to find the activation temporal sites. After phase mapping, the data was interpolated to match the corresponding area in the optical maps.

3.5.1 Electrical data cleansing

Not all electrodes recorded good quality signals, so noisy recordings had to be discarded. The non-viable signals were visually identified, as they had no recognizable depolarizations and were very irregular, as shown in Figure 3.13, and manually removed.

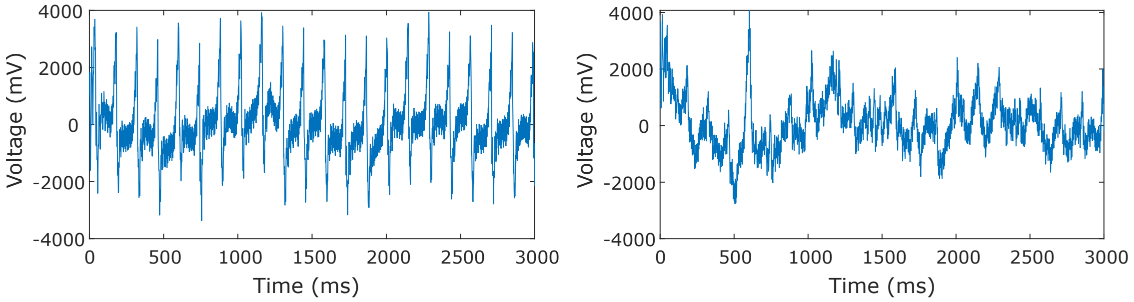

Figure 3.13: Representative signals of viable and non-viable electrical raw data. The viable signal, on the left, has clear activations, while the non-viable one has no distinguishable activation points and no organization.

3.5.2 Electrical data processing

The electrical signals are different from fluorescence signals, and therefore need a separate filtering process, that goes as follows.

1. *Temporal filtering:* Each electrical signal was band-pass filtered using a high-pass threshold of 2 Hz and a low-pass threshold of 40 Hz. These filtering settings removed high-frequency noise, as seen in Figures 3.14A and 3.14B, and provided a slight drift correction, thus effectively cleaning the action potential signals. The Parks-McClellan Remez Exchange algorithm was used for this step, as had been for the optical data temporal filtering.

2. *Derivative:* In order to detect the depolarizations, the derivative of the signals was extracted, as shown in Figure 3.14C [98].

3. *Squaring:* To enhance the signal's peaks, which correspond to the depolarizations, each signal was squared, as in Figure 3.14D [98].

4. *Invert data:* For the phase transitions to match the signals' depolarizations, the signals were inverted, as shown in Figure 3.14E.

5. *Smoothing:* A moving average was applied to the signals, with a moving window of 50 frames. The objective was to bring the signal as close as possible to a sinusoidal shape, and therefore resemble more accurately a fluorescence signal, so that the shape of the phase signals was similar and comparable [103]. The averaging was done twice, to achieve the desired shape, illustrated in Figure 3.14F.

The conversion to phase was done as explained for the optical data, in Section 3.3.3. Figure 3.14G represents a phase signal obtained from electrical data.

3.5.3 Comparison with optical maps

Just as sub-resolution optical maps had to be upsampled back to the original resolution to enable comparison between the different maps, the same logic applies to electrical data. To precisely compare the matching electrical and fluorescence signals, the positions of the electrodes in the optical mapping field of view were identified to create an electrode mask, as illustrated in Figure 3.15. This mask with the electrodes' positions was both used to interpolate the electrical data, using the Matlab function `scatterInterpolant`, and to downsample the optical data to 64 signals as obtained for the electrical data. The temporal signals and the phase maps for the electrical and the optical data were visually compared.

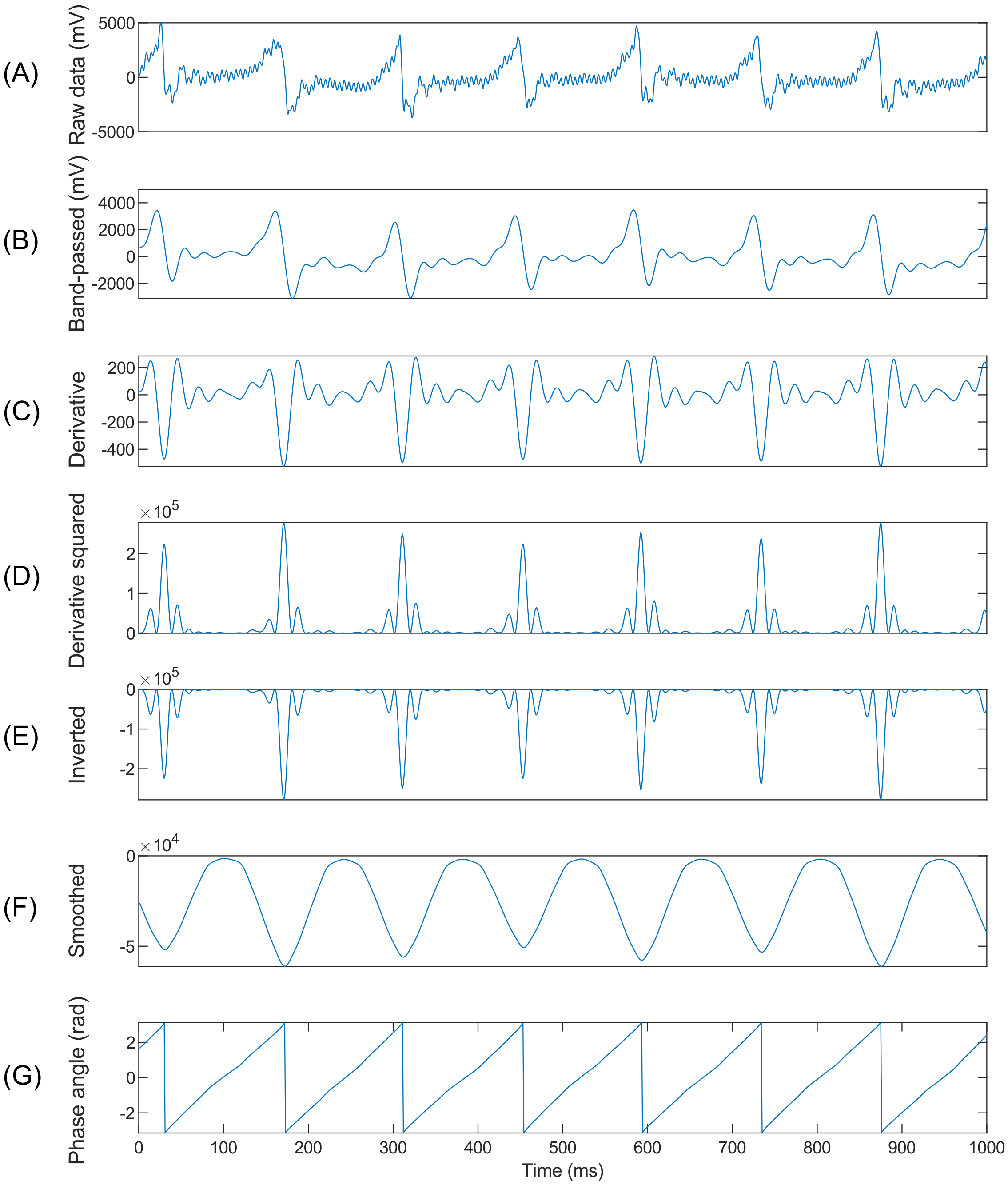

Figure 3.14: Steps for filtering electrical data and converting it to phase. **(A)** Raw electrical data, which had been preprocessed at the time of acquisition with a band-pass filter of [0 200] Hz and notch filtering. **(B)** Data after frequency filtering with a band-pass of [2, 40] Hz. **(C)** Approximate derivative of the signal. **(D)** The derivative is squared to enhance the peaks. **(E)** Signal is inverted so that the phase branch cut matches the depolarization. **(F)** The signal is smoothed twice with a moving average window of 50 frames, to resemble a sinusoidal wave and provide a cleaner phase signal. **(G)** Phase angle signal.

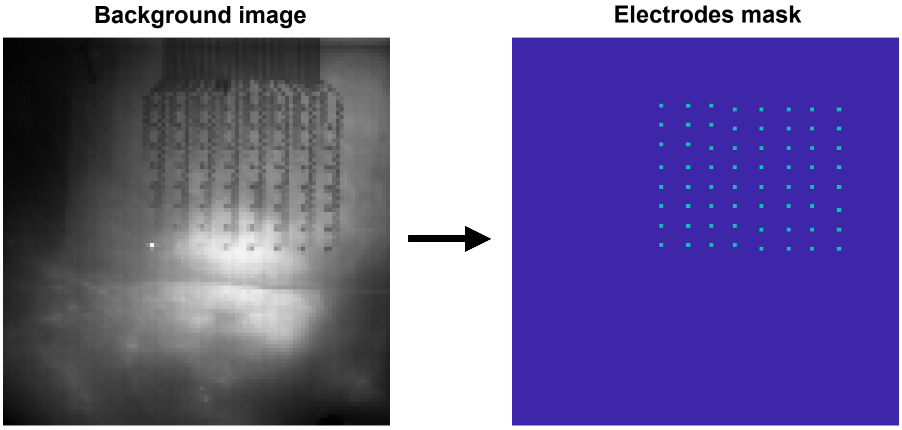

Figure 3.15: Electrodes mask obtained from the position of the electrodes visible in the background images of the optical recordings. This mask was used as a reference for both the downsampling of the optical data and the interpolation of the electrical data.

3.6 Arrhythmia dynamics' metrics

- **Incidence**

  Phase singularity incidence refers to the number of PSs present in each recording, and it was measured as the total number of PSs found in the 8-second recording divided by the data mask area. The number of PSs is informative regarding the stability of the arrhythmia, as more chaotic rhythms have a higher incidence of PSs.

- **Duration**

  The duration, or lifespan, of a phase singularity is the time period from the instant the PS appears to when it disappears. For therapy purposes, the longer-lasting rotors are the ones considered relevant. Therefore, a significant variation in this value would have an impact, as important information may be hidden or lost. This metric was calculated for all PSs and also just for stable rotors. If for any resolution of a given recording no rotors were detected, the duration value is omitted.

- **Displacement**

  Displacement is given by the two-dimensional Euclidean distance between each PS found in a sub-resolution map and its original counterpart, if a successful correlation is made. The Euclidean distance measures the length of a line segment connecting two points [104]. For two dimensions, it is given by

  $$d(p,q) = \sqrt{(p_x - q_x)^2 + (p_y - q_y)^2}, \tag{3.6}$$

  p_x and q_x being the horizontal coordinates of points p and q, and p_y and q_y the vertical coordinates. For each sub-resolution of each recording, the mean and maximum displacement were extracted. For the cases where no rotor was found in the original optical map, there was effectively no displacement to be measured, so the value was omitted.

- **F1-score for rotor detection**

  To verify the correlation success for each sub-resolution, three measures had to be taken into account: the number of true rotors found, the number of rotors missed, and the number of false rotors. These can be described in the following manner:

  True positive True rotor found in sub-resolution.

  False positive False rotor found in sub-resolution.

  False negative True rotor not found in sub-resolution.

  This definition makes it possible to apply algorithm performance metrics, such as precision and recall (also known as sensitivity) [105]. Precision is the ratio of the true rotors found to all the rotors found in a sub-resolution (Equation 3.7), while recall provides the ratio of the true rotors found in a sub-resolution to all the rotors found in the original resolution (Equation 3.8).

$$\text{Precision} = \frac{\text{True positives}}{\text{True positives} + \text{False positives}} = \frac{\text{Rotors found}}{\text{Rotors found} + \text{False rotors}} \tag{3.7}$$

$$\text{Recall} = \frac{\text{True positives}}{\text{True positives} + \text{False negatives}} = \frac{\text{Rotors found}}{\text{Rotors found} + \text{Missed rotors}} \tag{3.8}$$

  Precision and recall can be summarized by the F1-score, which is the harmonic mean of the two metrics [105]:

$$\text{F1-score} = 2 \times \frac{\text{Precision} \times \text{Recall}}{\text{Precision} + \text{Recall}} \tag{3.9}$$

  The F1-score has been used to evaluate PS detection algorithms [106] and was chosen to evaluate correlation performance in this work. It ranges from zero to one: zero if no correlation is made and one if all the original rotors are found and no different rotors are detected. For the cases where no rotor was found in the original optical map, the F1-score was omitted.

- **F1-score for PS density map peaks**

  The peaks of the PS density maps were used to assess if the locations with highest PS incidence were the same across resolutions. To compare the PS density peaks of multiple sub-resolution in regard to the original, the F1-score was used again. In this instance, true positives are the correctly found peaks, false positives are the erroneous density peaks, and false negatives are the undetected density peaks.

3.7 Categorical analysis

The rotor data extracted from the optical recordings was further analyzed according to following inherent characteristics.

- **Arrhythmia type**

  MVT and VF recordings were analyzed separately to assess type specific arrhythmia dynamics and rotor detection accuracy.

- **Sex**

  Sex differences analysis was performed by discriminating the recordings obtained from female and male donors.

- **Anatomical region**

  To verify and take into account possible regional differences in arrhythmia dynamics, the field of view was divided into three sections: the RVOT region, the mid-ventricular (MID) region, and the apical (API) region. This division is showcased in Figure 3.16. The area of the data mask in each region was taken into account for analysis.

- **Mapped surface**

  For every experiment, the endocardium and the epicardium were mapped simultaneously. The results obtained for each surface were compared.

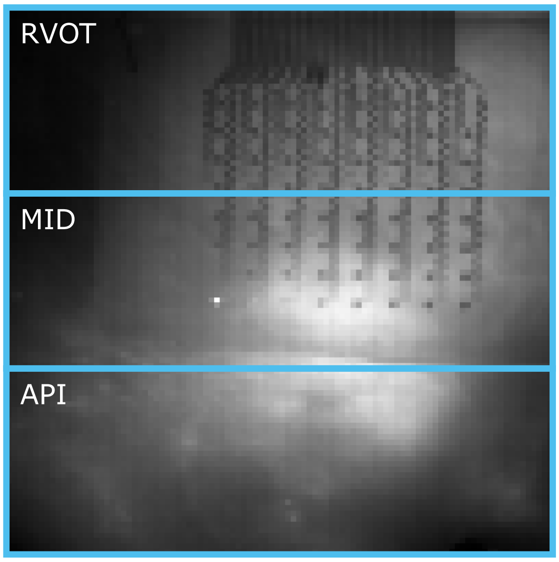

Figure 3.16: Division of field of view for regional analysis. RVOT, right ventricular outflow tract; MID, mid-ventricular region; API, apical region.

3.8 Statistical analysis

The samples presented are the average of all recordings for each donor heart. All means that characterize average trends across the cohort of donor hearts are reported as sample mean ± standard error of the mean (SEM). The SEM was chosen in detriment of standard deviation since it measures how far the sample mean is from the true population mean. When studying accuracy profiles, the 95% confidence interval of the mean is also presented. All datasets were assumed to have a normal distribution, since the metrics analyzed are derived from normal data. Incidence, duration, and displacement metrics are displayed as box and whiskers plots, with the box limits marking the quartiles and the whiskers the minimum and maximum values.

To compare the differences in a single metric due to spatial resolution, repeated measures one-way ANOVA tests were performed. To compare variability between groups, such as arrhythmia type or anatomical regions, repeated measures two-way ANOVA tests were performed. For repeated measures ANOVA tests, sphericity was not assumed and corrections were made using the Greenhouse-Geisser method. Variance homogeneity was verified through the Brown-Forsythe test and Bartlett's test. When relevant, post hoc multiple comparisons tests were performed. To compare group means for each resolution, Tukey's test was used when comparing three groups (such as anatomical regions: RVOT, MID and API) and Šídák's test was used when comparing two groups (such as arrhythmia type: MVT and VF). The Dunnett's test was used when comparing group means for each sub-resolution against the ground truth, only possible for rotor incidence and duration. In the case of duration, oftentimes values were missing if there were no rotors present. When values where missing, a mixed-effects analysis was performed instead of an ANOVA test. Significance was defined as $p < 0.05$. The statistical analysis was performed in GraphPad Prism version 9.2.0 (332) [107].

Chapter 4

Results and Discussion

In this chapter the results are presented and interpreted. Firstly, the concept of using optical data to draw conclusions for electrical data is validated. Secondly, the impact of methodology in the results is analysed. Then, the effect of spatial resolution is evaluated for arrhythmia characteristics, and the detection and localization of rotors. After, the data is discriminated by inherent characteristics (arrhythmia type, sex, anatomical region, and mapped surface) to understand how arrhythmia dynamics and rotor detection may differ. Lastly, detection and localization accuracy profiles are presented and analyzed.

4.1 Is there a correlation between electrical and optical data?

This thesis assumes that the fluorescence data obtained from optical mapping directly correlates with electrical data. That assumption allows the translation of the findings from optical data to devices using electrical data. Therefore, a crucial first step was to confirm that there is a direct correlation between electrical and optical data. Electrical data was only successfully acquired for one heart, so this analysis was limited to that sample.

In Figure 4.1A, a segment of simultaneously recorded electrical and fluorescence signals is displayed. The moments of highest depolarization of the electrical signal (blue line) coincide with the peaks of fluorescence (orange line), thus supporting the assumption.

However, the phase conversion of the optical and the electrical data, shown in Figure 4.1B, leaves the phase signals temporally spaced. This happens because the optical data is converted so that the phase transition coincides with the fluorescence peaks, while for the electrical data the middle of the depolarization slope matches the phase transition, instead of the final instant of depolarization. Therefore, the resulting phase signals are temporally shifted by approximately 12 ms. This is caused simply by phase mapping timing and does not affect the actual correlation of the signals.

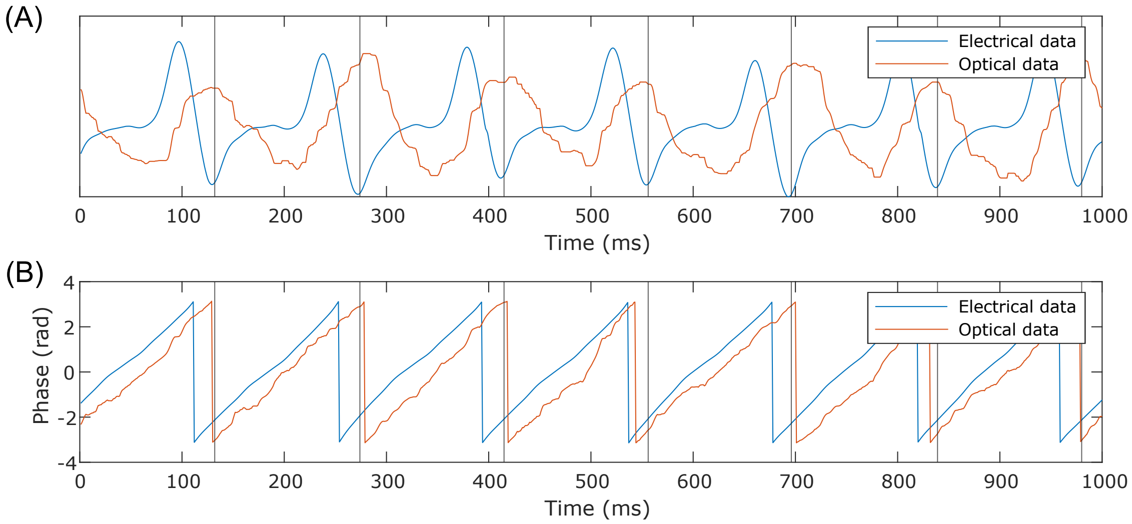

Figure 4.1: Correlation between electrical and optical signals. **(A)** Representative 1-second segments of electrical and fluorescence data, recorded simultaneously. The vertical black lines mark the peaks of depolarization of the electrical signal (blue line). The fluorescence excitation intensity increases when membrane potential decreases, therefore the fluorescence signal (orange line) positive peaks are expected to be synchronized with electrical depolarization, which stands true for the segment presented. Both signals were normalized for comparison. **(B)** Phase data from the signals in (A). For optical data (orange line), the phase cut corresponds to the fluorescence peak and, therefore, with the end of the depolarization in the electrical data. For electrical data (blue line), however, the cut transition occurs in the middle of the depolarization, which explains the slight delay of the optical phase signal in relation to the electrical.

Besides the phase signals, the phase maps were also compared for optical and electrical data. Figure 4.2 shows the phase maps at five different time points, with the optical data temporally shifted forward by 12 ms. For the electrical data, the 8x8 pixels matrices correspond to the original electrical recordings and the 38x47 pixels matrices are the result of interpolation of the original data, so that the maps are comparable with the optical maps. For the optical data, the 38x47 pixels correspond to the area where the electrodes' array is present in the full-sized optical maps, while the 8x8 pixels matrices are downsampled optical maps. As shown in the figure, there is a high correlation between optical and electrical data.

From this analysis, it was concluded that the correlation between electrical and optical data was clean and, consequently, the generalization of results was viable.

4.2 Does methodology affect rotor correlation?

The processing of the data and the algorithm to find correlations between PSs from different resolutions possess multiple variables that may impact the results. The study and optimization of these parameters are important for the reproducibility and reliability

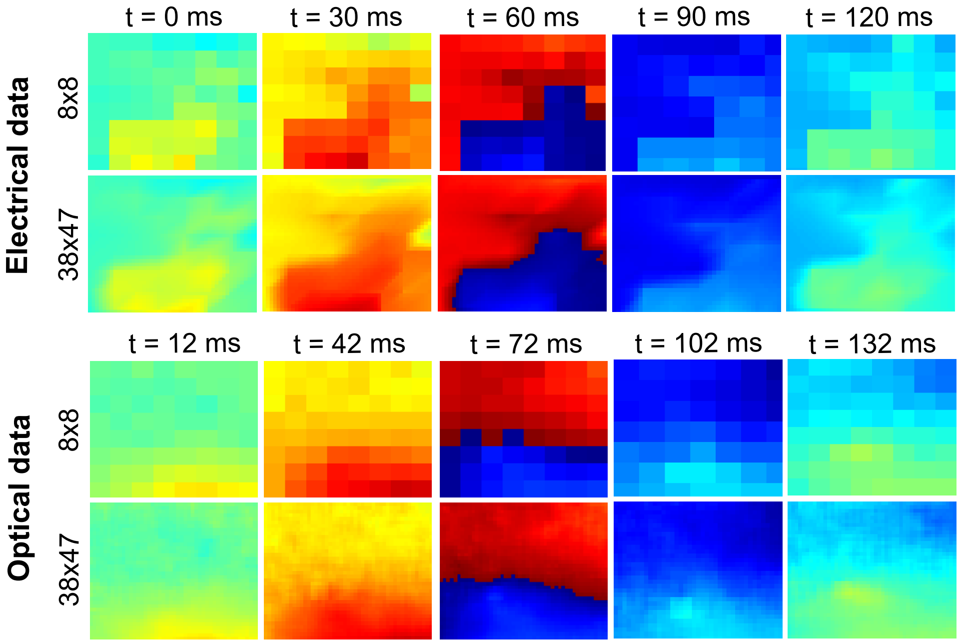

Figure 4.2: Correlation between electrical and optical phase maps.

of the results. In order to recognize and evaluate the effects of the methodology itself, in particular the data decimation and the correlation process, the following questions were raised, which are explored in this section.

1. How does the **downsampling method** affect the F1-score?
2. How does the **upsampling method** affect the F1-score?
3. How does the F1-score change depending on how **spatially accurate** the correlation is demanded to be?
4. Does the stable rotor's **lifespan restriction** hide relevant PSs?

For these analyses, only the epicardium data was considered.

4.2.1 Downsampling grid position

When downsampling, only a portion of the recorded signals are used for the posterior analysis. The signals selected were spaced in a uniform grid and a fixed position for the grid was maintained throughout the study. However, the generalization of the results for each sub-resolution based on the information from a single data subset may be unrealistic. In order to assess the uncertainty added by the grid position, four different grid positions were tested for three sub-resolutions ($\mathbb{D} = \{2, 5, 10\}$). In Figure 4.3, grid position 1 corresponds to the default placement and grid positions 2, 3, and 4 are the variations tested. The F1-score was obtained for each grid position, and the variation between the resulting values was computed for each recording.

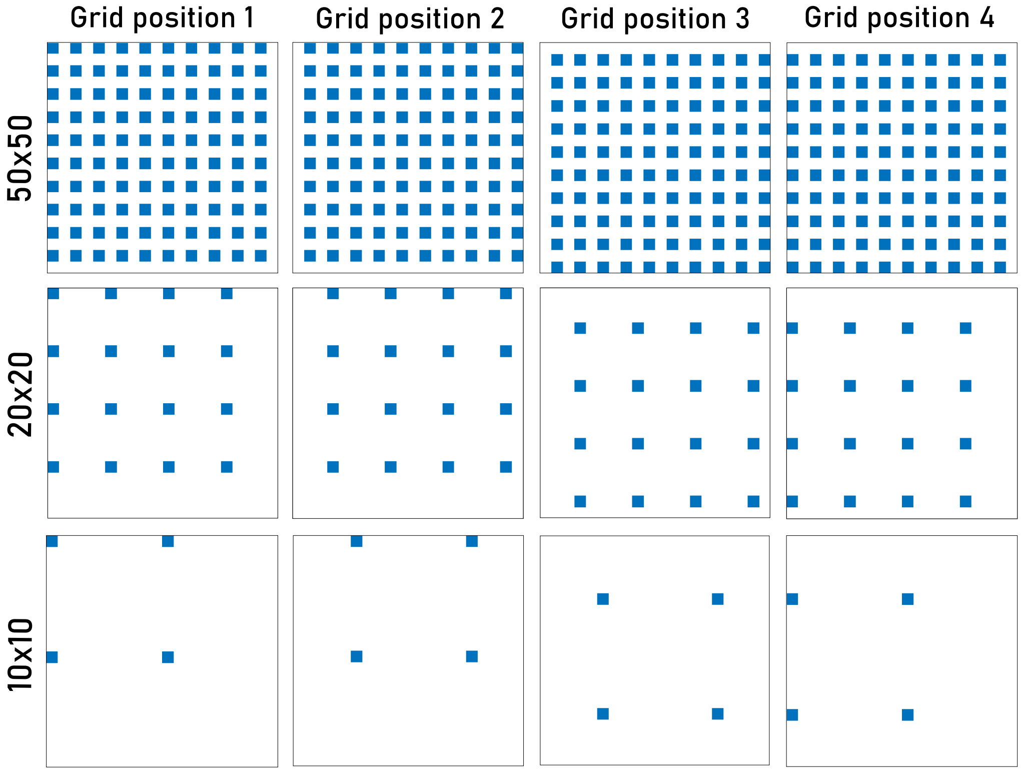

Figure 4.3: Representative matrices of the downsampling grid positions tested for half, a fifth, and a tenth of the original resolution.

Figure 4.4 showcases the F1-score variation due to the position of the pixels selected for sampling, shown as mean and standard deviation. Some variation was observed for all sub-resolutions. For the highest sub-resolution, the mean variation is close to 0.1, while it is closer to 0.2 for the other two sub-resolutions. These values represent variations of 10 to 20% of the F1-score, which means that the position of the electrodes is an important factor that might influence rotor mapping results.

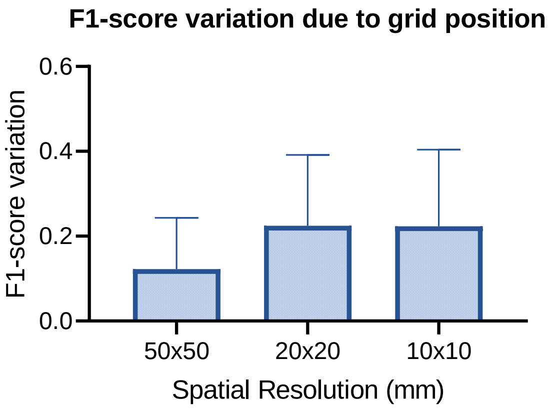

Figure 4.4: F1-score variation induced by the position of the downsampling grid (N=11). Values presented as mean ± standard deviation.

4.2.2 Interpolation method

After downsampling comes the upsampling, and this step has a source of variation as well. Upsampling requires interpolation and there are several methods to do it that may provide different results. The F1-scores obtained using linear, cubic, and cubic spline interpolation are compared in Figure 4.5, for five sub-resolutions.

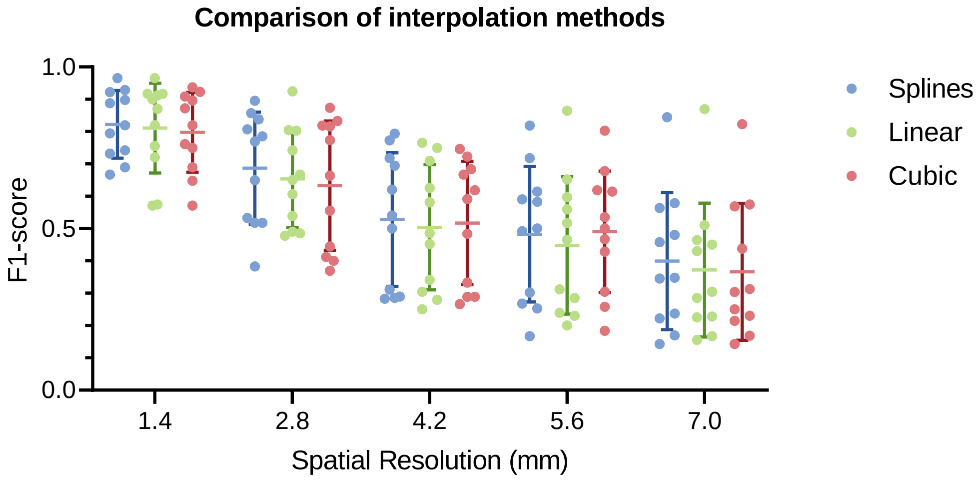

Figure 4.5: F1-score for different interpolation methods (N=11). Data presented as mean±SD.

Visually, there does not seem to be a considerable difference in values for the various interpolation methods, and a repeated measures two-way ANOVA test confirmed that the variation was not statistically significant (p value = 0.1712). Thus, the choice of interpolation method does not impact significantly the results, for the methods tested.

4.2.3 Spatial accuracy threshold

During the correlation between the PSs found in the original maps and the ones found for lower resolutions, a restriction is set regarding how close the PSs in sub-resolution maps have to be to the original location. In order to analyze how PS detection is affected by this displacement restriction, a F1-score profile was created for each sub-resolution with accepted displacement ranging from 0 to 7 mm. Figure 4.6 displays the obtained curves.

These graphs show that, for every sub-resolution, a plateau is reached. The spatial accuracy threshold at which that plateau is reached depends on the IED. As the IED increases, the spatial accuracy that can be expected decreases. For the highest IED considered, 7.0 mm, the minimum spatial accuracy radius (or displacement threshold) for which all correlating rotors are detected is 3.5 mm. It makes sense for the minimum radius to coincide with half the resolution, since that should be the maximum displacement possible.

The value of 3.5 mm (5 pixels) was then selected as the default displacement threshold for the remainder of the study, since it ensures that the F1-score values correspond to the best-case scenario for every resolution while being an acceptable error for ablation therapy.

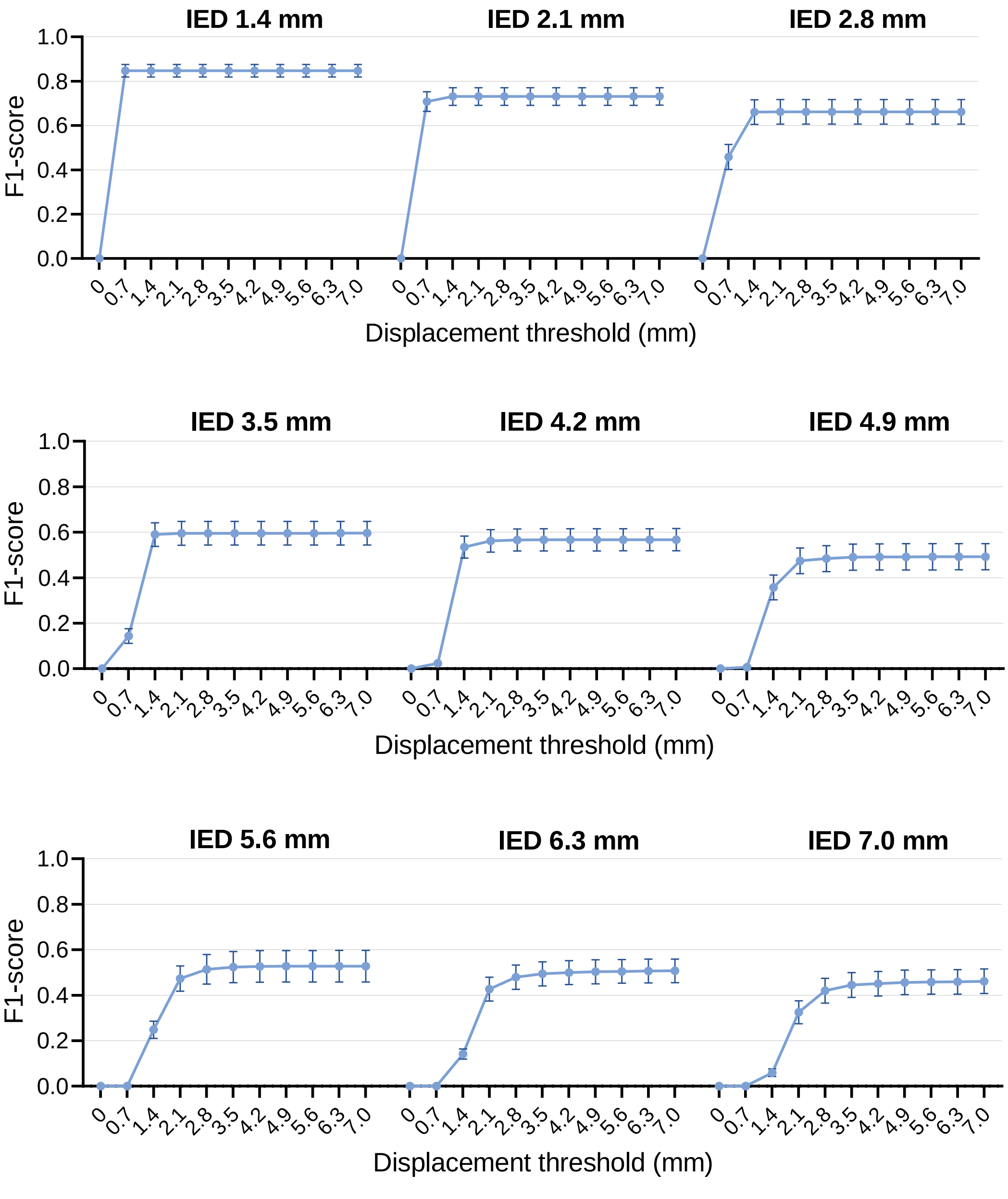

Figure 4.6: F1-score profile for changing spatial displacement threshold in phase singularity (PS) correlation, for all sub-resolutions (N = 11). Data presented as mean±SEM.

4.2.4 Lifespan restriction

When tracking rotors, the minimum lifespan accepted for a phase singularity to be considered as such is defined. Yet another lifespan threshold is set to distinguish stable rotors from non-stable ones, defined by the minimum CL of each recording. When studying detection accuracy through its F1-score, only stable rotors are considered. While this is a necessary restriction since the objective is to analyze the most meaningful rotors, it has its downfalls. This constraint leads to the assumption that missing rotors are not present in sub-resolution maps, which is not necessarily the case. As soon as a PS's duration falls behind the minimum CL it is ignored, which might happen for PSs that are broken into several segments that do not last the required period individually. However, when observing the phase maps through time, the PS might be clearly present in the sub-resolution for the majority of the time. With this in mind, the number of true rotors found for lower resolutions was investigated for different lifespan restrictions of sub-resolution stable rotors. These varying lifespan thresholds were only applied for sub-resolutions, while for the original resolution the restriction was kept at minimum CL, so that the comparison was made with the stable rotors present in the original resolution. Figure 4.7 shows the percentage of true rotors found for three different lifespan restrictions: half the minimum CL, three quarters of the minimum CL, and the minimum CL as used before.

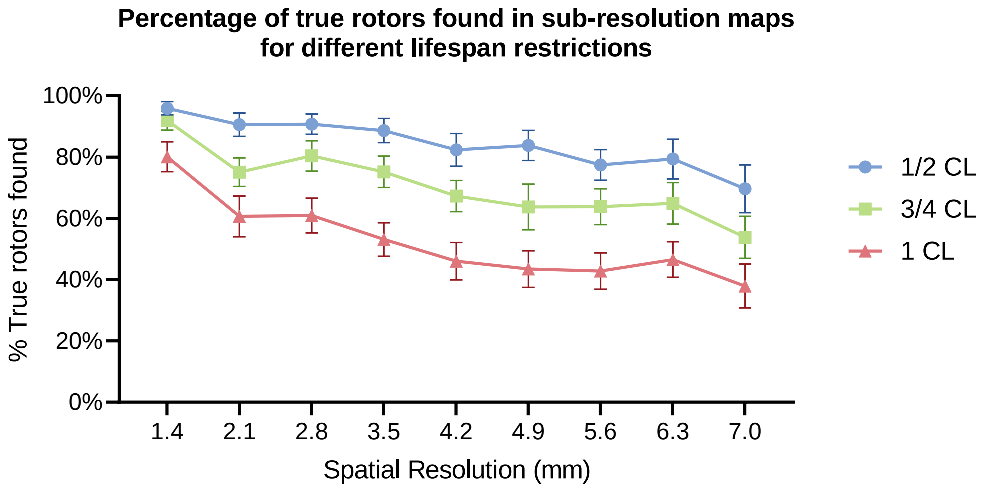

Figure 4.7: Percentage of true rotors found in sub-resolutions for different lifespan restrictions on sub-resolution rotors (N=11). Values presented as mean±SEM. CL, cycle length.

The percentage of rotors found is clearly superior for lower CLs, which means that there is a successful correlation between shorter-lasting PSs in sub-resolution maps and the stable rotors from the original resolution. Thus, it can be concluded that the rotors considered missing may be, in fact, present, but are not lasting the same amount of time and therefore are not being accounted as potential stable rotors. The reasoning for the establishment of the stable rotor's lifespan restriction does not lose integrity, as the rotors will lose meaningfulness if their lifespan decays. Thus, in terms of PS relevance, it is valid to consider these rotors as missing, but this finding justifies the presence of the rotors on the sub-resolution instantaneous phase maps when they are deemed missing. The loss in spatial resolution leads to the fragmentation of the phase singularity's path, and consequently to the inability of tracking algorithms to follow them through time.

4.3 How do arrhythmia dynamics change due to loss in spatial resolution?

The first step to reach the goals established for this thesis was to analyze the overall change in arrhythmia dynamics' characteristics and quality of rotor detection and localization due to spatial resolution. The values presented in this section correspond to the means of the recordings of each experiment, from both surfaces of the heart.

4.3.1 Dynamics characteristics

In order to assess if spatial resolution affects the perceived dynamics of an arrhythmia, the first metrics looked at are the ones that provide general information regarding the arrhythmia behavior, which are incidence and duration.

Incidence

PS incidence provides some insight on the level of organization of the arrhythmia since more disorganized rhythms are expected to reveal a higher incidence of PSs. Figure 4.8 presents arrhythmia drivers' incidence per unit area as spatial resolution decreases, and discriminates between the incidence of all phase singularities (APS) and the incidence of stable rotors (SRs). The spatial resolution of 0.7 mm corresponds to the original IED.

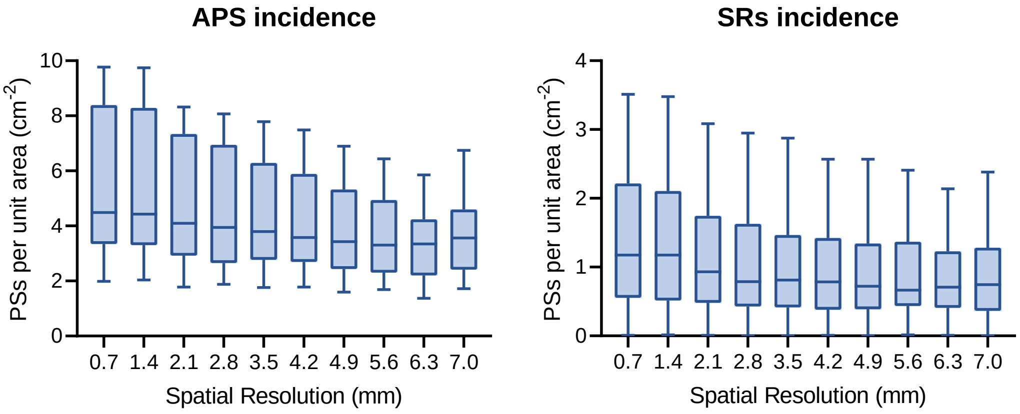

Figure 4.8: All phase singularities (APS) and stable rotors (SRs) incidence for different spatial resolutions, given as the number of rotors detected per square centimeter (N=12).

APS incidence tends to decrease with resolution. This makes sense, as the data quality worsens with lower resolutions, thus making PS tracking more challenging. There seems to be a more significant loss of information for high-incidence recordings, as the slope of the upper quartile is steeper than the median or the lower quartile. For SRs, the tendency is similar, with the incidence decreasing with resolution. However, incidence seems to stabilize for lower resolutions, after a noticeable drop between resolutions 1.4 mm and 2.1 mm. This may indicate that the most stable rotors are consistently detected, even for lower resolution. However, incidence does not assure that the same rotors are being detected for the lower resolutions or if the rotors being found correlate with the original ones, so those conclusions cannot be drawn at this point.

The incidence of both APS and SRs for each sub-resolution was statistically compared with the respective original incidence. The results of this comparison are presented in Table 4.1. The only sub-resolution with a non-significant difference to the original incidence is 1.4 mm, for both APS and SRs. This result is in accordance to what is visually inferred from the graphs.

In conclusion, rotor incidence tends to decrease as spatial resolution is lost. This is in conformity to previous studies [84], and may lead to different interpretations of the arrhythmia dynamics and mechanisms depending on the resolution of the mapping device.

Table 4.1: Results of a Dunnett's multiple comparisons test to assess significant differences in rotor incidence due to spatial resolution. The test compares the mean of each sub-resolution to the control, which is the original resolution's mean rotor incidence. The test was performed for (a) the incidence of all phase singularities, and (b) incidence of stable rotors.

(a) All phase singularities (N=12).

Comparison	Summary	*p* value
0.7 vs. 1.4	ns	0.4007
0.7 vs. 2.1	**	0.0029
0.7 vs. 2.8	**	0.0078
0.7 vs. 3.5	**	0.0091
0.7 vs. 4.2	**	0.0095
0.7 vs. 4.9	**	0.0059
0.7 vs. 5.6	**	0.0090
0.7 vs. 6.3	**	0.0066
0.7 vs. 7.0	**	0.0095

ns, not significant.
** p value ≤ 0.01.

(b) Stable rotors (N=11).

Comparison	Summary	*p* value
0.7 vs. 1.4	ns	0.1424
0.7 vs. 2.1	**	0.0063
0.7 vs. 2.8	**	0.0072
0.7 vs. 3.5	*	0.0136
0.7 vs. 4.2	*	0.0152
0.7 vs. 4.9	*	0.0123
0.7 vs. 5.6	*	0.0221
0.7 vs. 6.3	*	0.0338
0.7 vs. 7.0	*	0.0437

ns, not significant.
* p value ≤ 0.05; ** p value ≤ 0.01.

Duration

The lifespan of the phase singularities is another relevant characteristic of arrhythmia dynamics, as longer-lasting rotors are more stable. Figure 4.9 depicts APS' and SRs' duration as spatial resolution is lost.

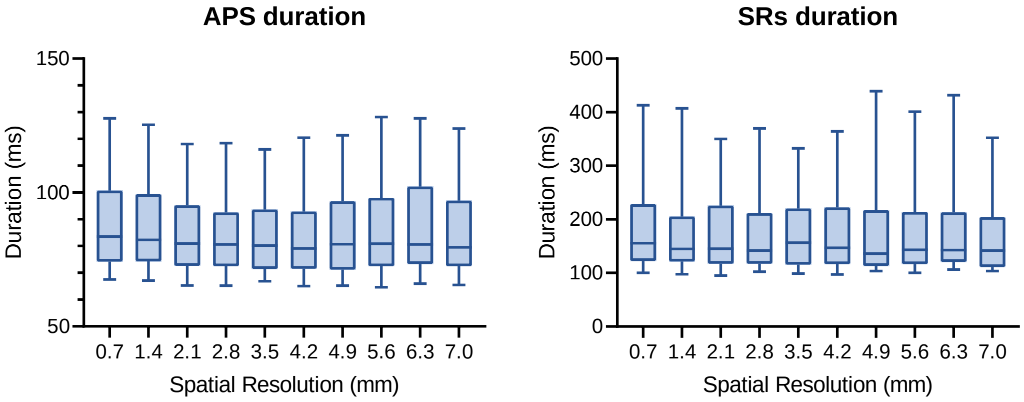

Figure 4.9: Duration of all phase singularities (APS) (left) and stable rotors (SRs) (right) for different spatial resolutions, given in milliseconds (N = 11).

There are slight variations between resolutions, but they are not visually significant for neither APS nor SRs. When analyzing statistically, there are different results for APS and SRs. Table 4.2a shows the results from the comparison between APS duration for sub-resolutions and the original resolution. The difference and its *p* value seem to follow a U-shaped curve, first decreasing with the highest difference for resolutions 2.1, 2.8, and 3.5 mm, and then increasing until the difference is no longer statistically significant (resolutions 6.3 and 7.0 mm). A possible explanation for this behaviour would be the increasing restriction of the rotors to specific locations as spatial resolution is lost and the number of interpolated values increases. If that is the case, the data loss creates the initial decrease in APS' duration, but as the amount of true data continues to deteriorate, the interpolation effect gains impact and forces the detected singularities to discrete locations, which would lead to the subsequent increase in APS duration.

In the case of SRs, the variation in rotor duration does not seem to relate to spatial resolution. The results of the statistical comparisons are presented in Table 4.2b, and there is no real statistically significance, as the only statistically significant difference has a *p* value just below the threshold. Therefore, the results indicate that stable rotors' duration is not affected by spatial resolution.

4.3.2 Detection accuracy

From the previous section, it is known that phase singularities' detection decreases as spatial resolution is lost, since the number of APS and SRs found lowers. Consequently, detection accuracy is bound to decrease for higher IEDs, since rotors will be missing. However, dynamics characteristics do not specify if the PSs present for lower resolutions are indeed the same as the ones in the original resolution. Hence, a question that remains is whether the PSs detected for lower resolutions are in fact the right PSs.

Table 4.2: Results of a Dunnett's multiple comparisons test to assess significant differences in rotor duration due to spatial resolution. The test was performed for (a) the duration of all the phase singularities, and (b) duration of stable rotors, specifically.

(a) All phase singularities (N=12).

Comparison	Summary	*p* value
0.7 vs. 1.4	ns	0.0828
0.7 vs. 2.1	**	0.0037
0.7 vs. 2.8	**	0.0014
0.7 vs. 3.5	**	0.0058
0.7 vs. 4.2	**	0.0015
0.7 vs. 4.9	*	0.0108
0.7 vs. 5.6	*	0.0152
0.7 vs. 6.3	ns	0.9999
0.7 vs. 7.0	ns	0.5609

ns, not significant.
* *p* value ≤ 0.05; ** *p* value ≤ 0.01.

(b) Stable rotors (N=11).

Comparison	Summary	*p* value
0.7 vs. 1.4	ns	0.3554
0.7 vs. 2.1	ns	0.2068
0.7 vs. 2.8	ns	0.0991
0.7 vs. 3.5	ns	0.4005
0.7 vs. 4.2	ns	0.0974
0.7 vs. 4.9	ns	0.9997
0.7 vs. 5.6	*	0.0450
0.7 vs. 6.3	ns	0.9888
0.7 vs. 7.0	ns	0.2585

ns, not significant.
* *p* value ≤ 0.05.

F1-score

To answer that question, the F1-score was computed for each sub-resolution, for every recording. Figure 4.10 shows the mean F1-score as spatial resolution decreases, and it is noticeable that, as expected, the F1-score decreases alongside resolution. This relationship confirms that spatial resolution affects the quality of rotor detection.

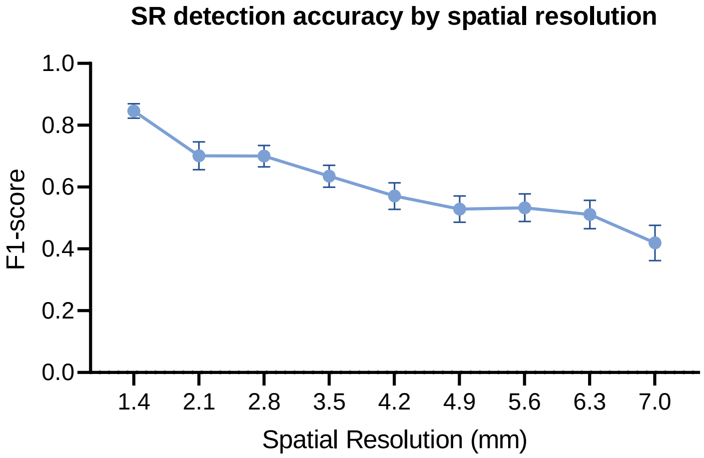

Figure 4.10: Stable rotor (SR) detection accuracy for different spatial resolutions, given by the F1-score of rotor detection and presented as mean±SEM (N = 11).

To get a better sense of the F1-score values to be expected for each resolution, the confidence intervals of the mean were calculated and are displayed in Table 4.3. These intervals allow to understand how overlapped or not the F1-score means are for each resolution, and add to the information given by the mean. Analyzing the F1-score of the highest sub-resolution, the difference between its mean value and the ground truth is considerable, representing a drop of 15% in detection accuracy. For the 2.1 mm resolution, the mean F1-score decreases 15% again. It can be observed that the confidence intervals for these two sub-resolution are not overlapped, establishing a clear accuracy decline. For the rest of the sub-resolutions, there is always overlapping between adjacent confidence intervals. Although for some segments the confidence interval practically does not vary, such as between resolutions 2.1 and 2.8 mm and between resolutions 4.9 and 8.3 mm, the F1-score clearly decreases with resolution.

Table 4.3: F1-score and respective confidence interval for each spatial resolution, for all hearts (N=11). F1-score is presented as mean±SEM.

Resolution (mm)	**F1-score**	**Confidence Interval**
1.4	0.85 ± 0.02	0.80 - 0.90
2.1	0.70 ± 0.04	0.60 - 0.80
2.8	0.70 ± 0.03	0.62 - 0.78
3.5	0.64 ± 0.04	0.56 - 0.71
4.2	0.57 ± 0.04	0.47 - 0.67
4.9	0.53 ± 0.04	0.43 - 0.63
5.6	0.53 ± 0.04	0.43 - 0.63
6.3	0.51 ± 0.05	0.41 - 0.62
7.0	0.42 ± 0.06	0.29 - 0.55

The F1-score provides a single measure that summarizes the accuracy of rotor detection, taking into account both the percentage of missing rotors and the percentage of false rotors. Nevertheless, it is relevant to compare these percentages, to understand which affects the overall accuracy the most. Therefore, recall and precision were analyzed separately and their values are presented in Figure 4.11. It can be observed that the values for recall are lower than for precision, meaning that it is more likely that rotors are being lost for lower resolutions than that false rotors are being generated. This tendency can be explained by the fact that the overall number of rotors detected decreases with resolution and, consequently, it is more probable to detect less true rotors than for extra rotors to appear. Therefore, although loss in resolution does lead to the appearance of phantom rotors, its impact is heavier in the sensitivity to true rotors.

F1-score for increasing PS duration

The F1-score gives a sense of the accuracy of rotor's detection. However, it does not automatically discriminate between rotors. Although the classification as a stable rotor already discards shorter-lived rotors, within the stable rotors not all are equally important. Assuming that longer-lasting SRs are more relevant to the arrhythmia dynamics and of more interest for therapy, it is meaningful to verify whether these SRs in particular are being recognized. With that in mind, the F1-score was computed for varying stable rotor duration thresholds, as shown in Figure 4.12. By increasing the lifespan threshold, the longer-lasting rotors are more and more isolated from the rest. From Figure 4.12 it can

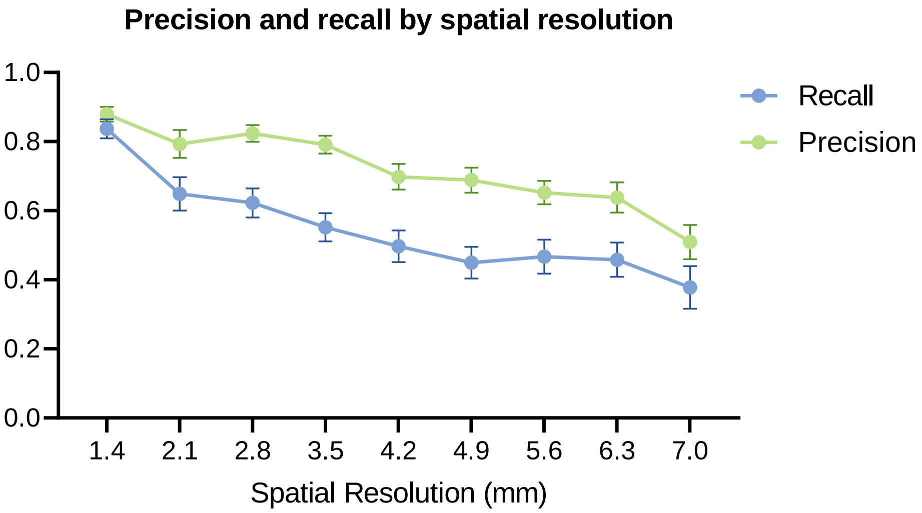

Figure 4.11: Precision and recall for different spatial resolutions, presented as mean±SEM (N=11).

be inferred that the detection of longer-lasting SRs is performed with a similar accuracy as the overall detection up to 2.1 mm of IED. For inter-electrode spacing higher than that, the difference between overall detection and longer-lasting rotors detection becomes more evident. It can be deduced that even if the overall stable rotor detection presents optimistic results, the most meaningful rotors may be lost for spatial resolutions equal or inferior to 2.8 mm. Even if they are being detected, which is possible and likely, they are losing temporal information and not given the adequate weight.

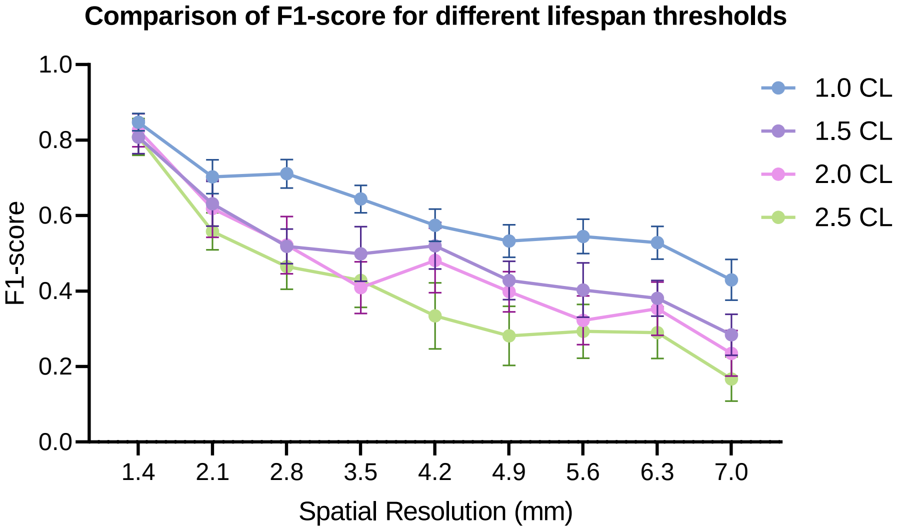

Figure 4.12: Comparison of F1-score for different lifespan thresholds (N=11). F1-score presented as mean±SEM. CL, cycle length.

4.3.3 Localization accuracy

When it comes to focal therapy, not only is it important to detect the rotors, but it is essential to properly locate them for therapy to be successful. In order to evaluate localization accuracy, two metrics were used: displacement between correlated PS paths and the F1-score for PS density maps' peaks.

Displacement

The mean and maximum displacement between successfully correlated PSs from the original resolution and sub-resolutions are presented in Figure 4.13. To be noted that this values are constrained by the acceptable displacement parameter set for the correlation algorithm (Section 3.4.1), which was 5 pixels (3.5 mm) as default. However, as shown before, the acceptable displacement value was chosen because the selected radius englobled most PSs and bigger radii provided similar results. Therefore, the displacements measured and displayed in this section would not vary significantly if the limit displacement was increased.

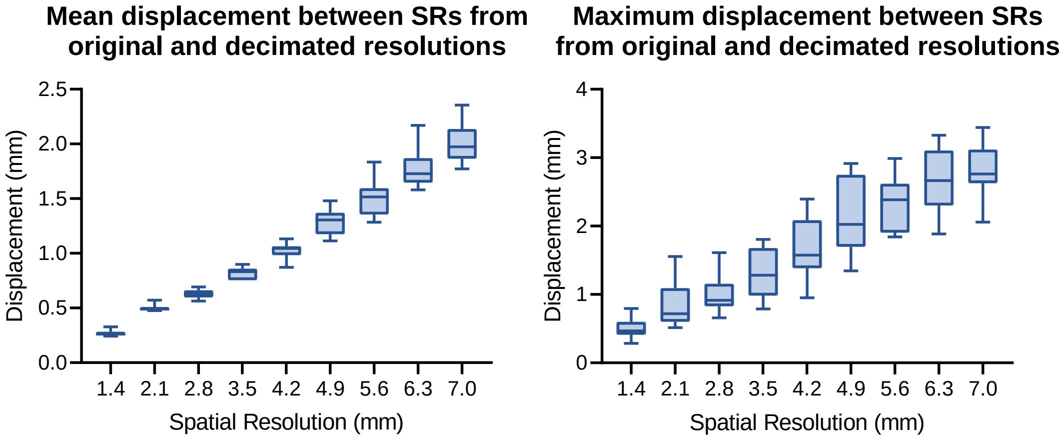

Figure 4.13: Mean and maximum displacement between successfully correlated rotors, for different spatial resolutions (N=11).

As expected, the mean displacement increases linearly with IED. Its value never reaches above 2.5 mm, even for the highest inter-electrode spacing. The mean displacements reached seem to approximately match with a fourth of the respective spatial resolution. This is understandable, since the maximum displacement possible for each resolution should correspond to half the resolution. The actual maximum displacement means seem to average just below the half resolution point for each sub-resolution. For a resolution of 1.4 mm, maximum displacement means are contained to a small range, however, for higher IEDs, the range of maximum displacement means increases and becomes less predictable.

Density maps

Density maps do not analyze PSs individually, but instead provide a global picture of their spatial distribution. This is particularly helpful to verify if the correct location is being selected for therapy, even if the true rotors are not consistently being tracked. This might happen because rotors tend to cluster in regions, and those regions might still be identifiable even when individual PSs are not. To illustrate, the SR density map of one of the VF recordings is displayed in Figure 4.14, along with the density maps of each sub-resolution. At least one peak stands out at the center of the field of view in the original resolution. As spatial resolution is lost, the peak is still detected close to the original position for most sub-resolutions. However, for resolutions equal or inferior to 2.8 mm other peaks appear that seem to have a higher or similar rotor density than the highest peak in the original resolution. It can also be noted that the position of the PSs becomes more discrete as resolution is lost. This is an effect of interpolation [81]. To quantitatively analyze the effect of spatial resolution on the PS density peaks, the F1-score for peak detection in sub-resolution maps was computed. The results are displayed in Figure 4.15.

Just as for rotor detection, the F1-score for rotor localization decreases with loss in spatial resolution. No statistically significant difference was detected between APS and SRs, but it can be observed in the figure that F1-score values for SRs are consistently lower than for APS. Since the number of SRs is lower and their individual impact on the density maps is higher (since they are the longer-lasting rotors), the loss of rotors due to spatial resolution has a higher impact on SRs density maps than for APS density. The F1-score values and respective CI are presented in Table 4.4.

The lifespan of SRs is superior to that of an average PS, so individual SRs are better represented in a density map than shorter-lived PSs. However, the number of rotors that do not last enough to be considered a SR is superior to the number of SRs, since APS incidence is more than double the SR incidence. This raises the question of whether SRs' locations, which are the most important from a clinical perspective, are well identified in density maps that include all rotors or if they are overshadowed by less meaningful rotors. To verify this, the peaks in a APS density map were compared to those found in a SR density map. This comparison was only done for full-resolution maps. The SR peaks were considered to be present in the APS maps if it existed within a radius of 3.5 mm. The mean percentage of missed SR density peaks in APS density maps for each donor heart is presented in Figure 4.16. The overall mean is around 30%, with most values below 40%. Looking at these values, one can assume that a significant portion of the most relevant peaks are being lost when considering all rotors. However, when considering where to apply therapy, the most relevant area might not be where the longer-lasting rotors are present, but where there is a higher incidence of rotors in general.

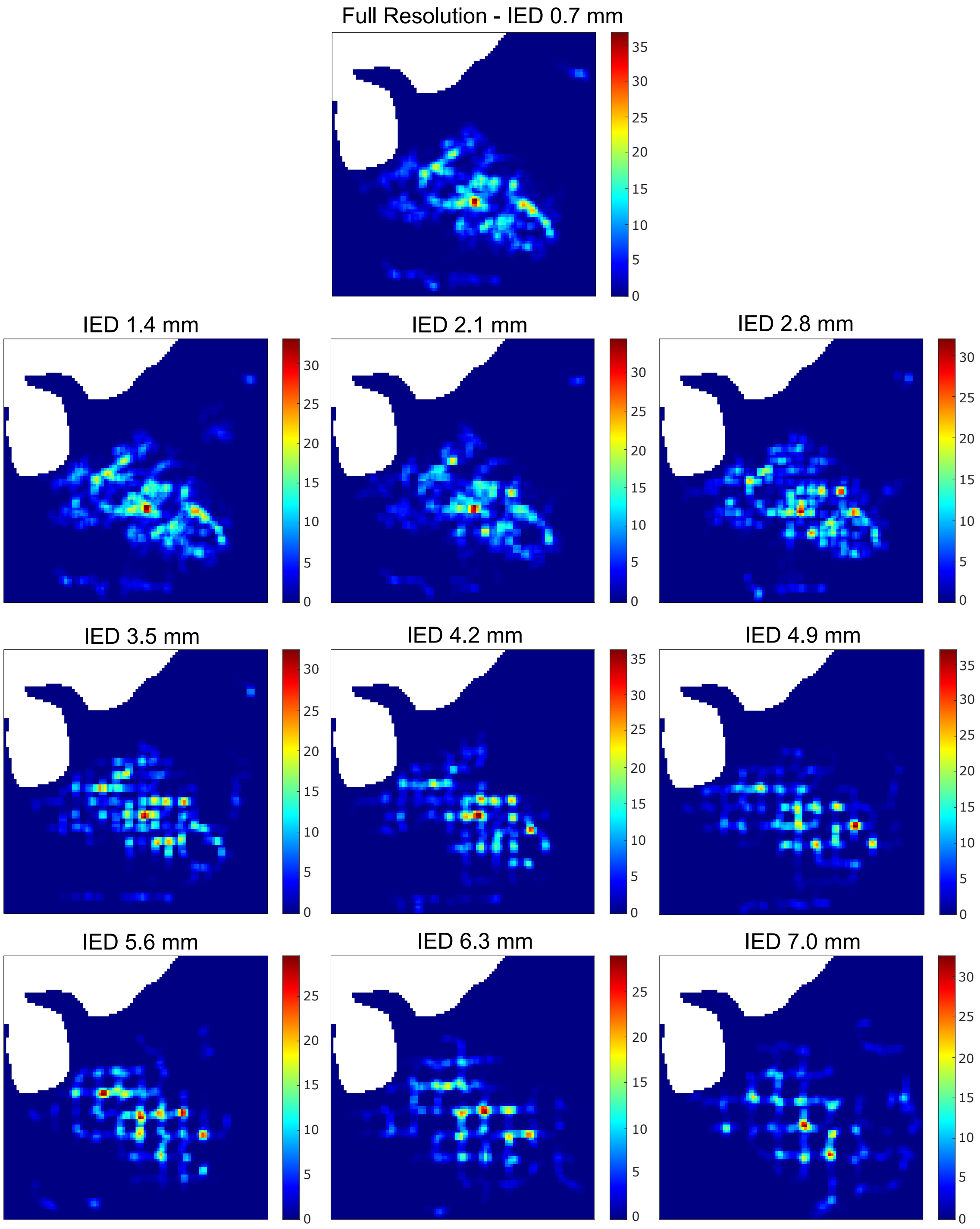

Figure 4.14: Rotor density maps of a single ventricular fibrillation recording for different spatial resolutions. IED, inter-electrode distance.

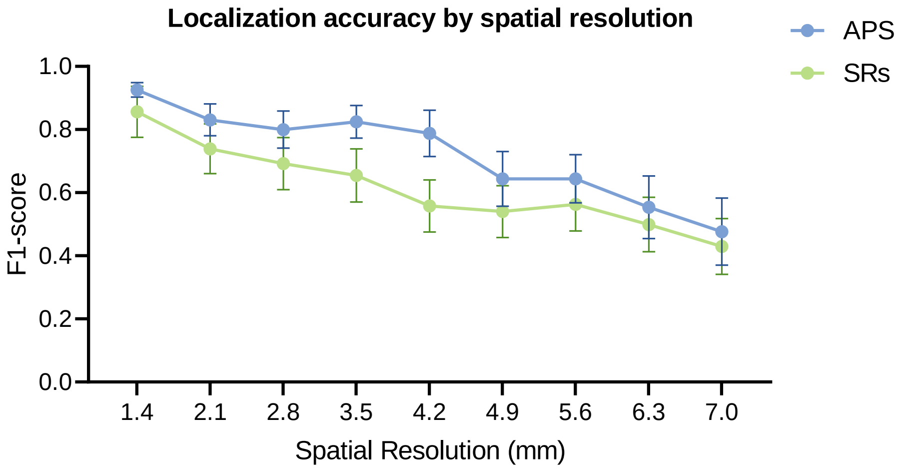

Figure 4.15: Comparison of localization accuracy, given by the F1-score of rotor density peaks, for all phase singularities (APS) and stable rotors (SRs) (N=11). F1-score presented as mean±SEM.

Table 4.4: F1-score of the rotor density peaks detection and respective confidence interval for each spatial resolution, for all hearts. F1-score presented as mean±SEM. IED, inter-electrode distance; CI, confidence interval of the mean.

(a) All phase singularities (N=12).

IED (mm)	F1-score	CI
1.4	0.93 ± 0.02	0.88 - 0.99
2.1	0.84 ± 0.04	0.75 - 0.93
2.8	0.81 ± 0.05	0.71 - 0.91
3.5	0.79 ± 0.04	0.70 - 0.88
4.2	0.73 ± 0.07	0.58 - 0.88
4.9	0.63 ± 0.07	0.47 - 0.80
5.6	0.64 ± 0.08	0.47 - 0.80
6.3	0.56 ± 0.07	0.41 - 0.71
7.0	0.46 ± 0.08	0.28 - 0.63

(b) Stable rotors (N=11).

IED (mm)	F1-score	CI
1.4	0.91 ± 0.03	0.85 - 0.98
2.1	0.80 ± 0.04	0.70 - 0.89
2.8	0.74 ± 0.06	0.62 - 0.86
3.5	0.71 ± 0.06	0.58 - 0.85
4.2	0.61 ± 0.07	0.46 - 0.75
4.9	0.57 ± 0.07	0.41 - 0.72
5.6	0.62 ± 0.07	0.47 - 0.77
6.3	0.52 ± 0.08	0.36 - 0.69
7.0	0.44 ± 0.08	0.26 - 0.62

4.4 How do inherent factors affect perceived dynamics?

Besides methodological variables, there are biological and other inherent factors that may also affect perceived dynamics. The combination of this factors with variation in spatial resolution may have different outcomes. In this section, the data is discriminated by and compared for the following classifications: arrhythmia type (MVT and VF), heart donor sex (female and male), anatomical region (RVOT, MID, and API), and heart surface (endocardium and epicardium).

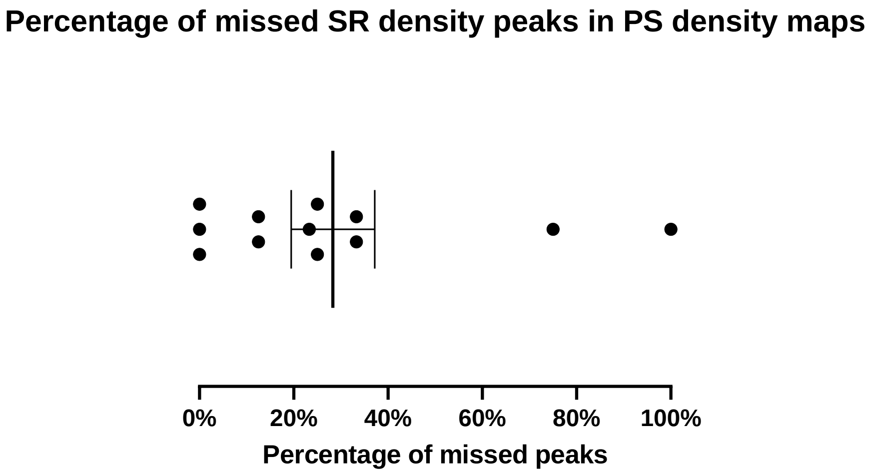

Figure 4.16: Percentage of stable rotors (SRs) density peaks missed in density maps with all phase singularities (APS). Each dot represents the mean for each heart. Vertical line and whiskers represent mean and standard error of the mean (N=12).

4.4.1 Arrhythmia type

One of the objectives of analyzing arrhythmia dynamics is to classify the type and organization of each dysrhythmia. Therefore, different arrhythmia types will have different behaviours. When studying the impact of spatial resolution on perceived arrhythmia dynamics, it becomes pertinent to verify whether different arrhythmia types remain distinguishable as the IED increases. MVT and VF represent the extremities of the spectrum of ventricular tachycardia complexity, so in this section the recordings of each were analysed separately in order to compare their dynamics as spatial resolution is lost.

PS incidence

The first metric compared was PS incidence, for both APS and stable rotors. The arrhythmia type is expected to have an impact on PS incidence, as MVT is a stable tachycardia and expected to have few rotors, while VF is a very disordered rhythm and presumed to be maintained by several PSs. This dichotomy was confirmed by the present data, and is well represented in Figure 4.17.

Even though the difference between APS incidence for MVT and VF is not statistically significant, there is a clear tendency for VF to have a higher number of rotors present. A similar relationship is observed for the incidence of stable rotors, in Figure 4.18.

When it comes to variation due to spatial resolution, both graphs prove what was estimated in Section 4.3.1, that higher-incidence recordings (VF recordings) are more affected by resolution. This is inferred by the clear slope of APS and SR incidence for VF, while incidence stays closer to the ground truth for MVT recordings. This difference in behaviour was also detected statistically, as shown in Tables 4.5 and 4.6. For both tables, the interaction between spatial resolution and arrhythmia type is significant. This means

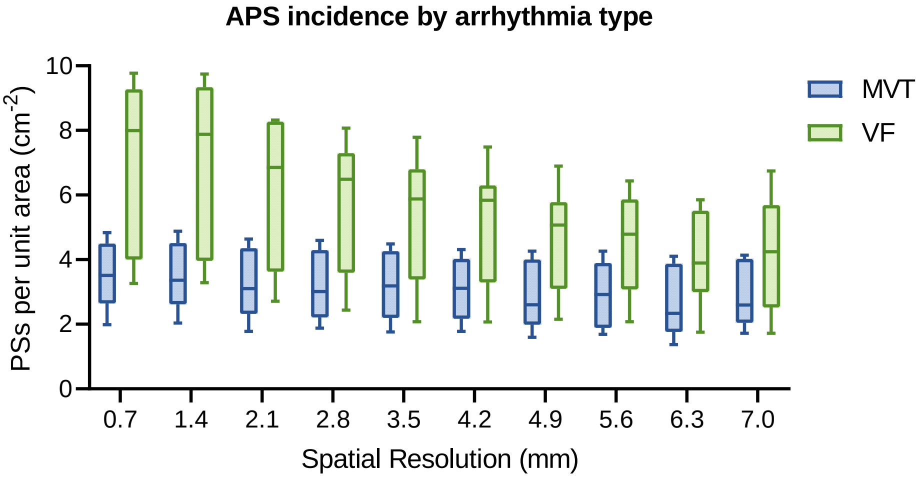

Figure 4.17: Comparison of all phase singularities (APS) incidence for different arrhythmia types (N=12, MVT=5). MVT, monomorphic ventricular tachycardia; VF, ventricular fibrillation.

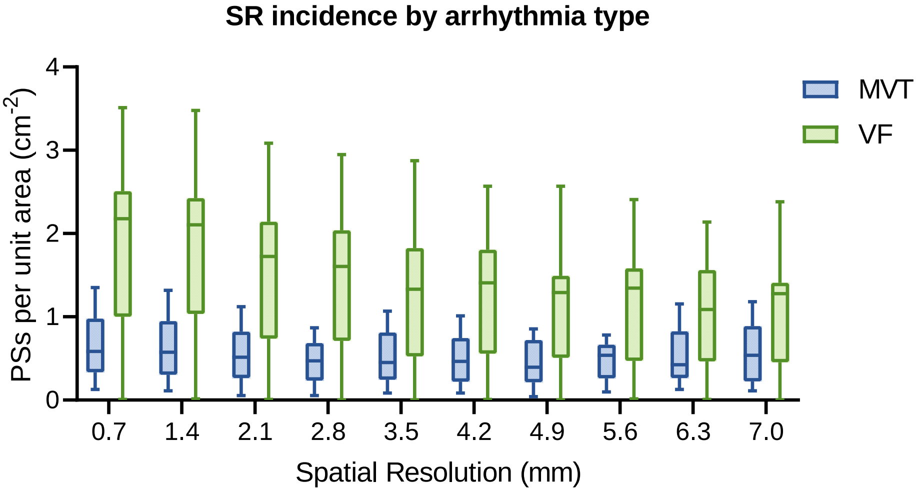

Figure 4.18: Comparison of stable rotor (SR) incidence for different arrhythmia types (N=12, MVT=5). MVT, monomorphic ventricular tachycardia; VF, ventricular fibrillation.

that the mean's difference between spatial resolutions does not evolve in the same manner for MVT and VF.

Table 4.5: Results of a two-way repeated measures ANOVA test to assess the mean differences between all phase singularities incidence for varying spatial resolutions and arrhythmia types (N=12, MVT=5).

Source of Variation	***p* value**	***p* value summary**
Spatial resolution	0.0007	***
Arrhythmia type	0.0662	ns
Spatial resolution x Arrhythmia type	<0.0001	****

ns, not significant.
*** *p* value ≤ 0.001; **** *p* value ≤ 0.0001.

Table 4.6: Results of a two-way repeated measures ANOVA test to assess the mean differences between stable rotor incidence for varying spatial resolutions and arrhythmia types (N=11, MVT=5).

Source of Variation	***p* value**	***p* value summary**
Spatial resolution	0.0054	**
Arrhythmia type	0.0673	ns
Spatial resolution x Arrhythmia type	<0.0001	****

ns, not significant.
** *p* value ≤ 0.01; **** *p* value ≤ 0.0001.

The variation due to spatial resolution in MVT recordings is also different depending on the stability of the rotor. This is seen in the slight decrease in APS incidence, while SRs incidence is less affected. Tables 4.7 and 4.8 shows the results from multiple comparison tests between the incidence for each sub-resolution and the ground truth, for APS and SRs respectively. These results validate the analysis that SR incidence for MVT recordings is more stable than its APS incidence, since the there is no statistical difference between MVT's SR incidence but there is for MVT's APS incidence for lower resolutions. This makes sense, since MVT is characterized by long-lasting stable rotors, which should be harder to lose track of, even for lower resolutions. In the case of VF, with the exception of 1.4 mm IED, all sub-resolutions present a statistically significant lower incidence, for both APS and SRs.

To conclude, the difference between MVT and VF was not statistically significant for any sub-resolution. Therefore, it can be visually inferred that the values of PS and SR incidence for MVT and VF grow closer as spatial resolution is lost, but it cannot be statistically verified.

Duration

The duration of phase singularities is also expected to change depending on arrhythmia type, which is observed for APS in Figure 4.19, and for stable rotors in Figure 4.20.

Table 4.7: Results of a Dunnett's multiple comparisons test to compare phase singularity incidence mean differences between sub-resolution values and the ground truth, for (a) monomorphic ventricular tachycardia (MVT) recordings, and (b) ventricular fibrillation (VF) recordings.

(a) MVT (N=5).

Comparison	**Summary**	***p* value**
0.7 vs. 1.4	ns	0.9565
0.7 vs. 2.1	ns	0.2117
0.7 vs. 2.8	ns	0.3299
0.7 vs. 3.5	ns	0.2911
0.7 vs. 4.2	ns	0.1289
0.7 vs. 4.9	*	0.0394
0.7 vs. 5.6	ns	0.1228
0.7 vs. 6.3	*	0.0156
0.7 vs. 7.0	ns	0.0629

ns, not significant.
* *p* value ≤ 0.05.

(b) VF (N=7).

Comparison	**Summary**	***p* value**
0.7 vs. 1.4	ns	0.4901
0.7 vs. 2.1	**	0.0038
0.7 vs. 2.8	*	0.0126
0.7 vs. 3.5	**	0.0069
0.7 vs. 4.2	*	0.0136
0.7 vs. 4.9	*	0.0118
0.7 vs. 5.6	*	0.0165
0.7 vs. 6.3	*	0.0159
0.7 vs. 7.0	*	0.0124

ns, not significant.
* *p* value ≤ 0.05; ** *p* value ≤ 0.01.

Table 4.8: Results of a Dunnett's multiple comparisons test to compare stable rotor incidence mean differences between sub-resolution values and the ground truth, for (a) monomorphic ventricular tachycardia (MVT) recordings, and (b) ventricular fibrillation (VF) recordings.

(a) MVT (N=5).

Comparison	**Summary**	***p* value**
0.7 vs. 1.4	ns	0.0714
0.7 vs. 2.1	ns	0.1450
0.7 vs. 2.8	ns	0.2858
0.7 vs. 3.5	ns	0.1555
0.7 vs. 4.2	ns	0.1541
0.7 vs. 4.9	ns	0.3007
0.7 vs. 5.6	ns	0.5912
0.7 vs. 6.3	ns	0.1035
0.7 vs. 7.0	ns	0.5386

ns, not significant.

(b) VF (N=6).

Comparison	**Summary**	***p* value**
0.7 vs. 1.4	ns	0.5317
0.7 vs. 2.1	*	0.0204
0.7 vs. 2.8	*	0.0382
0.7 vs. 3.5	*	0.0237
0.7 vs. 4.2	*	0.0374
0.7 vs. 4.9	*	0.0259
0.7 vs. 5.6	*	0.0317
0.7 vs. 6.3	*	0.0350
0.7 vs. 7.0	*	0.0353

ns, not significant.
* *p* value ≤ 0.05.

Visually, it can be noticed that MVT rotors tend to last longer than VF rotors, and this relation is present for APS and SRs. However, the different in duration becomes more obvious for stable rotors. This difference is validated statistically (*p* value = 0.0286), while for APS it was not. Additionally, the difference in duration for MVT and VF rotors stays approximately the same for every spatial resolution. Therefore, the difference between MVT and VF duration is significant, but none of them is affected by spatial resolution considerably. Nevertheless, MVT' APS duration presents the behaviour seen for overall duration in the previous section, with an initial decrease in duration and an increase for lower resolutions.

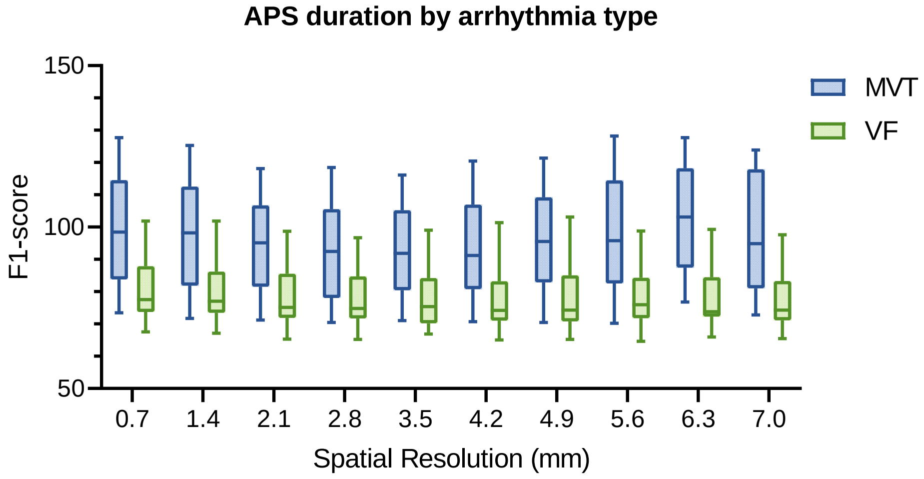

Figure 4.19: Comparison of all phase singularities (APS) duration for different arrhythmia types (N=11, MVT=5). MVT, monomorphic ventricular tachycardia; VF, ventricular fibrillation.

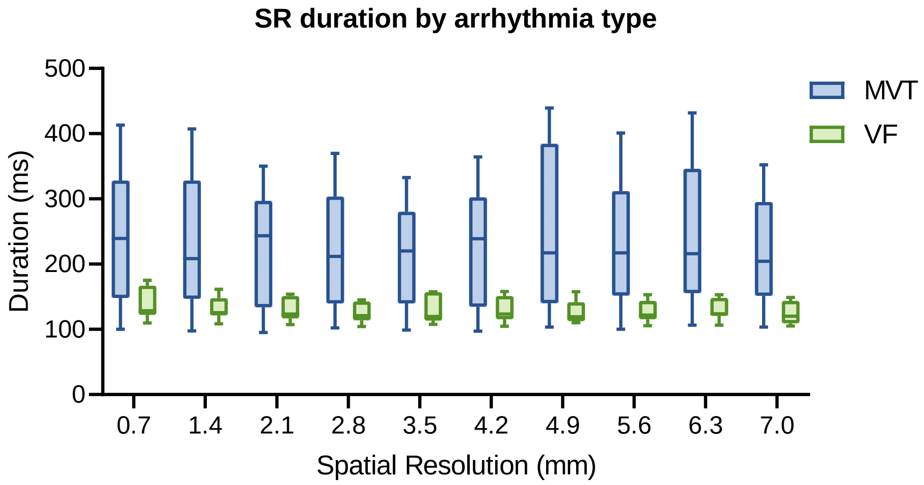

Figure 4.20: Comparison of stable rotors (SRs) duration for different arrhythmia types (N=11, MVT=5). MVT, monomorphic ventricular tachycardia; VF, ventricular fibrillation.

Detection accuracy

The difference between F1-scores for MVT and VF is displayed in Figure 4.21. The difference due to arrhythmia type is not statistically significant, but the difference in their behaviour as spatial resolution is lost is significant. These results are presented in Table 4.9. As seen in Figure 4.21, the F1-score for VF recordings has a much more stable trend downwards, while MVT's F1-score appears to be less dependant on spatial resolution. Furthermore, detection accuracy for MVT is lower than VF for higher resolutions but surpasses it at lower resolutions. This discrepancy can be explained by the difference in rotor incidence for both arrhythmia types, observed before in Figures 4.17 and 4.18. Since the number of rotors present in the recordings is much smaller for MVT, the loss of a few phase singularities is much harsher on the F1-score of MVT recordings than for VF, which results in a more unpredictable trend for the detection accuracy of stable arrhythmias across IEDs. Nevertheless, the F1-score for MVT recordings seems to stabilize at higher accuracy values, while the F1-score for VF keeps decreasing.

Table 4.9: Results of a two-way repeated measures ANOVA test to assess the mean differences between F1-scores for varying spatial resolutions and arrhythmia types (N=11, MVT=5).

Source of Variation	**P value**	**P value summary**
Spatial resolution	<0.0001	****
Arrhythmia type	0.8769	ns
Spatial resolution x Arrhythmia type	0.0011	**

ns, not significant.
** *p* value ≤ 0.01; **** *p* value ≤ 0.0001.

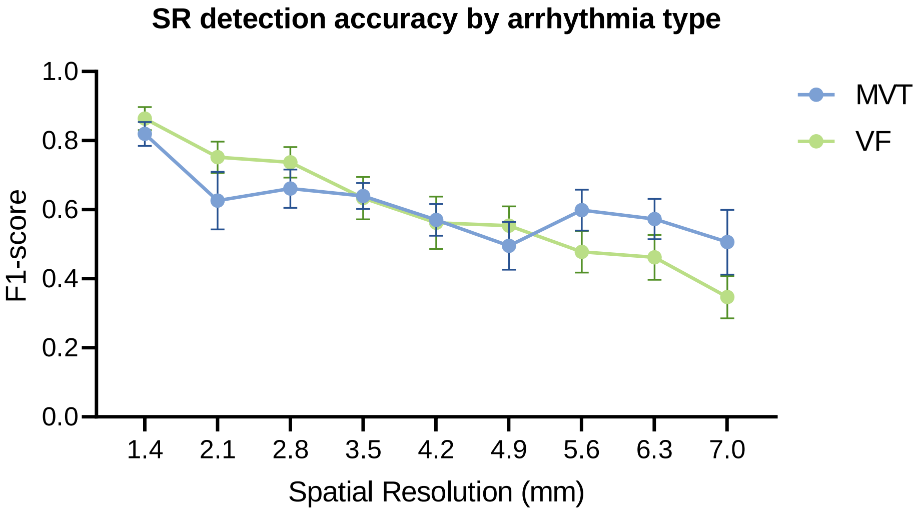

Figure 4.21: Comparison of stable rotor (SR) detection accuracy for different arrhythmia types, given by the F1-score of rotor detection (N=11, MVT=5). F1-score is presented as mean ± SEM. MVT, monomorphic ventricular tachycardia; VF, ventricular fibrillation.

Localization accuracy

Localization accuracy was also compared for MVT and VF. Figure 4.22 shows the F1-score of rotor density peaks. From the graph, it can be taken that localization accuracy stays similar for MVT and VF recordings until a spatial resolution of 2.8 mm, after which VF peak detection accuracy drops in relation to MVT. This is to be expected, since MVT will have rotors more concentrated in certain regions, while VF has more rotors that are shorter and will therefore be more dispersed, making the peak distribution more volatile.

Statistically, the difference was not significant.

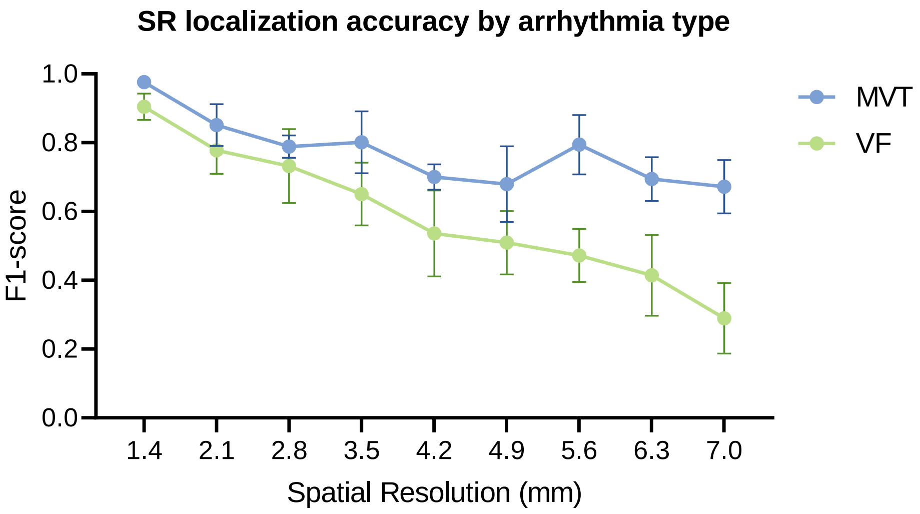

Figure 4.22: Comparison of stable rotor (SR) localization accuracy for different arrhythmia types, given by the F1-score of rotor density peaks detection and for a spatial accuracy radius of 3.5 mm (N=11, MVT=5). F1-score is presented as mean±SEM. MVT, monomorphic ventricular tachycardia; VF, ventricular fibrillation.

4.4.2 Sex

Sex hormones affect cardiac electrophysiology [108]. Therefore, it is useful to analyze sex differences in arrhythmia dynamics and verify how they may change due to spatial resolution of mapping devices.

Incidence

Regarding APS and SRs incidences, no visual or statistical difference was detected for female and male donors. The figures illustrating APS and SRs incidence for different sexes are in Appendix B (Figures B.1 and B.2, respectively).

Duration

As happened for rotor incidence, no significant visual or statistical differences were found in rotor duration between sexes, neither for APS or SRs. The figures illustrating the comparison of rotor duration by sex, for APS and SRs, are in Appendix B (Figures B.3 and B.4, respectively).

Detection accuracy

For detection accuracy, the F1-scores were compared and are displayed in Figure 4.23. Statistically, no significant differences were found. Visually, the F1-score curves match very well, with the F1-score mean for female hearts consistently slightly lower than for males. Although this difference is very faint, it is in accordance with the findings of

Tilz et al., who found a statistically significant difference in ablation outcomes using FIRM mapping for males and females, with females having a higher rate of arrhythmia recurrence [109]. Further studies would have to be made to assess this possible difference.

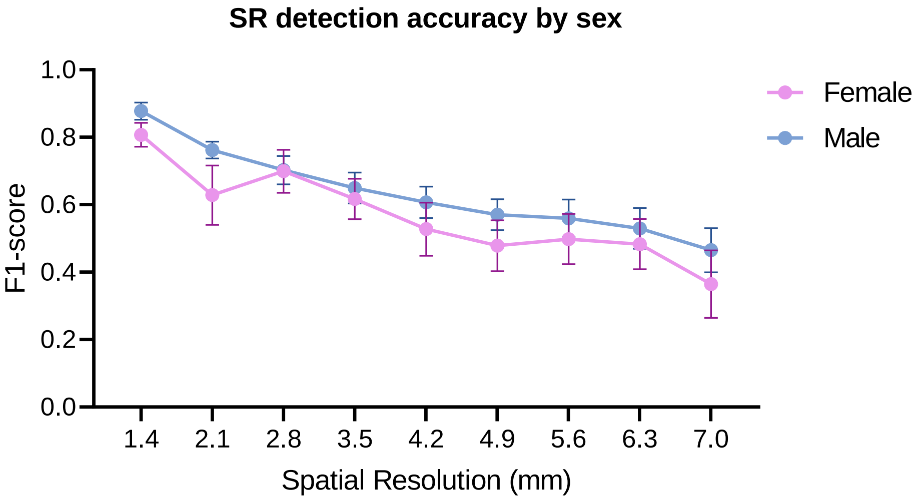

Figure 4.23: Comparison of stable rotor (SR) detection accuracy for different sexes, given by the F1-score of rotor detection (N=11, female=5). F1-score presented as mean±SEM.

Localization accuracy

For localization accuracy, no statistical significance how found. However, the same tendency was observed, with accuracy being consistently lower for females, as shown in Figure 4.24.

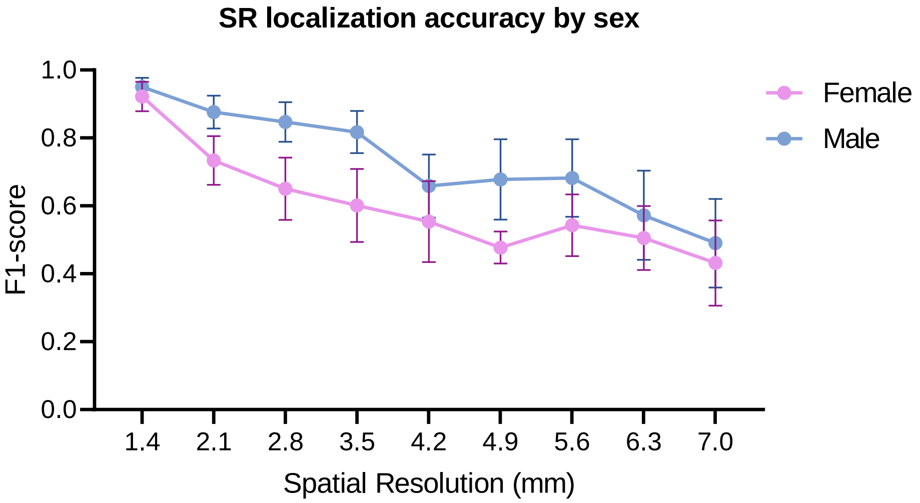

Figure 4.24: Comparison of stable rotor (SR) localization accuracy for different sexes, given by the F1-score of rotor density peak detection (N=11, female=5). F1-score presented as mean±SEM.

4.4.3 Anatomical region

Anatomical factors may affect considerably arrhythmogenesis due to variation in the tissue substrate. As a result, regional analyses are commonly made when studying arrhythmia. Additionally, a regional analysis is of interest for this thesis to verify is there is a specific region that would require a higher electrode density when mapping. For that goal, the field of view was divided in three parts that correspond to the RVOT, the mid-ventricular region, and the ventricular apex. The RVOT is of particular interest, as it is a known arrhythmogenic region, so a higher rotor incidence would be expected in this area [110], [111].

Incidence

Conversely, what the data showed was that incidence was similar for all regions, with a slight tendency for higher incidence in the MID region. This was observed for both APS and SRs incidence. SRs incidence for the different regions is presented in Figure 4.25. A possible explanation is a level of bias due to the MID region coinciding with the middle of the field of view. To minimize bias to certain regions due to differences in the area mapped, incidence is given per unit area and takes into account the area of the data mask in each region. However, the center of the field of view will tend to have better optical data quality, since it is the section in better focus. APS incidence behaved very similarly to SRs and its figure is shown in Appendix B (Figure B.5).

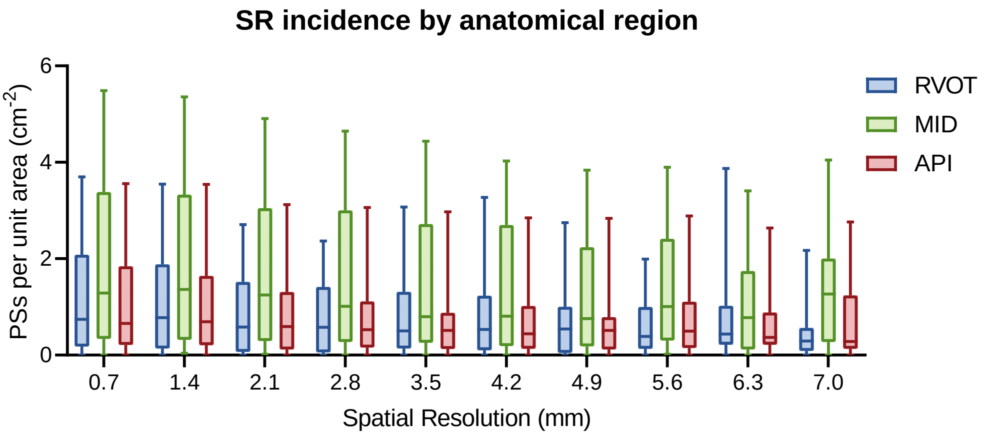

Figure 4.25: Comparison of stable rotor (SR) incidence for different anatomical regions (N=11). RVOT, right ventricular outflow tract; MID, mid-ventricular region; API, apical region.

Duration

The analysis of rotor lifespan for the different anatomical regions also showed no significant difference among them, for neither APS or SRs. The figures illustrating the distribution of mean duration for each heart for APS and SRs are in Appendix B (Figures B.6 and B.7, respectively).

Detection accuracy

Similarly, no statistically significant difference was found between the F1-score curves of each region, presented in Figure 4.26. Although non-significant, rotor detection in the RVOT region appears to tend to be lower than in the other regions.

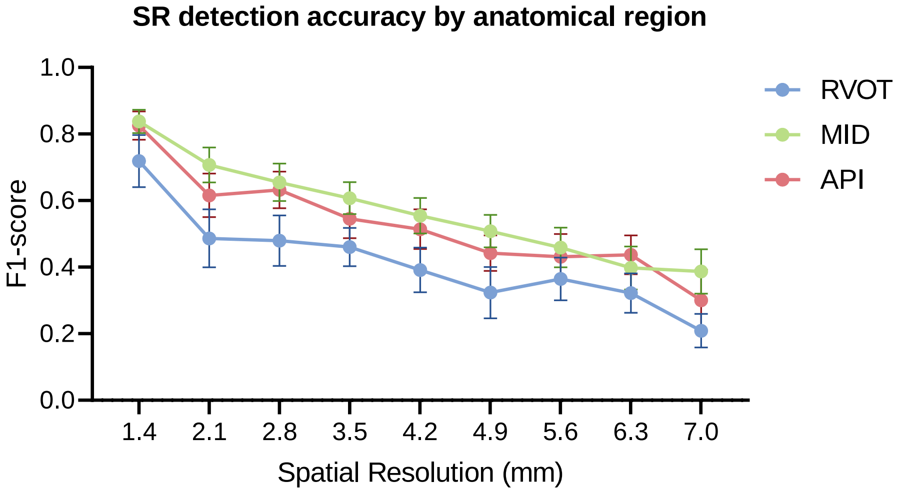

Figure 4.26: Comparison of stable rotor (SR) detection accuracy for different anatomical regions, given by the F1-score of rotor detection (N=11). F1-score is presented as mean±SEM. RVOT, right ventricular outflow tract; MID, mid-ventricular region; API, apical region.

4.4.4 Mapped surface

The majority of the values looked at until now were the mean of the epicardium and the endocardium results for each heart. However, the ventricular wall is thick and rotors gain a three-dimensional configuration, since cardiac propagation travels across the myocardium. Consequently, the arrhythmia dynamics observed in each side of the heart may not be consistent. Rotors can act as a scroll wave and sweep the entire wall simultaneously, or they can be focused in one of the sides of the wall, with their phase singularity only visible in one side. Therefore, arrhythmia dynamics were compared for the epicardium and endocardium.

Incidence

APS incidence for the both heart surfaces is displayed in Figure 4.27. The endocardium appears to have a tendency to present more rotors than the epicardium. A two-way ANOVA test, whose results are presented in Table 4.10, revealed that this difference between layers holds statistical significance (p value = 0.0160). Additionally, the variation due to spatial resolution varied significantly between the epicardium and the endocardium (p value < 0.0001), with the endocardium incidence values dropping more noticeably as resolution is lost.

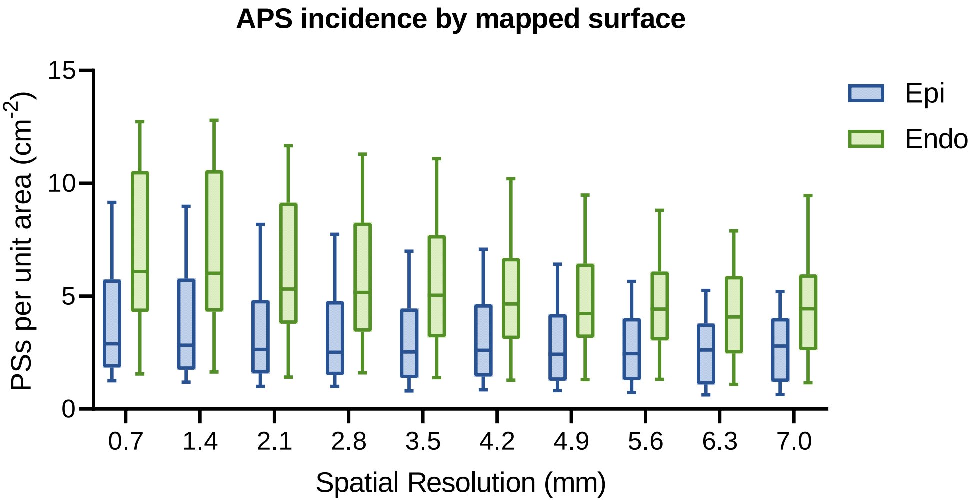

Figure 4.27: Comparison of all phase singularities (APS) incidence in the epicardium (Epi) and the endocardium (Endo) (N=12).

Table 4.10: Results of a two-way repeated measures ANOVA test to assess the mean differences between all phase singularities' incidence for varying spatial resolutions and heart surface (N=12).

Source of Variation	***p* value**	***p* value summary**
Spatial resolution	<0.0001	****
Heart surface	0.0160	*
Spatial resolution x Heart surface	<0.0001	****

* p value ≤ 0.05; **** p value ≤ 0.0001.

For SR incidence, however, the difference due to the heart surface mapped was not statistically significant. SR incidence, shown in Figure 4.28, still tends to be higher in the endocardium side, but the difference is less meaningful. This implies that a considerable portion of the rotors that the endocardium had extra relatively to the epicardium were short-lived.

A likely cause for the difference between rotor incidence is due to the adipose tissue (that is, fat tissue) present in the epicardium, whereas the endocardium allows complete direct access to myocardial tissue.

Duration

When it comes to rotor duration, the differences are not significant, neither due to spatial resolution or mapped surface. This lack of significance was observed for both APS and SRs. The figures illustrating the comparison of rotor duration by mapped surface, for APS and SRs, are in Appendix B (Figures B.8 and B.9, respectively).

Detection accuracy

When comparing the F1-score for rotor tracking, the metric's curves are very similar for

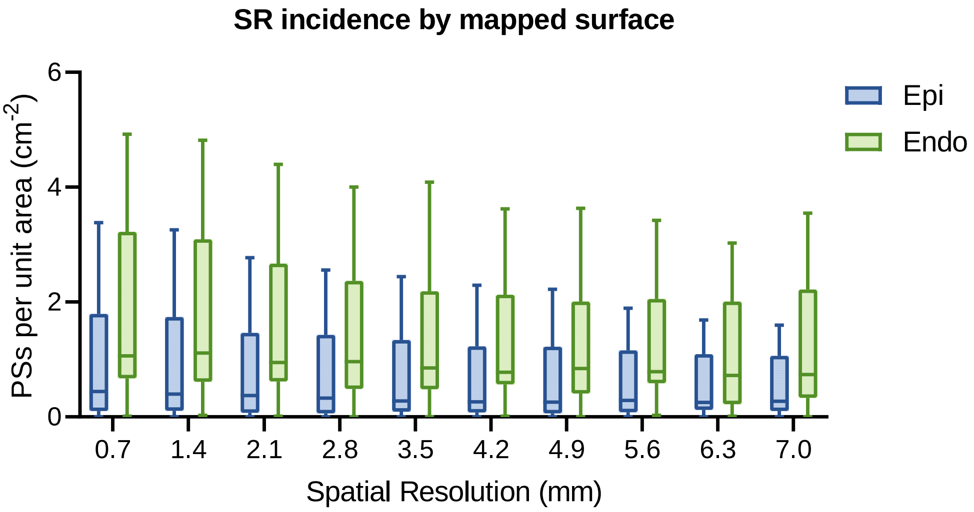

Figure 4.28: Comparison of stable rotor (SR) incidence in the epicardium (Epi) and the endocardium (Endo) (N=11).

endocardial and epicardial tissue, as seen in Figure 4.29. However, even though rotor detection stays similar for the epicardium and the endocardium, mapping the endocardium may provide better results due to the lack of adipose tissue interfering with rotor detection.

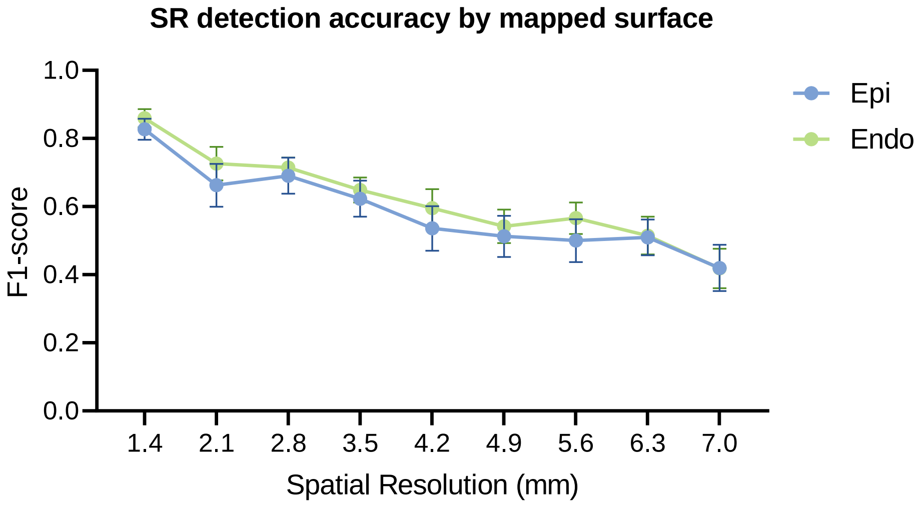

Figure 4.29: Comparison of stable rotor detection accuracy in the epicardium (Epi) and the endocardium (Endo), given by the F1-score of rotor detection (N=11). F1-score is presented as mean±SEM.

Localization accuracy

Localization accuracy was similar for epicardium and endocardium recordings. A graphic representation is provided in Appendix B (Figure B.10).

4.5 What are the spatial resolution requirements to map arrhythmic activity?

When answering the question of what is the ideal spatial resolution for mapping arrhythmia drivers, one has to simultaneously consider how accurate in space the PS detection has to be. Spatial accuracy has repercussions in rotor detection and, consequently, in the spatial resolution needed. For instance, as the desired spatial accuracy becomes more restricted, the detection quality worsens, because rotors that are displaced in the sub-resolution maps are not accounted for if they are outside the accuracy radius range. If the displaced rotor is within the accuracy radius, then the therapy applied to the displaced rotor will reach the rotor's true position. If we consider the case of an ablation intervention, a bigger lesion size means a bigger accuracy radius, which leads to a higher probability of successfully applying therapy to the real rotor when targeting its distorted position. Oppositely, a big ablation lesion will provoke more tissue damage which may eventually lead to the creation of proarrhythmic substrate, which defeats the purpose of the therapy. Therefore, ideal spatial accuracy may take different values depending on the goal of the study or treatment. The acceptable rotor detection accuracy is also user dependant. Thus, the necessary spatial resolution depends on the desired spatial accuracy and detection accuracy.

Throughout this section, both spatial resolution and spatial accuracy radius were taken into account to create accuracy profiles for both detection and localization of arrhythmia drivers.

4.5.1 Detection accuracy

To refresh the concept of the F1-score, this metric is the harmonic mean of precision and recall. Precision corresponds to the percentage of true rotors in the rotors found in a sub-resolution map, while recall corresponds to the percentage of the original rotors that were found. As an example, if precision is 0.5 only 50% of the rotors found correspond to the original ones, and therefore 50% of the rotors found are false rotors. On the other hand, if recall is 0.5 then 50% of the original rotors are missing in the sub-resolution. The harmonic mean of these values would result in a F1-score of 0.5. If both precision and recall are perfect, then the F1-score would be 1. The F1-score drops to 0 whenever no true rotors are found, independently of the amount of false rotors.

In Section 4.2.3, the F1-score was computed for varying spatial accuracy thresholds, with the goal of studying the effect of this parameter on the metric. The results obtained from that analysis are useful to establish the detection accuracy to be expected for when taking into account the spatial resolution of the device and the spatial accuracy necessary. It was also noted in that analysis that for spatial accuracy radii superior to 3.5 mm, the detection accuracy started to reach a plateau. In this section, the highest spatial accuracy radius taken into account is 4.2 mm. This limit was chosen to make sure the plateau is reached for every resolution and because it corresponds to the radius of the more sizeable ablation lesions. Naturally, spatial accuracy directly correlates with spatial resolution, as the maximum spatial accuracy possible for a given resolution will be half the resolution.

Table 4.11 displays the mean F1-scores for all cohort hearts and their standard error. This table provides a general guideline of the rotor detection accuracy to be expected for each spatial resolution and desired spatial accuracy. Figure 4.30 complements it by illustrating the 95% confidence intervals of each F1-score mean.

Table 4.11: Color-coded rotor detection accuracy profile for multiple spatial resolutions and spatial accuracies, based on all recordings (N=11). F1-score values are presented as mean±SEM.

Spatial resolution (mm)	**Spatial accuracy (mm)**						
	0	0.7	1.4	2.1	2.8	3.5	4.2
0.7	1.00 ± 0.00	1.00 ± 0.00	1.00 ± 0.00	1.00 ± 0.00	1.00 ± 0.00	1.00 ± 0.00	1.00 ± 0.00
1.4	0.00 ± 0.00	0.85 ± 0.02	0.85 ± 0.02	0.85 ± 0.02	0.85 ± 0.02	0.85 ± 0.02	0.85 ± 0.02
2.1	0.00 ± 0.00	0.68 ± 0.04	0.70 ± 0.04	0.70 ± 0.05	0.70 ± 0.04	0.70 ± 0.04	0.70 ± 0.04
2.8	0.00 ± 0.00	0.49 ± 0.04	0.70 ± 0.03	0.70 ± 0.03	0.70 ± 0.03	0.70 ± 0.03	0.70 ± 0.03
3.5	0.00 ± 0.00	0.16 ± 0.02	0.63 ± 0.04	0.63 ± 0.04	0.63 ± 0.04	0.64 ± 0.04	0.64 ± 0.04
4.2	0.00 ± 0.00	0.03 ± 0.01	0.53 ± 0.04	0.57 ± 0.04	0.57 ± 0.04	0.57 ± 0.04	0.57 ± 0.04
4.9	0.00 ± 0.00	0.00 ± 0.00	0.36 ± 0.04	0.51 ± 0.04	0.52 ± 0.04	0.53 ± 0.04	0.53 ± 0.04
5.6	0.00 ± 0.00	0.00 ± 0.00	0.23 ± 0.03	0.48 ± 0.04	0.52 ± 0.04	0.53 ± 0.04	0.54 ± 0.04
6.3	0.00 ± 0.00	0.00 ± 0.00	0.12 ± 0.02	0.41 ± 0.05	0.49 ± 0.05	0.51 ± 0.05	0.51 ± 0.05
7.0	0.00 ± 0.00	0.00 ± 0.00	0.05 ± 0.01	0.27 ± 0.05	0.38 ± 0.06	0.42 ± 0.06	0.43 ± 0.05

Color-coded from red (zero) to green (one).

From this profile, the rotor detection accuracy of current devices can be deduced. Considering that the average IED for current cardiac mapping catheters is around 4 mm (not taking into account distances between splines for basket catheters), the expected detection accuracy value is 57±4%. When it comes to the confidence interval, there is a 95% probability that the accuracy mean for a IED of 4.2 mm will not reach above 70%.

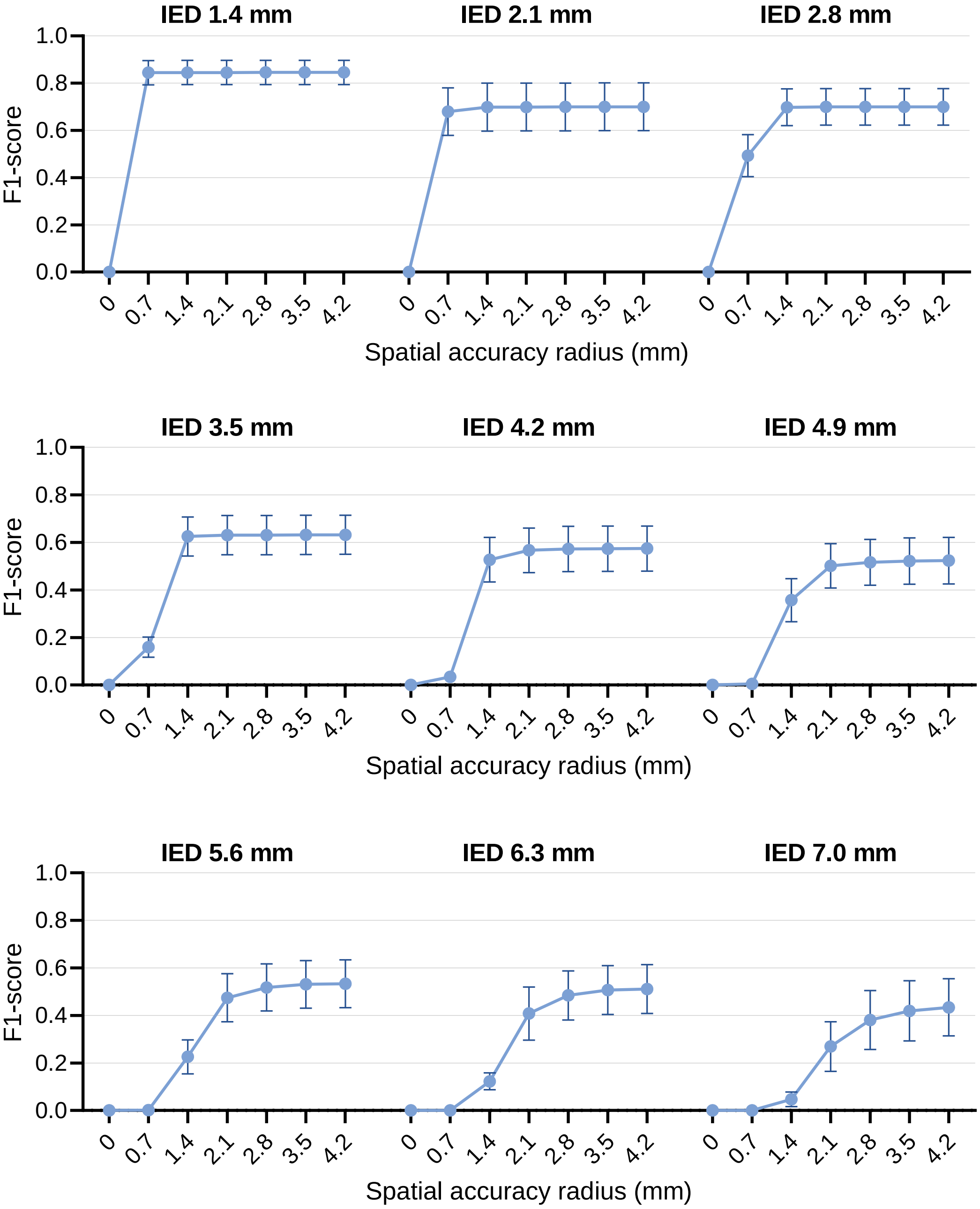

Figure 4.30: Detection accuracy (F1-score) profile with 95% confidence intervals of the mean for each sub-resolution, for all samples (N=11). IED, inter-electrode distance.

This profile obtained from all the experiments provides a useful generic guideline for IED requirements. However, it has been previously concluded that the detection accuracy varies depending on arrhythmia type (Section 4.4.1). Therefore, that distinction was performed in this section as well and a detection accuracy profile was computed for each arrhythmia type. However, when looking at the difference between detection accuracies obtained for MVT and VF, one has to bear in mind their difference in rotor incidence. That is, even though the F1-score is lower for MVT recordings at higher spatial resolutions, the number of rotors that are actually being missed or that are erroneous is inferior for MVT data than for VF data, as a general rule. Nevertheless, since MVT rotors tend to be more stable, the individual loss of these rotors will probably have more impact than the individual loss of a VF rotor.

The accuracy profile for MVT recordings is displayed in Table 4.12 and is complemented by Figure 4.31, that shows the confidence intervals of the means. In this table, the behaviour seen previously in Section 4.4.1 becomes more evident. Rotor detection accuracy for MVT initially drops as spatial resolution is lost. However, accuracy stabilizes in values around 50-65% for IED equal or higher than 2.1 mm. For a resolution of 4.2 mm, which is close to the clinical spatial resolution average, the rotor detection accuracy obtained is 58±4%, with a confidence interval close to 45-70% for a spatial accuracy of 3.5 mm. For this value to be above 80% or to increase reasonably, the spatial resolution has to be at least 1.4 mm.

For VF recordings, the accuracy profile is displayed in Table 4.13 and the corresponding confidence intervals are visually displayed in Figure 4.32. For current clinical resolution, mean detection accuracy is 56±8%. For VF, the minimum spatial resolution for an accuracy superior to 80% is 1.4 mm, as had been for MVT and for all recordings. For the current average clinical resolution (around 4 mm), rotor detection accuracy is 56±8%. For the worst-case scenario of a spatial resolution of 7 mm, which is a realistic resolution, rotor detection accuracy reaches 36±6%. It can be taken that these devices are not able to map VF.

If the goal of a study or treatment is solely to be able to detect stable arrhythmias, lower resolutions may suffice if detection accuracy around 50-60% is considered sufficient. Conversely, if there is a need to successfully detect highly unstable arrhythmias, resolution requirements become harsher.

Table 4.12: Color-coded rotor detection accuracy profile for multiple spatial resolutions and spatial accuracies, based on monomorphic ventricular tachycardia recordings (N=5). F1-score values are presented as mean±SEM.

Spatial resolution (mm)	**Spatial accuracy (mm)**						
	0	0.7	1.4	2.1	2.8	3.5	4.2
0.7	1.00 ± 0.00	1.00 ± 0.00	1.00 ± 0.00	1.00 ± 0.00	1.00 ± 0.00	1.00 ± 0.00	1.00 ± 0.00
1.4	0.00 ± 0.00	0.82 ± 0.03	0.82 ± 0.03	0.82 ± 0.03	0.83 ± 0.03	0.83 ± 0.03	0.83 ± 0.03
2.1	0.00 ± 0.00	0.62 ± 0.08	0.64 ± 0.08	0.64 ± 0.08	0.64 ± 0.08	0.64 ± 0.08	0.64 ± 0.08
2.8	0.00 ± 0.00	0.43 ± 0.06	0.66 ± 0.05	0.66 ± 0.05	0.66 ± 0.05	0.66 ± 0.05	0.66 ± 0.05
3.5	0.00 ± 0.00	0.18 ± 0.02	0.63 ± 0.04	0.64 ± 0.04	0.64 ± 0.04	0.64 ± 0.04	0.64 ± 0.04
4.2	0.00 ± 0.00	0.03 ± 0.01	0.55 ± 0.04	0.58 ± 0.04	0.58 ± 0.04	0.58 ± 0.04	0.58 ± 0.04
4.9	0.00 ± 0.00	0.00 ± 0.00	0.38 ± 0.07	0.49 ± 0.07	0.50 ± 0.07	0.50 ± 0.07	0.50 ± 0.07
5.6	0.00 ± 0.00	0.00 ± 0.00	0.27 ± 0.05	0.55 ± 0.06	0.59 ± 0.06	0.60 ± 0.06	0.60 ± 0.06
6.3	0.00 ± 0.00	0.00 ± 0.00	0.14 ± 0.02	0.52 ± 0.06	0.57 ± 0.06	0.57 ± 0.06	0.57 ± 0.06
7.0	0.00 ± 0.00	0.00 ± 0.00	0.06 ± 0.03	0.37 ± 0.08	0.47 ± 0.09	0.51 ± 0.09	0.52 ± 0.09

Color-coded from red (zero) to green (one).

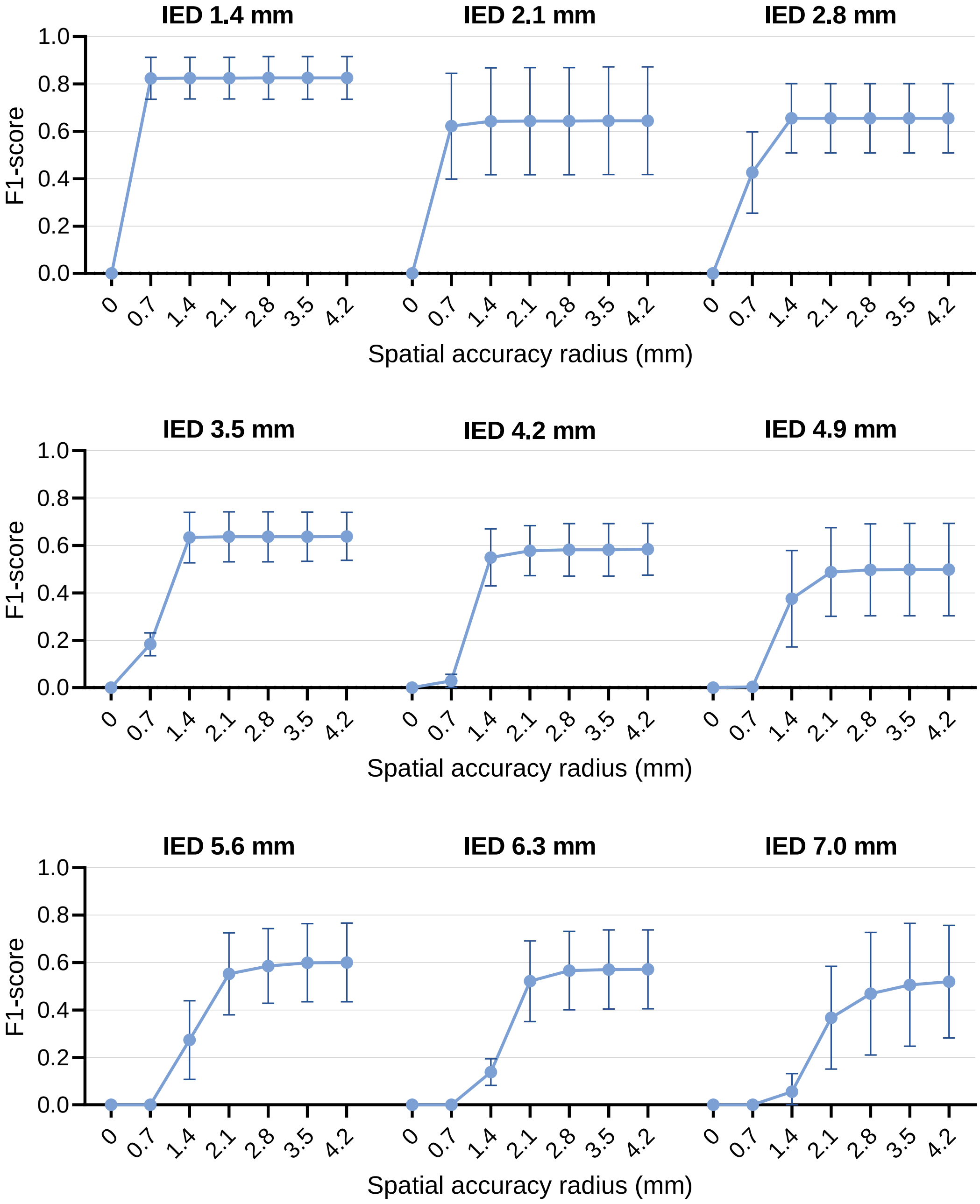

Figure 4.31: Detection accuracy (F1-score) profile with 95% confidence intervals of the mean for each sub-resolution, for monomorphic ventricular tachycardia (N=5). IED, inter-electrode distance.

Table 4.13: Color-coded rotor detection accuracy profile for multiple spatial resolutions and spatial accuracies, based on ventricular fibrillation recordings (N=6). F1-score values are presented as mean±SEM.

Spatial resolution (mm)	**Spatial accuracy (mm)**						
	0	0.7	1.4	2.1	2.8	3.5	4.2
0.7	1.00 ± 0.00	1.00 ± 0.00	1.00 ± 0.00	1.00 ± 0.00	1.00 ± 0.00	1.00 ± 0.00	1.00 ± 0.00
1.4	0.00 ± 0.00	0.86 ± 0.03	0.86 ± 0.03	0.86 ± 0.03	0.86 ± 0.03	0.86 ± 0.03	0.86 ± 0.03
2.1	0.00 ± 0.00	0.73 ± 0.04	0.75 ± 0.05	0.75 ± 0.05	0.75 ± 0.05	0.75 ± 0.05	0.75 ± 0.05
2.8	0.00 ± 0.00	0.55 ± 0.05	0.73 ± 0.05	0.74 ± 0.05	0.74 ± 0.05	0.74 ± 0.05	0.74 ± 0.05
3.5	0.00 ± 0.00	0.14 ± 0.03	0.62 ± 0.06	0.63 ± 0.06	0.63 ± 0.06	0.63 ± 0.06	0.63 ± 0.06
4.2	0.00 ± 0.00	0.04 ± 0.01	0.51 ± 0.07	0.56 ± 0.07	0.56 ± 0.08	0.56 ± 0.08	0.56 ± 0.08
4.9	0.00 ± 0.00	0.01 ± 0.00	0.35 ± 0.05	0.53 ± 0.06	0.55 ± 0.06	0.55 ± 0.06	0.56 ± 0.06
5.6	0.00 ± 0.00	0.00 ± 0.00	0.19 ± 0.03	0.41 ± 0.06	0.47 ± 0.06	0.48 ± 0.06	0.48 ± 0.06
6.3	0.00 ± 0.00	0.00 ± 0.00	0.11 ± 0.02	0.32 ± 0.05	0.42 ± 0.06	0.46 ± 0.06	0.47 ± 0.07
7.0	0.00 ± 0.00	0.00 ± 0.00	0.04 ± 0.01	0.19 ± 0.03	0.31 ± 0.06	0.35 ± 0.06	0.36 ± 0.06

Color-coded from red (zero) to green (one).

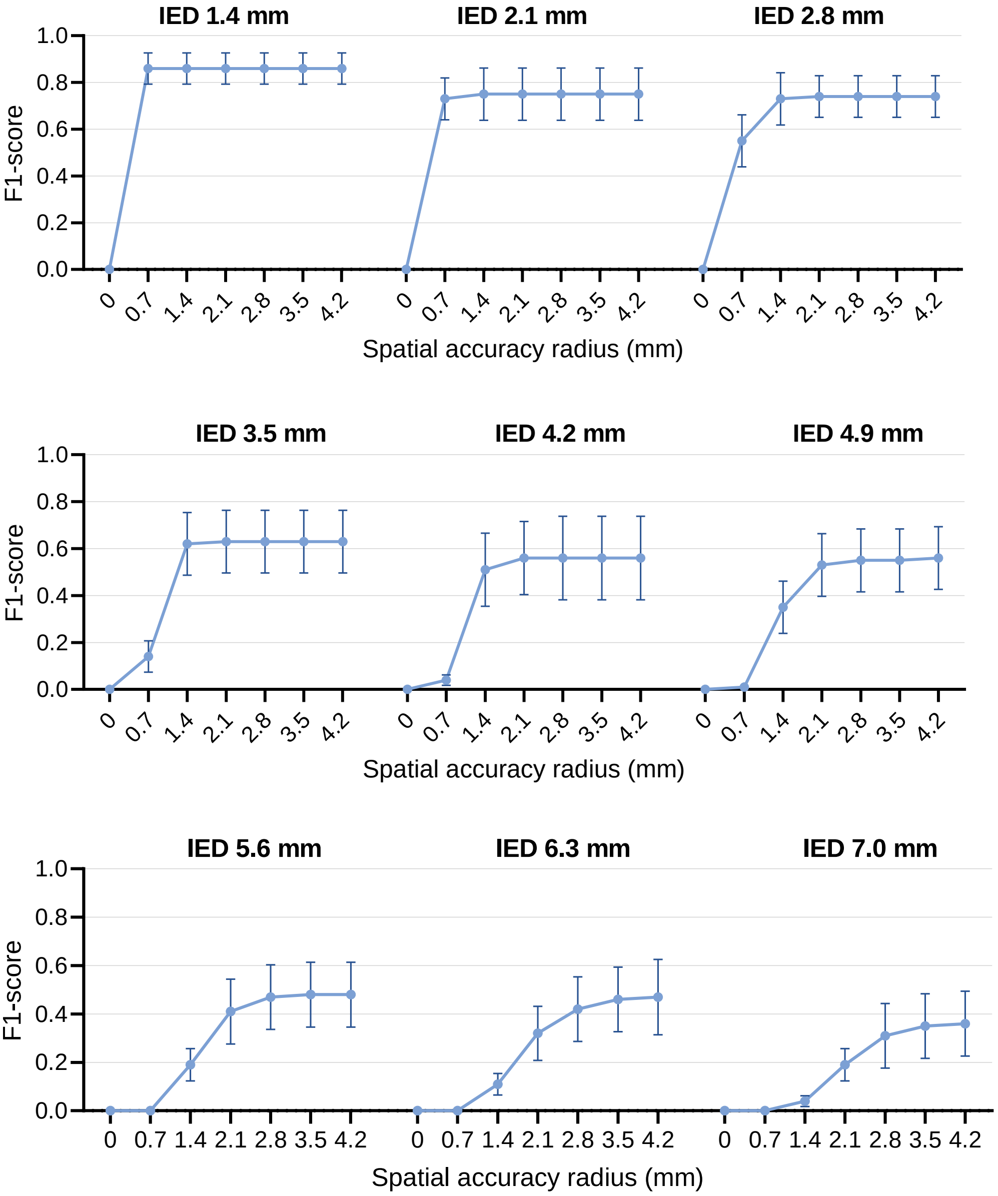

Figure 4.32: Detection accuracy (F1-score) profile with 95% confidence intervals of the mean for each sub-resolution, for VF samples (N=6). IED, inter-electrode distance.

4.5.2 Localization accuracy

Previously, localization accuracy was only assessed for a displacement (or spatial accuracy) radius of 3.5 mm. Here, the F1-scores for peak detection within a radius of 2.1 mm and 1.4 mm were also evaluated. The threshold of 3.5 mm was chosen initially since it corresponds to the radius of an average ablation lesion. However, for smaller device IEDs, the spatial accuracy will become more precise, so it was considered relevant to track the increase in permissible spatial accuracy as IED decreases. Since SRs are more relevant than APS and their relation for density peak detection has already been studied, only stable rotors were taken into consideration in this section. However, the accuracy profiles for APS density peak detection are available in Appendix B.

Table 4.14 displays stable rotor localization accuracy for varying resolution and spatial accuracy, for all recordings. For the spatial accuracy of an ablation lesion (radius of 3.5 mm), the expected accuracies are presented in the right column of the table. Considering a F1-score of 80% a good localization accuracy, this value can be reached for a spatial resolution of 2.1 mm. For the current clinical resolution, which is around 4.2 mm, the localization accuracy is only 61±7%. As therapies become more and more localized, spatial accuracy necessities grow. Evidently, the minimum spatial resolution needed grows as well.

Table 4.14: Color-coded rotor localization accuracy profile for multiple spatial resolutions and spatial accuracies, based on all recordings (N=11). F1-score values are presented as mean±SEM.

Spatial resolution (mm)	**Spatial accuracy (mm)**		
	1.4	2.1	3.5
0.7	1.00 ± 0.00	1.00 ± 0.00	1.00 ± 0.00
1.4	0.81 ± 0.05	0.87 ± 0.04	0.91 ± 0.03
2.1	0.67 ± 0.06	0.72 ± 0.05	0.80 ± 0.04
2.8	0.65 ± 0.06	0.75 ± 0.05	0.74 ± 0.06
3.5	0.59 ± 0.05	0.70 ± 0.05	0.71 ± 0.06
4.2	0.45 ± 0.08	0.55 ± 0.07	0.61 ± 0.07
4.9	0.34 ± 0.09	0.51 ± 0.07	0.57 ± 0.07
5.6	0.29 ± 0.06	0.50 ± 0.07	0.62 ± 0.07
6.3	0.21 ± 0.06	0.41 ± 0.07	0.52 ± 0.08
7.0	0.14 ± 0.05	0.25 ± 0.07	0.44 ± 0.08

Color-coded from red (zero) to green (one).

The complementary 95% confidence intervals of the means are displayed in Figure 4.33. Each curve represents the F1-score of density peaks detection as the spatial accuracy radius increases for a given spatial resolution. The size of the confidence intervals tends to grow as resolution decreases because the resulting F1-scores are more inconsistent. Nevertheless, even with wider ranges the CI limits keep decreasing with spatial resolution. For an IED of 2.8 mm the F1-score values are not incremental with

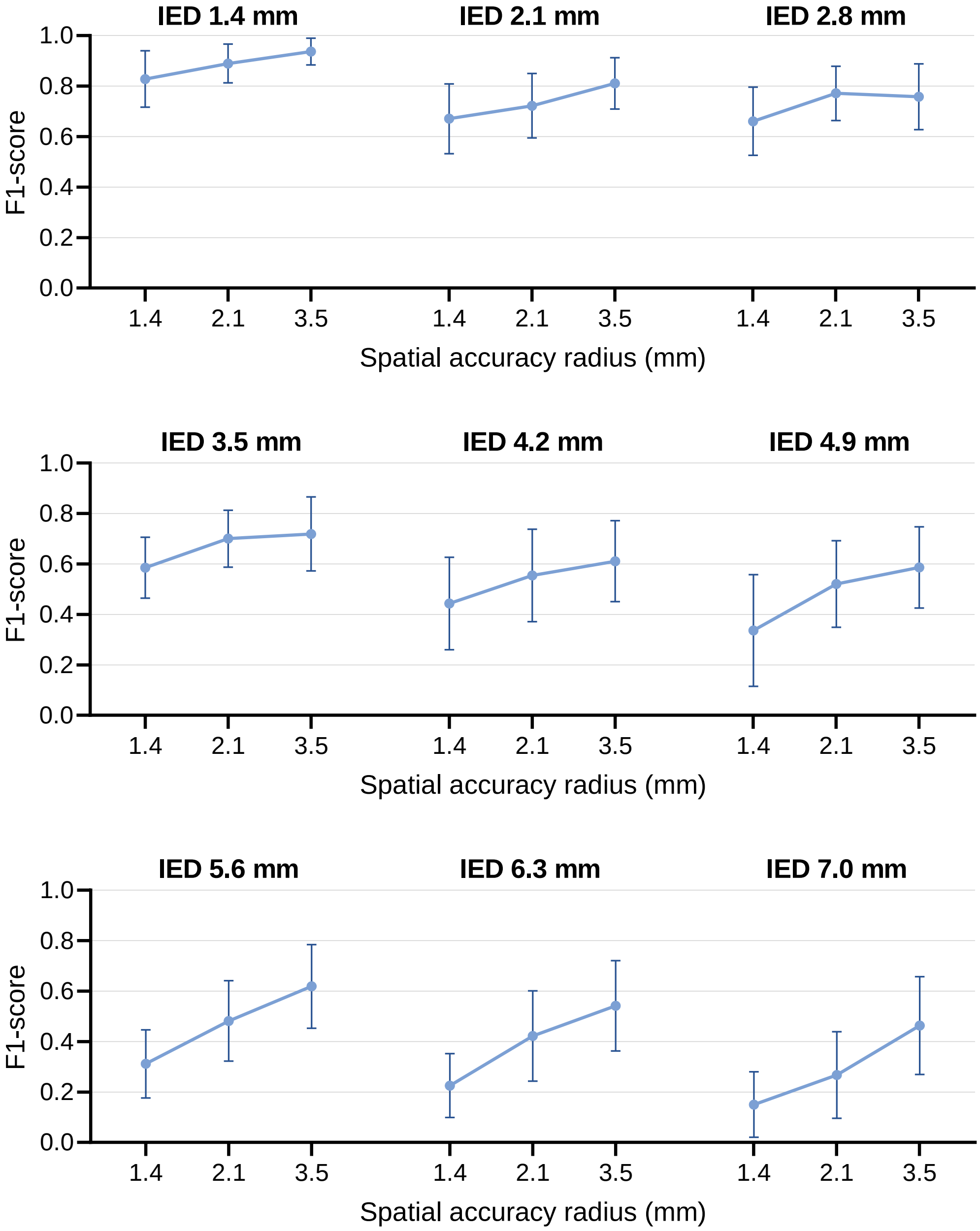

Figure 4.33: Localization accuracy (F1-score) profile with 95% confidence intervals of the mean for each sub-resolution, for all samples (N=11). IED, inter-electrode distance.

the spatial accuracy radius, with the intermediate value having the highest score. This occurs because of the peak detection conditions explained in Section 3.3.9. To avoid multiple detection of the same peak, a radius is defined within which only the highest density peak is considered a true peak. Consequently, the remaining peaks in the area are considered noise from the actual peak. This radius that was used to define a single peak corresponded to the spatial accuracy radius considered. Therefore, for smaller spatial accuracy radius the number of PS density peaks detected may be superior which leads to the possibility of the F1-score being higher for higher spatial accuracies. This was not observed for detection accuracies, in the previous section, because the number of true rotors was the same for every spatial accuracies, meaning the the F1-score could only decrease as the spatial accuracy radius decreased.

Arrhythmia type also influenced localization accuracy. Therefore, different localization accuracy profiles were created for MVT and VF as well.

Table 4.15 presents the localization accuracy profiles for MVT. Localization accuracy values are higher for MVT. For spatial accuracy of 3.5 mm, the average localization accuracy is never below 67%. It can be noted that for resolutions equal or lower than 2.8 mm mean accuracy varies within a small range between 65% and 80%. For the average current clinical resolution, localization accuracy is 70±4% with a confidence interval of 60% to 80%. Although still lacking, these results imply a relatively good localization accuracy for current devices. What this means is that, even if some MVT rotors are not being correctly detected or if false rotors appear, there is a relatively high probability that therapy will still be applied to the right area, since localization accuracy is higher than detection accuracy. Considering a more extreme example, the Constellation basket catheter [62] has an IED in each spline that can reach 7 mm depending on the model. For this spatial resolution, the expected accuracy is between 46-89%, with a mean value of 67±8%. These values are not too far from the values for average current IED.

Table 4.15: Color-coded rotor localization accuracy profile for multiple spatial resolutions and spatial accuracies, based on monomorphic ventricular tachycardia recordings (N=5). F1-score values are presented as mean±SEM.

Spatial resolution (mm)	**Spatial accuracy (mm)**		
	1.4	2.1	3.5
0.7	1.00 ± 0.00	1.00 ± 0.00	1.00 ± 0.00
1.4	0.91 ± 0.06	0.90 ± 0.06	0.98 ± 0.01
2.1	0.70 ± 0.10	0.77 ± 0.06	0.85 ± 0.06
2.8	0.62 ± 0.05	0.79 ± 0.05	0.79 ± 0.03
3.5	0.63 ± 0.04	0.76 ± 0.08	0.80 ± 0.09
4.2	0.49 ± 0.09	0.66 ± 0.07	0.70 ± 0.04
4.9	0.42 ± 0.14	0.62 ± 0.11	0.68 ± 0.11
5.6	0.30 ± 0.13	0.57 ± 0.11	0.79 ± 0.09
6.3	0.30 ± 0.10	0.50 ± 0.10	0.69 ± 0.06
7.0	0.24 ± 0.08	0.43 ± 0.11	0.67 ± 0.08

Color-coded from red (zero) to green (one).

However, the confidence intervals, presented in Figure 4.34, reveal that the localization accuracy for MVT is very inconsistent, specially for resolutions equal or lower than 4.9 mm. The wide CIs are due to the accuracy variability and due to the small number of samples. Nevertheless, for the highest accuracy radius, which corresponds to an average ablation lesion radius, localization accuracy is relatively high for all resolutions even when taking into account its confidence intervals. Therefore, for stable arrhythmias which are the easiest to map and localize, all currently used resolutions should have a decent probability of correctly localizing the rotors that are detected. However, for an localization accuracy higher than 90% the minimum resolution needs to be at least 1.4 mm.

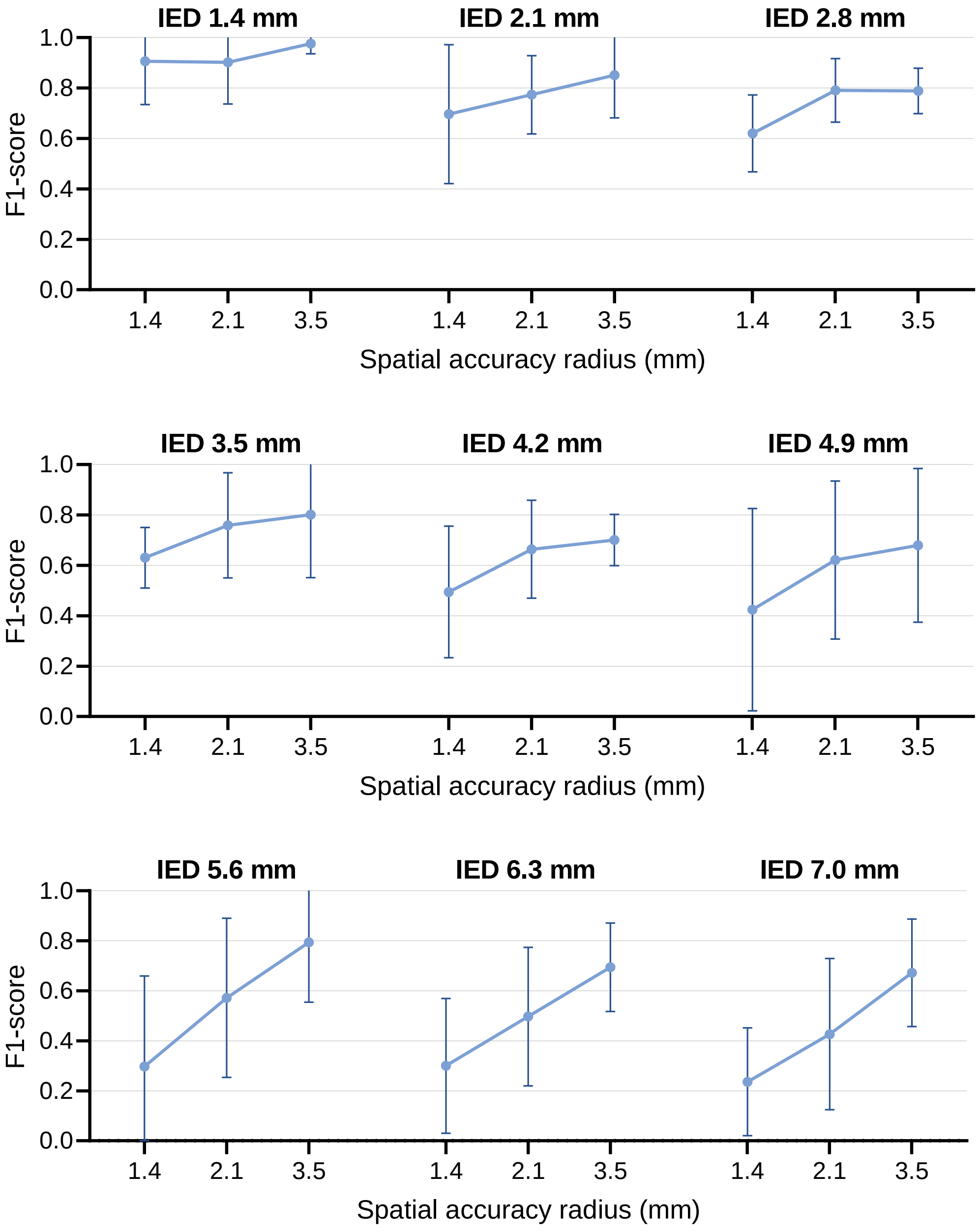

Figure 4.34: Localization accuracy (F1-score) profile with 95% confidence intervals of the mean for each sub-resolution, for monomorphic ventricular tachycardia (N=5). IED, inter-electrode distance.

For VF, the localization accuracy profile is presented in Table 4.16. It is harder to correctly localize unstable arrhythmias, as can be seen by the lower accuracy values. For a spatial accuracy of 3.5 mm, the spatial resolution has to be at least 4.9 mm for mean localization accuracy to be superior to 50%. To be higher than 70%, resolution has to be at least 2.8 mm, and to reach 90% it has to be at least 1.4 mm. For current clinical resolution, localization accuracy is 54±13%, that meaning that only close to half the rotors detected would be properly detected. Considering again the case of the Constellation basket catheter, for its resolution of 7 mm the localization accuracy is 29±8%, which leads to the conclusion that this device and others of comparable resolution are not apt to map unstable arrhythmias. As spatial accuracy needs increase, so does the resolution required. For a spatial accuracy of 2.1 mm, accuracies above 90% are hardly achievable for resolutions inferior to 0.7 mm, and for a spatial accuracy of 1.4 mm it is unlikely to have accuracies above 80% for spatial resolutions inferior to 0.7 mm.

Table 4.16: Color-coded rotor localization accuracy profile for multiple spatial resolutions and spatial accuracies, based on ventricular fibrillation recordings (N=6). F1-score values are presented as mean±SEM.

Spatial resolution (mm)	**Spatial accuracy (mm)**		
	1.4	2.1	3.5
0.7	1.00 ± 0.00	1.00 ± 0.00	1.00 ± 0.00
1.4	0.76 ± 0.07	0.88 ± 0.04	0.90 ± 0.04
2.1	0.65 ± 0.09	0.68 ± 0.10	0.78 ± 0.07
2.8	0.69 ± 0.10	0.76 ± 0.08	0.73 ± 0.11
3.5	0.55 ± 0.09	0.65 ± 0.07	0.65 ± 0.09
4.2	0.40 ± 0.13	0.46 ± 0.13	0.54 ± 0.13
4.9	0.26 ± 0.14	0.44 ± 0.10	0.51 ± 0.09
5.6	0.32 ± 0.05	0.41 ± 0.09	0.47 ± 0.08
6.3	0.16 ± 0.06	0.36 ± 0.12	0.41 ± 0.12
7.0	0.08 ± 0.08	0.14 ± 0.08	0.29 ± 0.08

Color-coded from red (zero) to green (one).

Figure 4.35 shows the complementary confidence intervals for VF. In the same manner as had happened for MVT, the CIs' ranges are considerably big for VF due to variability between means and to the low number of samples. However, the CIs' ranges tend to be bigger for VF samples than for MVT when considering higher resolutions, even with a slightly higher number of samples. This mean that the localization accuracy is even more volatile for VF, with its values being very disperse even for high resolutions.

The tables presented in this section provide an indication of the loss of information that can be expected for different spatial resolutions. The amount of loss highly depends on the stability of the arrhythmia mapped. The implications are that current available resolutions may be appropriate for ablating stable arrhythmias, but higher resolutions are needed for localized defibrillation to come to fruition. Furthermore, the spatial resolution of a mapping device is constrained by the feasibility of its manufacture and clinical applicability. Higher resolution mapping devices usually imply a smaller field of view, while lower resolution allows for more spacing between electrodes and consequently for

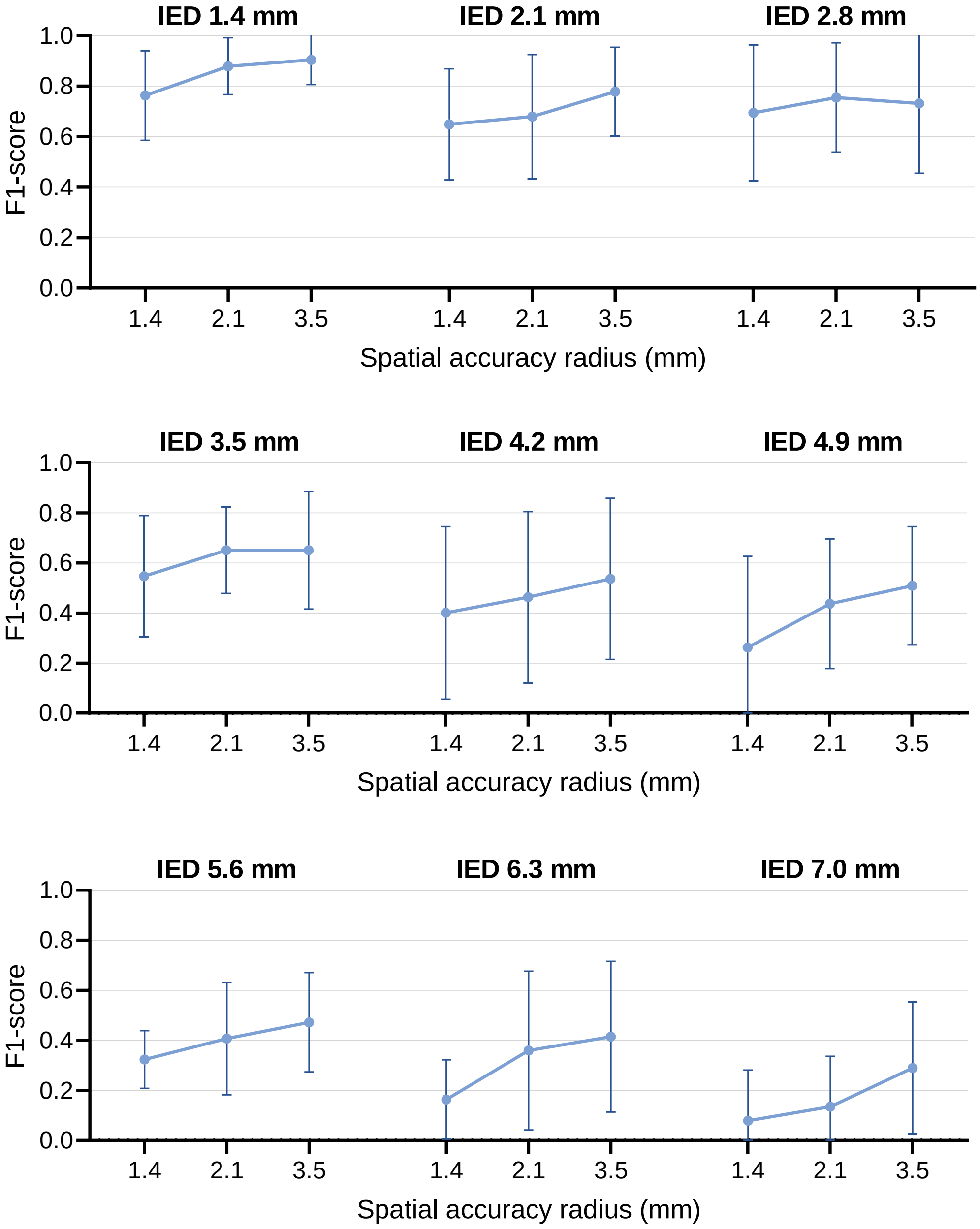

Figure 4.35: Localization accuracy (F1-score) profile with 95% confidence intervals of the mean for each sub-resolution, for ventricular fibrillation (N=6). IED, inter-electrode distance.

bigger mapped areas for the same number of electrodes. Therefore, a trade-off exists between resolution and mapped area that needs to be balanced according to the needs of the manufacturer. These accuracy profiles will enable a more knowledgeable decision with respect to the impact of spatial resolution on rotor detection and localization.

CHAPTER 5

CONCLUSIONS

This chapter concludes the thesis by presenting an overview of its findings, identifying its limitations, and recommending solutions and future directions.

5.1 Summary of findings

The aim of this thesis was to analyze the effects of inter-electrode distance in three aspects: perceived arrhythmia dynamics, rotor detection, and rotor localization.

The perceived arrhythmia dynamics entail the assumptions that may be made about arrhythmia mechanisms. Rotor incidence and duration reports have been inconsistent, leading to doubts regarding the prevalence and importance of these propagation discontinuities in arrhythmia mechanisms. A first analysis of the overall arrhythmia dynamics characteristics revealed that rotor incidence decreases as IED increases, while rotor duration did not change considerably. Stable rotors' incidence is more robust to spatial resolution loss. Regarding rotor detection accuracy, it decreases with increase in IED, as expected. Localization accuracy also decreases with increase in IED.

The data was further dissected by splitting the recordings according to mechanistic and biologic characteristics such as arrhythmia type, sex, anatomic region, and mapped surface.

Arrhythmia type impacted rotor incidence, duration, detection accuracy, and localization accuracy. Rotor incidence was higher for VF, while rotor duration was higher for MVT. These differences were expected, since more unstable arrhythmic episodes are characterized by disorganized excitation of the cardiac tissue, resulting in more rotors but of shorter duration. Furthermore, VF rotor incidence decreased at a faster rate than MVT rotor incidence for increasing IED. For the cases where VF incidence was clearly superior to MVT incidence, the incidence values become very close for lower resolutions.

Although differences were not significant for any IED, these results indicate a tendency for MVT and VF rotor incidence to become indistinguishable for lower resolutions. This may lead to misinterpretation of arrhythmia dynamics for high IEDs. Detection accuracy (F1-score) was not significantly different, but its variation due to spatial resolution was. Detection accuracy for VF decreased constantly with resolution, while for MVT it decreased initially and stabilized at around 50-65%. Localization accuracy also decreased constantly for VF, while it remained at higher values for MTV, not reaching below 60%.

Mapped surface impacted rotor incidence. Rotor incidence was higher in the endocardium than in the epicardium. Most likely, it is due to the presence of adipose tissue in the epicardium which interferes with the quality of the signals. Therefore, devices that map the endocardium will have a higher sensitivity to rotors for the same spatial resolution.

Sex and regional differences were not significant.

Regarding the spatial resolution requirements for robust rotor detection and localization, the questions are if the current resolution used in clinical settings is appropriate and what would the goal minimum spatial resolution be for the optimization of future mapping devices.

Current mapping devices detection accuracy can be deduced from the F1-scores obtained since the average of current clinical mapping resolution is known, which is around 4 mm. Approximate to that value, a resolution of 4.2 mm had a detection accuracy of 57±4% in this study. From the confidence intervals, rotor detection accuracy can be expected to be within 45% and 67% for that resolution. These are relatively low values, which explain the disappointing results for therapy targeting rotors. For an accuracy of at least 80%, spatial resolution would have to be a minimum of 1.4 mm. Nevertheless, any increase in spatial resolution will enhance rotor detection accuracy and represent an improvement.

Localization accuracy is 61±7% for the average clinical resolution. When comparing localization accuracies for MVT and VF, MVT is very robust to data loss, while VF's localization accuracy decreases rapidly. Therefore, novel focal therapies that target unstable arrhythmias will require much higher resolutions than treatments that focus on localizing stable arrhythmias.

Overall, the minimum spatial resolution depends on how accurate the manufacturer wants rotor detection and localization to be. Therefore, instead of reaching a specific value as the minimum resolution necessary for robust arrhythmia mapping, this work provides the rotor detection and localization accuracies that may be expected for multiple spatial resolutions.

5.2 Limitations and future work

A considerable limitation of this study was the absence of rotors in the area mapped by the electrode array. A clean correlation was found between electrical and optical data, but it would be relevant for the validation of this study to verify correlation between rotor detection for electrical data and optical data downsampled to a similar resolution.

Regarding the conditioning of the data and rotor tracking algorithm, there are several steps involved that bring a level of uncertainty that should be evaluated. In this study, the position of the downsampling grid was proved to contribute with a significant variation to the resulting F1-scores. A deeper analysis of the variability induced by data conditioning should be performed. Namely, simulated data could be run through the algorithm pipeline, in order to quantify methodology errors.

Experimental error also comes into play. Besides the inherent biological data variability, variation in experimental conditions could also impact the results. A source of possible error is the setting of the camera field of view as 7 cm, which was not an exact measurement.

Furthermore, the data is biased to the resolution of 0.7 mm set as the ground truth. As future work, it would be interesting to optically map a smaller field of view, resulting in an even higher spatial resolution as ground truth and compare with current results. However, the mapped area would decrease which would also influence the results.

Regarding the data analysis, the F1-score was used to evaluate the accuracy of both detection and localization of rotors. However, this metric does not take into account the number of false positives when no true positives are detected. This is limiting since the amount of false rotors/density peaks is still relevant when no true rotors/density peaks are detected. For the current study this occurrence was not significant, but it should be taken into account for future studies. For the statistical analysis, the normality of the data was assumed but it did not always coincide with the distribution of the data, which may interfere with the statistical inferences.

Lastly, the only pseudo-electrode configuration tested was a uniform grid. Future studies could gain from experimenting with other configurations to mimic specific mapping devices.

5.3 Study contributions

The relevance of this study falls upon, firstly, the contribution to the scientific knowledge regarding the effects of spatial resolution on perceived arrhythmia dynamics and, subsequently, on interpreted arrhythmia mechanisms. Secondly, the improvement of a software tool for the processing of optical data and tracking of rotors. The creation and peak detection of PS density maps and the conditioning and phase mapping of electrical data are also additions to the software that were developed in the duration of this work. Lastly, spatial resolution requirements guidelines are provided to assist future mapping devices fabrication, which may in turn improve therapy outcomes.

REFERENCES

[1] J. M. Lourenço, *The NOVAthesis LaTeX Template User's Manual*, NOVA University Lisbon, 2021. [Online]. Available: `https://github.com/joaomlourenco/novathesis/raw/master/template.pdf`.

[2] J. Rogers, "Combined phase singularity and wavefront analysis for optical maps of ventricular fibrillation", *IEEE Transactions on Biomedical Engineering*, vol. 51, no. 1, pp. 56–65, 2004. DOI: `10.1109/TBME.2003.820341`.

[3] "The top 10 causes of death" World Health Organization. https://www.who.int/newsroom/fact-sheets/detail/the-top-10-causes-of-death (accessed Aug. 28, 2021).

[4] R. J. Myerburg, A. Interian Jr, R. M. Mitrani, K. M. Kessler, and A. Castellanos, "Frequency of sudden cardiac death and profiles of risk", *The American journal of cardiology*, vol. 80, no. 5, 10F–19F, 1997.

[5] S. S. Chugh, K. Reinier, C. Teodorescu, *et al.*, "Epidemiology of sudden cardiac death: Clinical and research implications", *Progress in cardiovascular diseases*, vol. 51, no. 3, pp. 213–228, 2008.

[6] G. Lippi, F. Sanchis-Gomar, and G. Cervellin, "Global epidemiology of atrial fibrillation: An increasing epidemic and public health challenge", *International Journal of Stroke*, vol. 16, no. 2, pp. 217–221, 2021.

[7] K. C. Roberts-Thomson, P. M. Kistler, and J. M. Kalman, "Atrial tachycardia: Mechanisms, diagnosis, and management", *Current problems in cardiology*, vol. 30, no. 10, pp. 529–573, 2005.

[8] A. V. Dolinko, M. T. Kuntz, E. M. Antman, G. R. Strichartz, and L. S. Lilly, "Cardiovascular Drugs", in *Pathophysiology of Heart Disease: A Collaborative Project of Medical Students and Faculty: Fifth Edition*, Wolters Kluwer, 2016, ch. 17, pp. 400–455.

[9] R. A. DeSilva, T. B. Graboys, P. J. Podrid, and B. Lown, "Cardioversion and defibrillation", *American heart journal*, vol. 100, no. 6, pp. 881–895, 1980.

[10] A. Bhatia, R. Cooley, M. Berger, *et al.*, "The implantable cardioverter defibrillator: Technology, indications, and impact on cardiovascular survival", *Current Problems in Cardiology*, vol. 29, no. 6, pp. 303–356, 2004, ISSN: 01462806.

[11] M. M. Steffen, J. S. Osborn, and M. J. Cutler, “Cardiac implantable electronic device therapy: Permanent pacemakers, implantable cardioverter defibrillators, and cardiac resynchronization devices”, *Medical Clinics*, vol. 103, no. 5, pp. 931–943, 2019.

[12] M. Ahmad, L. Bloomstein, M. Roelke, A. D. Bernstein, and V. Parsonnet, “Patients’ attitudes toward implanted defibrillator shocks”, *Pacing and clinical electrophysiology*, vol. 23, no. 6, pp. 934–938, 2000.

[13] F. S. Ng, O. Toman, J. Petru, *et al.*, “Novel low-voltage MultiPulse Therapy to terminate atrial fibrillation”, *JACC: Clinical Electrophysiology*, 2021.

[14] V. C. Scanlon and T. Sanders, *Essentials of anatomy and physiology*. FA Davis, 2018.

[15] "Heart chambers: MedlinePlus Medical Encyclopedia Image" U.S. National Library of Medicine. `https://medlineplus.gov/ency/imagepages/19612.htm` (accessed Feb. 4, 2021).

[16] R. K. Turley, M. Snyder, and L. Cunningham, *Understanding coronary artery disease (CAD)*. [Online]. Available: `https://demo.staywellhealthlibrary.com/Content/healthsheets-v1/understanding-coronary-artery-disease-cad/`.

[17] J. E. Hall, *Textbook of Medical Physiology*. Philadelphia: Saunders Elsevier, 2011, ISBN: 978-1-4160-4574-8.

[18] K. L. McCance and S. E. Huether, *Pathophysiology: The Biologic Basis for Disease in Adults and Children: Eighth Edition*, ser. Pathophysiology the Biologic Basis. Elsevier, 2018, ISBN: 9780323583473.

[19] "Electrical Conduction System of the Heart" EKG.MD. `https://ekg.md/content/electrical-conduction-system/` (accessed Jan. 29, 2021).

[20] J. E. Lemieux, E. R. Edelman, G. R. Strichartz, and L. S. Lilly, “Normal cardiac structure and function”, in *Pathophysiology of Heart Disease: A Collaborative Project of Medical Students and Faculty: Fifth Edition*, Wolters Kluwer, 2016, ch. 1, pp. 1–25.

[21] M. J. Prust, W. G. Stevenson, and L. S. Lilly, “Clinical Aspects of Cardiac Arrhythmias”, in *Pathophysiology of Heart Disease: A Collaborative Project of Medical Students and Faculty: Fifth Edition*, Wolters Kluwer, 2016, ch. 12, pp. 286–309.

[22] M. J. Prust, W. G. Stevenson, G. R. Strichartz, and L. S. Lilly, “Mechanisms of Cardiac Arrhythmias”, in *Pathophysiology of Heart Disease: A Collaborative Project of Medical Students and Faculty: Fifth Edition*, Wolters Kluwer, 2016, ch. 11, pp. 268–285.

[23] M. J. Janse. "Reentry" ECAS European Cardiac Arrhythmia Society. `https://www.ecas-heartrhythm.org/reentry` (accessed Feb. 1, 2021).

[24] S. V. Pandit and J. Jalife, “Rotors and the dynamics of cardiac fibrillation”, *Circulation research*, vol. 112, no. 5, pp. 849–862, 2013.

[25] A. V. Panfilov and H. Dierckx, “Theory of Rotors and Arrhythmias”, in *Cardiac Electrophysiology: From Cell to Bedside*, Elsevier, 2018, ch. 34, pp. 325–334, ISBN: 978-0-323-44733-1.

[26] D. B. Geselowitz, “On the theory of the electrocardiogram”, *Proceedings of the IEEE*, vol. 77, no. 6, pp. 857–876, 1989.

[27] "Rhythm Recognition" ACLS Medical Training. `https://www.aclsmedicaltraining.com/rhythm-recognition/` (accessed Jul. 17, 2021).

[28] M. Helton, “Diagnosis and management of common types of supraventricular tachycardia”, *American family physician*, vol. 92, no. 9, pp. 793–800, 2015.

[29] D. G. Katritsis and A. J. Camm, “Classification and differential diagnosis of atrioventricular nodal re-entrant tachycardia”, *Europace*, vol. 8, no. 1, pp. 29–36, 2006.

[30] A. Goldberger, *Goldberger’s Clinical Electrocardiography*. Elsevier, 2018.

[31] B. Olshansky and R. M. Sullivan, “Inappropriate sinus tachycardia”, *Journal of the American College of Cardiology*, vol. 61, no. 8, pp. 793–801, 2013.

[32] A. J. Camm, “Hopes and disappointments with antiarrhythmic drugs”, *International Journal of Cardiology*, vol. 237, pp. 71–74, 2017, Sudden Cardiac Death, ISSN: 0167-5273. DOI: `https://doi.org/10.1016/j.ijcard.2017.03.056`. [Online]. Available: `https://www.sciencedirect.com/science/article/pii/S0167527317316649`.

[33] H. Calkins, G. Hindricks, R. Cappato, *et al.*, “2017 HRS/EHRA/ECAS/APHRS/-SOLAECE expert consensus statement on catheter and surgical ablation of atrial fibrillation”, *Ep Europace*, vol. 20, no. 1, e1–e160, 2018.

[34] M. Haissaguerre, P. Jaıs, D. C. Shah, *et al.*, “Spontaneous initiation of atrial fibrillation by ectopic beats originating in the pulmonary veins”, *New England Journal of Medicine*, vol. 339, no. 10, pp. 659–666, 1998.

[35] G. Lee, P. Sanders, and J. M. Kalman, “Catheter ablation of atrial arrhythmias: State of the art”, *The Lancet*, vol. 380, no. 9852, pp. 1509–1519, 2012.

[36] R. M. John, U. B. Tedrow, B. A. Koplan, *et al.*, “Ventricular arrhythmias and sudden cardiac death”, *The Lancet*, vol. 380, no. 9852, pp. 1520–1529, 2012.

[37] C. Carbucicchio, M. Santamaria, N. Trevisi, *et al.*, “Catheter ablation for the treatment of electrical storm in patients with implantable cardioverter-defibrillators: Short-and long-term outcomes in a prospective single-center study”, *Circulation*, vol. 117, no. 4, pp. 462–469, 2008.

[38] S. Knecht, F. Sacher, M. Wright, *et al.*, “Long-term follow-up of idiopathic ventricular fibrillation ablation: A multicenter study”, *Journal of the American College of Cardiology*, vol. 54, no. 6, pp. 522–528, 2009.

[39] A. Noheria and J. Anderson, “Advances in mapping and ablation of ventricular fibrillation”, *Current Treatment Options in Cardiovascular Medicine*, vol. 23, no. 3, pp. 1–24, 2021.

[40] S. M. Narayan, D. E. Krummen, M. W. Enyeart, and W.-J. Rappel, “Computational mapping identifies localized mechanisms for ablation of atrial fibrillation”, 2012.

[41] P. Benharash, E. Buch, P. Frank, *et al.*, “Quantitative analysis of localized sources identified by focal impulse and rotor modulation mapping in atrial fibrillation”, *Circulation: Arrhythmia and Electrophysiology*, vol. 8, no. 3, pp. 554–561, 2015.

[42] K. Umapathy, K. Nair, S. Masse, *et al.*, “Phase mapping of cardiac fibrillation”, *Circulation: Arrhythmia and Electrophysiology*, vol. 3, no. 1, pp. 105–114, 2010.

[43] S. M. Narayan, T. Baykaner, P. Clopton, *et al.*, “Ablation of rotor and focal sources reduces late recurrence of atrial fibrillation compared with trigger ablation alone: Extended follow-up of the CONFIRM trial (Conventional Ablation for Atrial Fibrillation With or Without Focal Impulse and Rotor Modulation)”, *Journal of the American College of Cardiology*, vol. 63, no. 17, pp. 1761–1768, 2014.

[44] E. Buch, M. Share, R. Tung, *et al.*, “Long-term clinical outcomes of focal impulse and rotor modulation for treatment of atrial fibrillation: A multicenter experience”, *Heart Rhythm*, vol. 13, no. 3, pp. 636–641, 2016.

[45] J. M. Miller, V. Kalra, M. K. Das, *et al.*, “Clinical benefit of ablating localized sources for human atrial fibrillation: The Indiana University FIRM Registry”, *Journal of the American College of Cardiology*, vol. 69, no. 10, pp. 1247–1256, 2017.

[46] S. Mohanty, P. Mohanty, C. Trivedi, *et al.*, “Long-term outcome of pulmonary vein isolation with and without focal impulse and rotor modulation mapping: Insights from a meta-analysis”, *Circulation: Arrhythmia and Electrophysiology*, vol. 11, no. 3, e005789, 2018.

[47] A. J. Shah, A. Jadidi, X. Liu, *et al.*, “Atrial tachycardias arising from ablation of atrial fibrillation: A proarrhythmic bump or an antiarrhythmic turn?”, *Cardiology research and practice*, vol. 2010, 2010.

[48] M. Han, L. Chen, K. Aras, *et al.*, “Catheter-integrated soft multilayer electronic arrays for multiplexed sensing and actuation during cardiac surgery”, *Nature Biomedical Engineering*, vol. 4, no. 10, pp. 997–1009, 2020.

[49] Y. Sandoval, M. N. Burke, A. S. Lobo, *et al.*, “Contemporary arterial access in the cardiac catheterization laboratory”, *JACC: Cardiovascular Interventions*, vol. 10, no. 22, pp. 2233–2241, 2017.

[50] P. A. Friedman, “Novel mapping techniques for cardiac electrophysiology”, *Heart*, vol. 87, no. 6, pp. 575–582, 2002.

[51] G. J. Klein, G. M. Guiraudon, A. D. Sharma, and S. Milstein, “Demonstration of macroreentry and feasibility of operative therapy in the common type of atrial flutter”, *The American journal of cardiology*, vol. 57, no. 8, pp. 587–591, 1986.

[52] G. K. Feld, R. Fleck, P.-S. Chen, *et al.*, “Radiofrequency catheter ablation for the treatment of human type 1 atrial flutter. identification of a critical zone in the reentrant circuit by endocardial mapping techniques.”, *Circulation*, vol. 86, no. 4, pp. 1233–1240, 1992.

[53] D. Durrer, R. T. Van Dam, G. Freud, M. Janse, F. Meijler, and R. Arzbaecher, “Total excitation of the isolated human heart”, *Circulation*, vol. 41, no. 6, pp. 899–912, 1970.

[54] A. S. Manolis and K. Lazaridis, “Focal atrial tachycardia ablation: Highly successful with conventional mapping”, *Journal of Interventional Cardiac Electrophysiology*, vol. 55, no. 1, pp. 35–46, 2019.

[55] I. Cakulev, M. W. Kroll, and M. V. Orlov, “The History of Mapping”, in *Cardiac Bioelectric Therapy*, I. R. Efimov, F. S. Ng, and J. I. Laughner, Eds., Springer Nature, 2021, ch. 3, pp. 27–40.

[56] B. Zrenner, G. Ndrepepa, M. Schneider, *et al.*, “Computer-assisted animation of atrial tachyarrhythmias recorded with a 64-electrode basket catheter”, *Journal of the American College of Cardiology*, vol. 34, no. 7, pp. 2051–2060, 1999.

[57] M. J. Schalij, F. P. van Rugge, M. Siezenga, and E. T. van der Velde, “Endocardial activation mapping of ventricular tachycardia in patients: First application of a 32-site bipolar mapping electrode catheter”, *Circulation*, vol. 98, no. 20, pp. 2168–2179, 1998.

[58] "Mapping catheter / intracardiac Constellation™ Boston Scientific" HealthManagement.org. `https://healthmanagement.org/products/view/mapping-catheter-intracardiac-constellation-boston-scientific` (accessed Jun. 13, 2021).

[59] Abbott, *The right tools for high-density mapping: High-density diagnostic mapping catheter portfolio.* Abbott, St. Paul, Massachusetts, 2018.

[60] "INTELLAMAP ORION™ Mapping Catheter" Boston Scientific. `https://www.bostonscientific.com/en-US/products/catheters--mapping/orion.html` (accessed Jun. 18, 2021).

[61] "PENTARAY® NAV ECO High Density Mapping Catheter" Johnson Johnson. `https://www.jnjmedicaldevices.com/en-US/product/pentaray-nav-eco-high-density-mapping-catheter` (accessed Jun. 18, 2021).

[62] Boston Scientific, *Constellation™ Full Contact Mapping Catheter.* Boston Scientific Corporation, San Jose, California, 2014.

[63] "IntellaMap Orion™ High-Resolution Mapping Catheter" Boston Scientific. `https://www.bostonscientific.com/en-US/medical-specialties/electrophysiology/cardiac-mapping-system/cardiac-arrhythmia-mapping-system/mapping-catheter.html` (accessed Jun. 19, 2021).

[64] Biosense Webster, *CATALOGUE 2021.* Johnson Johnson Medical NV/SA, Irvine, California, 2021.

[65] L. Martinez-Mateu, L. Romero, A. Ferrer-Albero, *et al.*, “Factors affecting basket catheter detection of real and phantom rotors in the atria: A computational study”, *PLoS computational biology*, vol. 14, no. 3, e1006017, 2018.

[66] J. Laughner, S. Shome, N. Child, *et al.*, “Practical considerations of mapping persistent atrial fibrillation with whole-chamber basket catheters”, *JACC: Clinical Electrophysiology*, vol. 2, no. 1, pp. 55–65, 2016.

[67] Y. J. Hong, H. Jeong, K. W. Cho, N. Lu, and D.-H. Kim, “Wearable and implantable devices for cardiovascular healthcare: From monitoring to therapy based on flexible and stretchable electronics”, *Advanced Functional Materials*, vol. 29, no. 19, p. 1 808 247, 2019.

[68] J. Viventi, D.-H. Kim, J. D. Moss, *et al.*, “A conformal, bio-interfaced class of silicon electronics for mapping cardiac electrophysiology”, *Science translational medicine*, vol. 2, no. 24, 24ra22–24ra22, 2010.

[69] L. Xu, S. R. Gutbrod, A. P. Bonifas, *et al.*, “3D multifunctional integumentary membranes for spatiotemporal cardiac measurements and stimulation across the entire epicardium”, *Nature communications*, vol. 5, no. 1, pp. 1–10, 2014.

[70] J. Liu, X. Zhang, Y. Liu, *et al.*, “Intrinsically stretchable electrode array enabled in vivo electrophysiological mapping of atrial fibrillation at cellular resolution”, *Proceedings of the National Academy of Sciences*, vol. 117, no. 26, pp. 14 769–14 778, 2020.

[71] J. Park, S. Choi, A. H. Janardhan, *et al.*, “Electromechanical cardioplasty using a wrapped elasto-conductive epicardial mesh”, *Science translational medicine*, vol. 8, no. 344, 344ra86–344ra86, 2016.

[72] S. Choi, S. I. Han, D. Jung, *et al.*, “Highly conductive, stretchable and biocompatible Ag–Au core–sheath nanowire composite for wearable and implantable bioelectronics”, *Nature nanotechnology*, vol. 13, no. 11, pp. 1048–1056, 2018.

[73] V. Kashyap, A. Caprio, T. Doshi, *et al.*, “Multilayer fabrication of durable catheter-deployable soft robotic sensor arrays for efficient left atrial mapping”, *Science advances*, vol. 6, no. 46, eabc6800, 2020.

[74] K. Song, J. H. Han, H. C. Yang, K. I. Nam, and J. Lee, “Generation of electrical power under human skin by subdermal solar cell arrays for implantable bioelectronic devices”, *Biosensors and Bioelectronics*, vol. 92, pp. 364–371, 2017.

[75] D.-H. Kim, R. Ghaffari, N. Lu, *et al.*, “Electronic sensor and actuator webs for large-area complex geometry cardiac mapping and therapy”, *Proceedings of the National Academy of Sciences*, vol. 109, no. 49, pp. 19 910–19 915, 2012.

[76] S. A. George, “History of Optical Mapping”, in *Cardiac Bioelectric Therapy*, I. R. Efimov, F. S. Ng, and J. I. Laughner, Eds., Springer Nature, 2021, ch. 4, pp. 41–48.

[77] J. I. Laughner, F. S. Ng, M. S. Sulkin, R. M. Arthur, and I. R. Efimov, “Processing and analysis of cardiac optical mapping data obtained with potentiometric dyes”, *American Journal of Physiology-Heart and Circulatory Physiology*, vol. 303, no. 7, H753–H765, 2012.

[78] C. O’Shea, S. N. Kabir, A. P. Holmes, *et al.*, “Cardiac optical mapping – State-of-the-art and future challenges”, *The international journal of biochemistry & cell biology*, vol. 126, p. 105 804, 2020.

[79] J. M. Guerra, E. Jorge, S. Raga, *et al.*, “Effects of open-irrigated radiofrequency ablation catheter design on lesion formation and complications: In vitro comparison of 6 different devices”, *Journal of cardiovascular electrophysiology*, vol. 24, no. 10, pp. 1157–1162, 2013.

[80] J. R. Winterfield, J. Jensen, T. Gilbert, *et al.*, “Lesion size and safety comparison between the novel flex tip on the FlexAbility ablation catheter and the solid tips on the ThermoCool and ThermoCool SF ablation catheters”, *Journal of cardiovascular electrophysiology*, vol. 27, no. 1, pp. 102–109, 2016.

[81] M. Alessandrini, M. Valinoti, L. Unger, *et al.*, “A computational framework to benchmark basket catheter guided ablation in atrial fibrillation”, *Frontiers in physiology*, vol. 9, p. 1251, 2018.

[82] K. N. Aronis and H. Ashikaga, “Impact of number of co-existing rotors and inter-electrode distance on accuracy of rotor localization”, *Journal of electrocardiology*, vol. 51, no. 1, pp. 82–91, 2018.

[83] C. H. Roney, C. D. Cantwell, J. D. Bayer, *et al.*, “Spatial resolution requirements for accurate identification of drivers of atrial fibrillation”, *Circulation: Arrhythmia and Electrophysiology*, vol. 10, no. 5, e004899, 2017.

[84] B. King, A. Porta-Sánchez, S. Massé, *et al.*, “Effect of spatial resolution and filtering on mapping cardiac fibrillation”, *Heart rhythm*, vol. 14, no. 4, pp. 608–615, 2017.

[85] R. D. Anderson, S. Kumar, J. M. Kalman, *et al.*, “Catheter ablation of ventricular fibrillation”, *Heart, Lung and Circulation*, vol. 28, no. 1, pp. 110–122, 2019.

[86] M. C. Mauney and I. L. Kron, “The physiologic basis of warm cardioplegia”, *The Annals of thoracic surgery*, vol. 60, no. 3, pp. 819–823, 1995.

[87] S. Joshi and D. J. Wilber, “Ablation of idiopathic right ventricular outflow tract tachycardia: Current perspectives”, *Journal of Cardiovascular Electrophysiology*, vol. 16, S52–S58, 2005.

[88] Q. Lou, W. Li, and I. R. Efimov, “The role of dynamic instability and wavelength in arrhythmia maintenance as revealed by panoramic imaging with blebbistatin vs. 2, 3-butanedione monoxime”, *American Journal of Physiology-Heart and Circulatory Physiology*, vol. 302, no. 1, H262–H269, 2012.

[89] M. Kovács, J. Tóth, C. Hetényi, A. Málnási-Csizmadia, and J. R. Sellers, “Mechanism of blebbistatin inhibition of myosin II”, *Journal of Biological Chemistry*, vol. 279, no. 34, pp. 35 557–35 563, 2004.

[90] M. Warren, K. W. Spitzer, B. W. Steadman, *et al.*, “High-precision recording of the action potential in isolated cardiomyocytes using the near-infrared fluorescent dye di-4-ANBDQBS”, *American Journal of Physiology-Heart and Circulatory Physiology*, vol. 299, no. 4, H1271–H1281, 2010.

[91] Z. Lu, B. Cui, B. He, *et al.*, “Distinct restitution properties in vagally mediated atrial fibrillation and six-hour rapid pacing-induced atrial fibrillation”, *Cardiovascular Research*, vol. 89, no. 4, pp. 834–842, Nov. 2010, ISSN: 0008-6363. DOI: `10.1093/cvr/cvq334`. eprint: `https://academic.oup.com/cardiovascres/article-pdf/89/4/834/724867/cvq334.pdf`. [Online]. Available: `https://doi.org/10.1093/cvr/cvq334`.

[92] K. Aras, *Cadence*, `https://github.com/kedararas/Cadence`, 2021.

[93] MATLAB, *version 9.10.0.1602886 (R2021a)*. Natick, Massachusetts: The MathWorks Inc., 2021.

[94] C. Gloschat, K. Aras, S. Gupta, *et al.*, “RHYTHM: an open source imaging toolkit for cardiac panoramic optical mapping”, *Scientific reports*, vol. 8, no. 1, pp. 1–12, 2018.

[95] R. Telgarsky, *Dominant Frequency Extraction*, 2013. arXiv: `1306.0103 [cs.NA]`.

[96] L. A. Unger, M. Rottmann, G. Seemann, and O. Dössel, “Detecting phase singularities and rotor center trajectories based on the hilbert transform of intraatrial electrograms in an atrial voxel model”, *Current Directions in Biomedical Engineering*, vol. 1, no. 1, pp. 38–41, 2015.

[97] M.-A. Bray and J. P. Wikswo, “Considerations in phase plane analysis for nonstationary reentrant cardiac behavior”, *Physical Review E*, vol. 65, no. 5, p. 051 902, 2002.

[98] C. H. Roney, “Mathematical techniques for assessing cardiac wavefront dynamics”, Ph.D. dissertation, Imperial College London, 2015.

[99] S. C. Chapra, *Applied numerical methods with MATLAB for engineers and scientists*. McGraw-Hill Higher Education, 2008.

[100] L. Leon and F. Roberge, "Directional characteristics of action potential propagation in cardiac muscle. A model study.", *Circulation research*, vol. 69, no. 2, pp. 378–395, 1991.

[101] K. K. Aras, N. R. Faye, B. Cathey, and I. R. Efimov, "Critical volume of human myocardium necessary to maintain ventricular fibrillation", *Circulation: Arrhythmia and Electrophysiology*, vol. 11, no. 11, e006692, 2018.

[102] J. D. Bayer, C. H. Roney, A. Pashaei, P. Jaıs, and E. J. Vigmond, "Novel radiofrequency ablation strategies for terminating atrial fibrillation in the left atrium: A simulation study", *Frontiers in physiology*, vol. 7, p. 108, 2016.

[103] P. Kuklik, S. Zeemering, B. Maesen, *et al.*, "Reconstruction of instantaneous phase of unipolar atrial contact electrogram using a concept of sinusoidal recomposition and hilbert transform", *IEEE transactions on biomedical engineering*, vol. 62, no. 1, pp. 296–302, 2014.

[104] R. Fabbri, L. D. F. Costa, J. C. Torelli, and O. M. Bruno, "2D euclidean distance transform algorithms: A comparative survey", *ACM Computing Surveys (CSUR)*, vol. 40, no. 1, pp. 1–44, 2008.

[105] H. Dalianis, "Evaluation Metrics and Evaluation", in *Clinical Text Mining: Secondary Use of Electronic Patient Records*. Cham: Springer International Publishing, 2018, pp. 45–53, ISBN: 978-3-319-78503-5. DOI: `10.1007/978-3-319-78503-5_6`. [Online]. Available: `https://doi.org/10.1007/978-3-319-78503-5_6`.

[106] X. Li, T. P. Almeida, N. Dastagir, *et al.*, "Standardizing single-frame phase singularity identification algorithms and parameters in phase mapping during human atrial fibrillation", *Frontiers in physiology*, vol. 11, p. 869, 2020.

[107] GraphPad Prism, *version 9.2.0 (332)*. GraphPad Software, LLC, 2021.

[108] A. M. Gillis, "Atrial fibrillation and ventricular arrhythmias: Sex differences in electrophysiology, epidemiology, clinical presentation, and clinical outcomes", *Circulation*, vol. 135, no. 6, pp. 593–608, 2017.

[109] R. R. Tilz, T. Lin, A. Rillig, *et al.*, "Focal impulse and rotor modulation for the treatment of atrial fibrillation: Locations and 1 year outcomes of human rotors identified using a 64-electrode basket catheter", *Journal of cardiovascular electrophysiology*, vol. 28, no. 4, pp. 367–374, 2017.

[110] W. Shimizu, "Arrhythmias originating from the right ventricular outflow tract: How to distinguish "malignant" from "benign"?", *Heart Rhythm*, vol. 6, no. 10, pp. 1507–1511, 2009.

[111] N. Calvo, M. Jongbloed, and K. Zeppenfeld, "Radiofrequency catheter ablation of idiopathic right ventricular outflow tract arrhythmias", *Indian Pacing and Electrophysiology Journal*, vol. 13, no. 1, pp. 14–33, 2013.

APPENDIX A

DONOR HEART CLINICAL INFORMATION

This appendix contains the available clinical information of the donor human hearts. The information is presented in Figure A.1.

Donor #	Age	Sex	Race	COD	LVEF	BMI	Drugs	Alcohol	Smoker	DM	HTN	Heart Disease
D1	62	M	Black	Brain Death	NA	23.3	Yes	Yes	Yes	No	No	No
D2	65	F	White	Stroke	NA	36.3	No	Yes	Yes	No	Yes	No
D3	71	F	White	Stroke	65%	26.6	No	Yes	No	No	No	No
D4	63	F	White	Stroke	NA	26.9	No	No	No	No	No	Sinus Tac
D5	49	M	Hispanic	Head T	70%	36.3	No	Yes	Yes	No	No	Mild LVH
D6	57	M	Black	Stroke	NA	40.2	No	Yes	No	No	Yes	No
D7	57	F	Black	Stroke	70%	29.2	No	Yes	Yes	No	No	No
D8	62	M	Hispanic	Stroke	NA	18.6	No	Yes	Yes	Yes	No	No
D9	68	F	Black	Brain Death	60%	30.4	No	No	No	No	Yes	Mild LVH
D10	60	F	White	Brain Death	NA	20.8	No	Yes	Yes	No	No	Sinus Tac
D11	56	M	White	Brain Death	55%	26.9	Yes	No	Yes	Yes	No	Sinus Tac
D12	51	M	White	Stroke	NA	21.5	Yes	Yes	Yes	No	No	MI

Figure A.1: Donor human heart information. Table of donor human heart information including age, sex, race, cause of death (COD), left ventricular ejection fraction (LVEF), body mass index (BMI), and relevant clinical history including drug, alcohol, nicotine (cigarette smoker) use, diabetes (DM), hypertension (HTM), and heart disease such as sinus tachycardia, left ventricular hypertrophy (LVH), and myocardial infarction (MI).

APPENDIX B

ADDITIONAL FIGURES AND TABLES

This appendix contains the supplementary figures and tables of the results section.

The majority of the sex differences results were not significant. Figures B.1 and B.2 present the comparison in rotor incidence for female and males donor hearts, for both all phase singularities (APS) and just stable rotors (SRs), respectively. The difference was not significant for either. Furthermore, Figures B.3 and B.4 show the distribution of mean rotor duration for both sexes, for APS and SRs respectively. Once more, the difference is not significant.

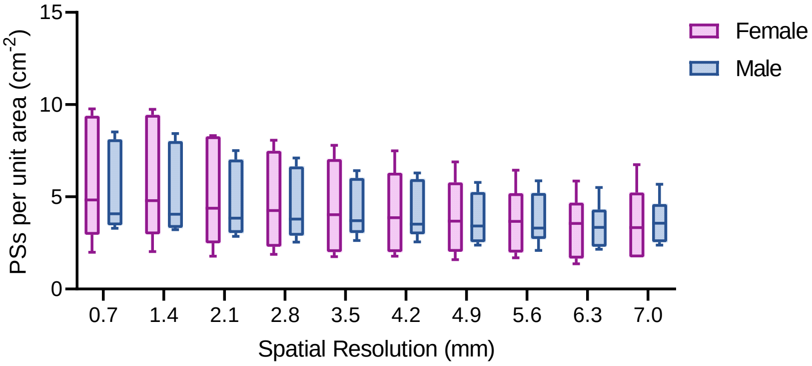

Figure B.1: Comparison of all phase singularities (APS) incidence for different sexes (N=12, female=6).

Figure B.2: Comparison of stable rotors (SRs) incidence for different sexes (N=11, female=5).

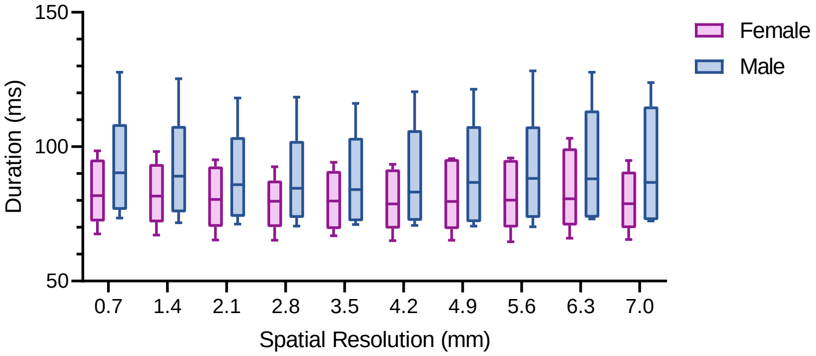

Figure B.3: Comparison of all phase singularities (APS) duration for different sexes (N=12, female=6).

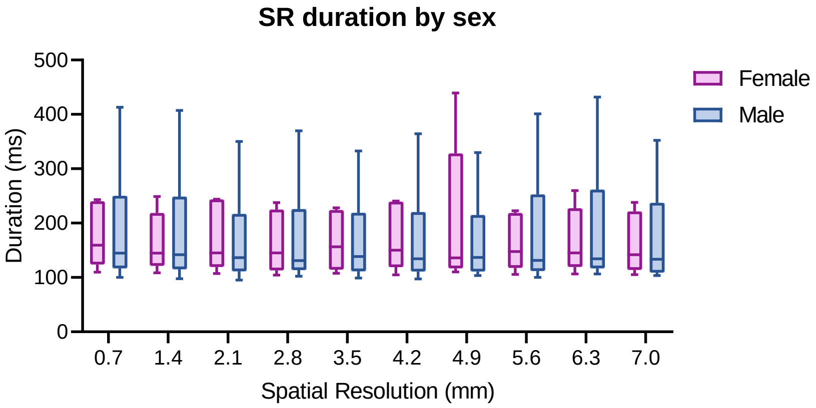

Figure B.4: Comparison of stable rotors (SRs) duration for different sexes (N=11, female=5).

The regional analysis did not provide statistically significant results. Figure B.5 shows the incidence for all phase singularities by anatomical region, while Figures B.6 and B.7 display the rotor duration by anatomical region for all phase singularities and stable rotors, respectively.

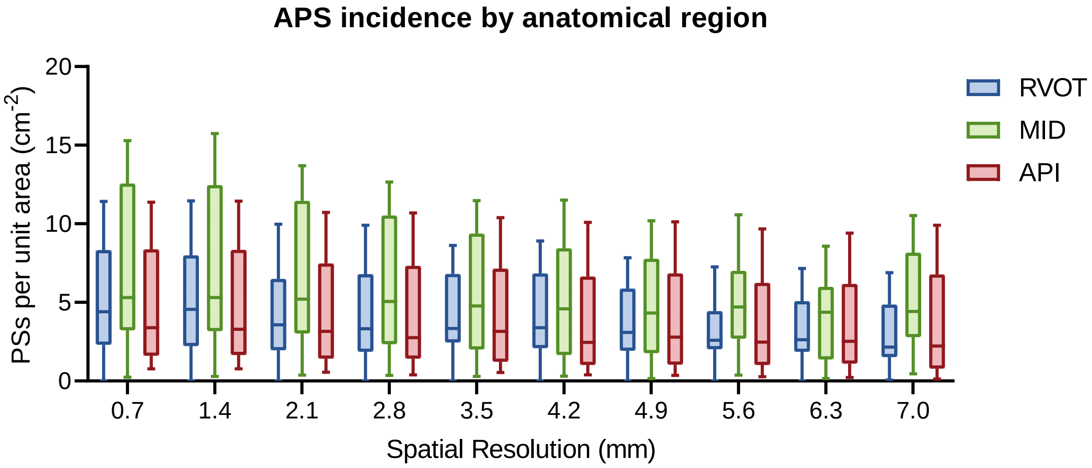

Figure B.5: Comparison of all phase singularities (APS) incidence for different anatomical regions (N=12). RVOT, right ventricular outflow tract; MID, mid-ventricular region; API, apical region.

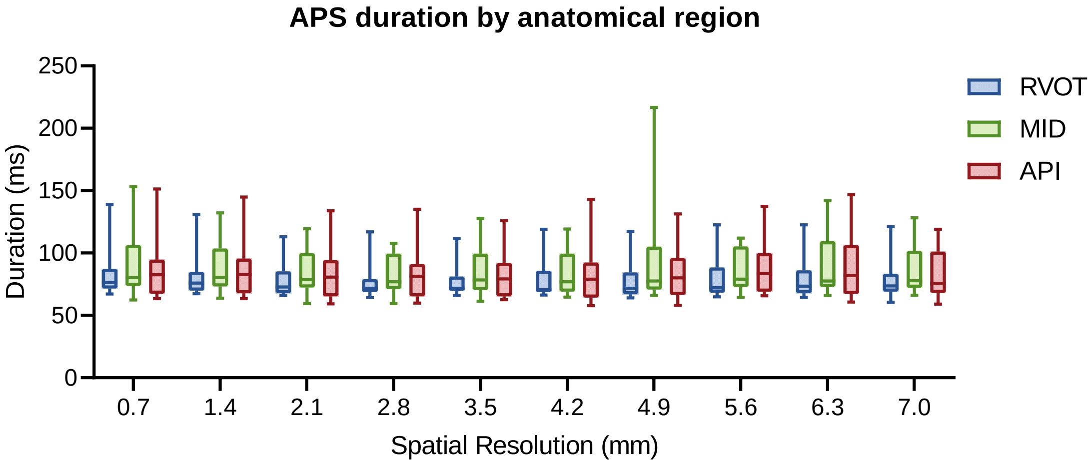

Figure B.6: Comparison of all phase singularities (APS) duration for different anatomical regions (N=12). RVOT, right ventricular outflow tract; MID, mid-ventricular region; API, apical region.

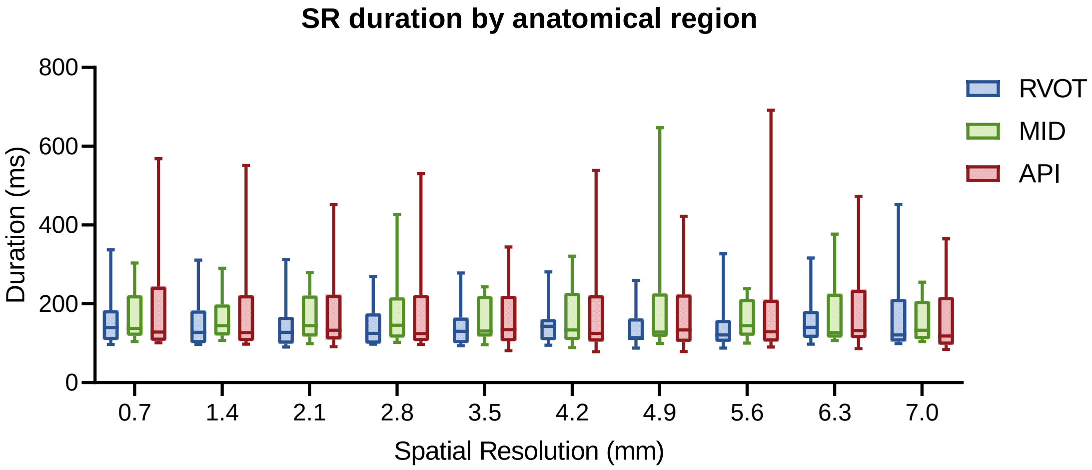

Figure B.7: Comparison of stable rotors (SRs) duration for different anatomical regions (N=11). RVOT, right ventricular outflow tract; MID, mid-ventricular region; API, apical region.

When comparing arrhythmia dynamics in the epicardium and the endocardium, the main difference observed was in rotor incidence. Conversely, no significant differences were observed for APS or SRs' duration, as shown in Figures B.8 and B.9, respectively. Furthermore, no differences were observed for rotor detection or rotor localization. The comparison of rotor localization accuracy in the epicardium and the endocardium is displayed in Figure B.10.

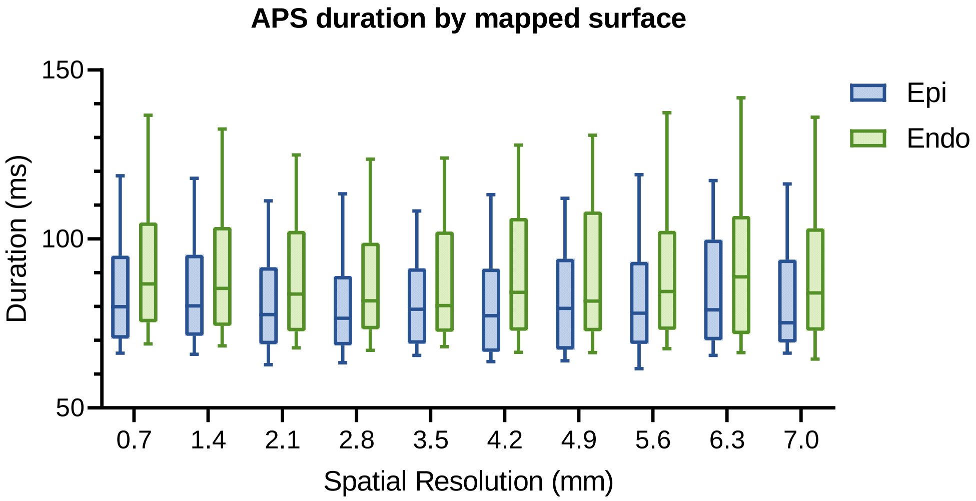

Figure B.8: Comparison of all phase singularities (APS) duration in the epicardium (Epi) and the endocardium (Endo) (N=12).

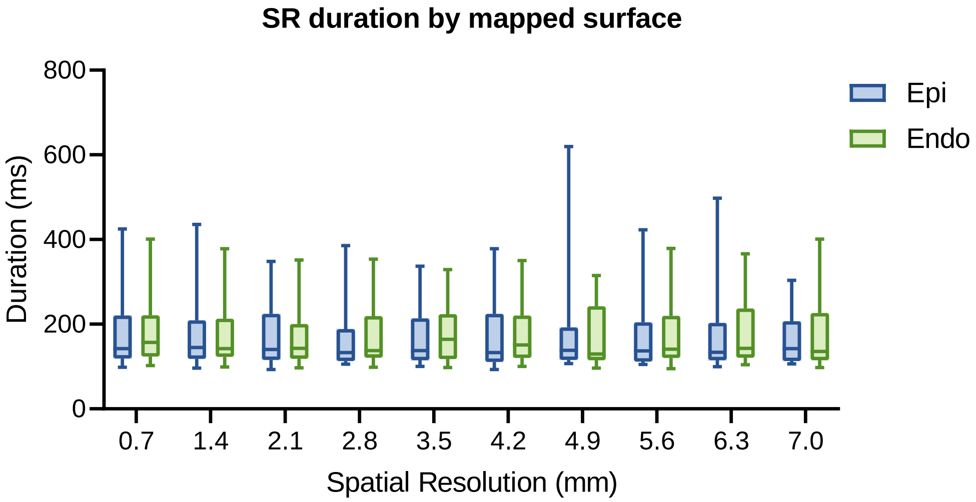

Figure B.9: Comparison of stable rotors (SRs) duration in the epicardium (Epi) and the endocardium (Endo) (N=11).

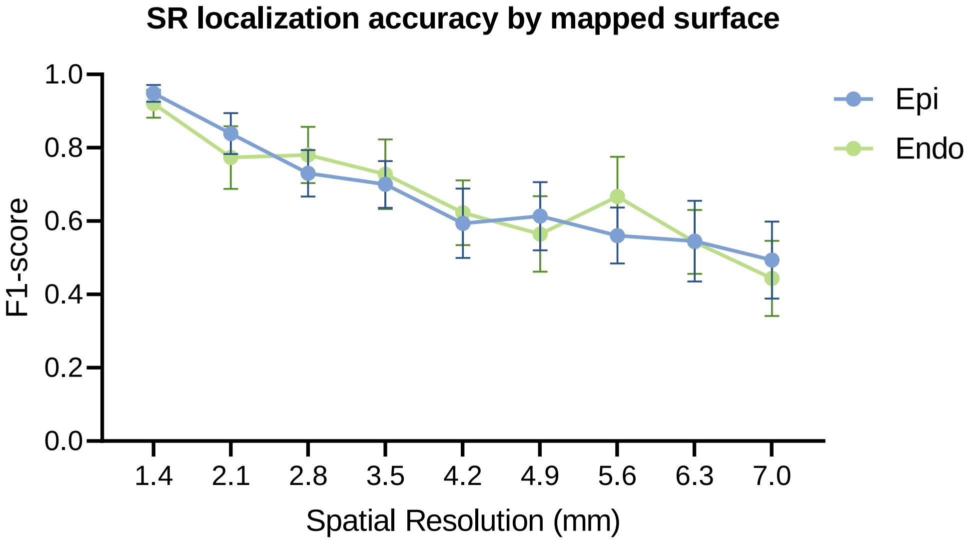

Figure B.10: Comparison of stable rotor (SR) localization accuracy for the epicardium (Epi) and the endocardium (Endo), given by the F1-score of rotor density peaks detection and for a spatial accuracy radius of 3.5 mm (N=11). F1-score is presented as mean±SEM.

Lastly, the following tables present the localization accuracy profiles for APS. Table B.1 corresponds to the accuracy profile for all recordings, Table B.2 refers to MVT recordings, and Table B.3 refers to VF recordings.

Table B.1: Color-coded localization accuracy profile for all phase singularities, based on all recordings (N=12). F1-score values are presented as mean±SEM.

Spatial resolution (mm)	**Spatial accuracy (mm)**		
	1.4	2.1	3.5
0.7	1.00 ± 0.00	1.00 ± 0.00	1.00 ± 0.00
1.4	0.89 ± 0.03	0.92 ± 0.02	0.93 ± 0.02
2.1	0.77 ± 0.04	0.83 ± 0.04	0.84 ± 0.04
2.8	0.68 ± 0.06	0.77 ± 0.05	0.81 ± 0.05
3.5	0.68 ± 0.06	0.74 ± 0.05	0.79 ± 0.04
4.2	0.48 ± 0.07	0.63 ± 0.06	0.73 ± 0.07
4.9	0.36 ± 0.07	0.55 ± 0.07	0.63 ± 0.07
5.6	0.30 ± 0.06	0.56 ± 0.08	0.64 ± 0.08
6.3	0.24 ± 0.05	0.37 ± 0.05	0.56 ± 0.07
7.0	0.12 ± 0.04	0.27 ± 0.08	0.46 ± 0.08

Color-coded from red (zero) to green (one).

Table B.2: Color-coded localization accuracy profile for all phase singularities, based on monomorphic ventricular tachycardia recordings (N=5). F1-score values are presented as mean±SEM.

Spatial resolution (mm)	**Spatial accuracy (mm)**		
	1.4	2.1	3.5
0.7	1.00 ± 0.00	1.00 ± 0.00	1.00 ± 0.00
1.4	0.89 ± 0.05	0.94 ± 0.02	0.93 ± 0.03
2.1	0.81 ± 0.07	0.84 ± 0.06	0.86 ± 0.06
2.8	0.61 ± 0.08	0.77 ± 0.07	0.81 ± 0.05
3.5	0.79 ± 0.05	0.79 ± 0.09	0.85 ± 0.05
4.2	0.52 ± 0.11	0.74 ± 0.04	0.87 ± 0.04
4.9	0.37 ± 0.13	0.59 ± 0.09	0.75 ± 0.09
5.6	0.30 ± 0.11	0.72 ± 0.07	0.83 ± 0.05
6.3	0.30 ± 0.08	0.36 ± 0.06	0.68 ± 0.07
7.0	0.19 ± 0.07	0.42 ± 0.13	0.64 ± 0.08

Color-coded from red (zero) to green (one).

Table B.3: Color-coded localization accuracy profile for all phase singularities, based on ventricular fibrillation recordings (N=7). F1-score values are presented as mean±SEM.

Spatial resolution (mm)	Spatial accuracy (mm)		
	1.4	2.1	3.5
0.7	1.00 ± 0.00	1.00 ± 0.00	1.00 ± 0.00
1.4	0.88 ± 0.04	0.91 ± 0.04	0.93 ± 0.04
2.1	0.75 ± 0.05	0.82 ± 0.06	0.83 ± 0.06
2.8	0.73 ± 0.09	0.78 ± 0.08	0.81 ± 0.07
3.5	0.61 ± 0.08	0.71 ± 0.06	0.75 ± 0.06
4.2	0.46 ± 0.10	0.55 ± 0.09	0.63 ± 0.10
4.9	0.35 ± 0.08	0.51 ± 0.10	0.55 ± 0.10
5.6	0.30 ± 0.07	0.44 ± 0.11	0.50 ± 0.10
6.3	0.20 ± 0.06	0.37 ± 0.08	0.48 ± 0.09
7.0	0.07 ± 0.04	0.16 ± 0.07	0.33 ± 0.10

Color-coded from red (zero) to green (one).